

# IPAM Research in Industrial Projects for Students (RIPS)

---



## A Method for Designing Impulsive Low-Energy Transfers Between the Earth and the Moon Using Invariant Manifolds\*

Summer 2006: June 26–August 26

Prepared for  
Jet Propulsion Laboratory

IPAM RIPS Team:

Stephen DeSalvo<sup>†</sup>  
Kenneth L. Ho

Jonathan Essen  
Gwenan Knight

Faculty Advisor:  
Stefano Campagnola

Liaison:  
Martin W. Lo

\*This project was jointly sponsored by NSF award no. DMS-0439872 and the Jet Propulsion Laboratory.

<sup>†</sup>Project manager



# *Abstract*

---

This report presents a systematic method for designing impulsive low-energy transfers between the Earth and the Moon by using invariant manifold theory. The Sun-Earth-Moon-spacecraft (-SC) four-body problem is chosen as a reference system and is well-approximated by two coupled planar circular restricted three-body problems (PCR3BPs): Sun-Earth-SC and Earth-Moon-SC. The invariant manifolds of each PCR3BP are studied independently, and the PCR3BPs are linked by manifold transfer. For simplicity, only the  $L_2$  manifolds are considered. A novel method of investigating these transfers by bounding the low-energy transfer regions is developed. The natural extension to the characterization of the transfer energy surfaces motivated by this method is discussed in detail. The initial trajectory obtained by patching the three-body solutions together is then corrected using four-body dynamics; the formulation of this correction scheme as an optimization problem is introduced. Furthermore, transfers between low Earth orbit or lunar orbit, and the manifolds in their respective PCR3BPs are investigated; and continuation methods for Lyapunov orbits and an adaptive perturbation magnitude scheme for manifold propagation are presented. All discussed methods are implemented as part of a documented MATLAB toolbox for low-energy Earth-Moon mission design.



# Table of contents

---

<b>Acknowledgements</b>	xi
<b>CHAPTER 1</b>	
<b>Introduction</b>	1
<b>CHAPTER 2</b>	
<b>Low-Energy Transfers Between the Earth and the Moon</b>	5
2.1 The $\Delta v$ Cost Function . . . . .	5
2.2 The Hohmann Transfer . . . . .	6
2.3 Invariant Manifolds in the Planar Circular Restricted Three-Body Problem .	9
2.4 Impulsive Low-Energy Earth-Moon Mission Design . . . . .	9
<b>CHAPTER 3</b>	
<b>The Planar Circular Restricted Three-Body Problem</b>	11
3.1 Introduction . . . . .	11
3.2 Equations of Motion . . . . .	11
3.3 The Jacobi Constant and Zero-Velocity Curves . . . . .	13
3.4 Lagrange Points, Lyapunov Orbits, and Invariant Manifolds . . . . .	13
<b>CHAPTER 4</b>	
<b>Continuation Methods for Lyapunov Orbits</b>	19
4.1 Breakdown of the Linearization Method . . . . .	19
4.2 Extrapolation of Initial Conditions for Lyapunov Orbits . . . . .	20
<b>CHAPTER 5</b>	
<b>Invariant Manifold Transfers</b>	25
5.1 Transfers Between Circular Orbits and Manifolds . . . . .	25
5.2 Transfers Between Sun-Earth and Earth-Moon Manifolds . . . . .	28
5.3 Poincaré Sections . . . . .	28
5.4 Low-Energy Transfer Regions . . . . .	29
5.5 Transfer Region Boundaries by Polygon Construction . . . . .	30
5.6 Types of Boundary Polygons . . . . .	30
5.7 Polygon construction . . . . .	31
5.8 Extension: Density Control by Grid Selection . . . . .	32

**CHAPTER 6**

<b>Extension: Characterization of the <math>\Delta v</math> Surface</b>	35
6.1 Introduction . . . . .	35
6.2 Manifold Layers . . . . .	35
6.3 Parametric Study of the Transfer Region . . . . .	40
6.4 Potential for Future Research . . . . .	40

**CHAPTER 7**

<b>Trajectory Correction Using Four-Body Dynamics</b>	41
7.1 The Bicircular Model . . . . .	41
7.2 Coupling the Three-Body Trajectories . . . . .	42
7.3 Multiple Shooting as an Optimization Problem . . . . .	43

**CHAPTER 8**

<b>Conclusion</b>	49
-------------------	----

**APPENDIX A**

<b>Restricted Two-Body Problem Dynamics</b>	51
A.1 Equations of Motion . . . . .	51
A.2 Planar Motion . . . . .	51
A.3 Energy . . . . .	52
A.4 Properties of an Ellipse . . . . .	53

**APPENDIX B**

<b>Table of Parameter Values</b>	55
----------------------------------	----

**APPENDIX C**

<b>Derivation of the Equations of Motion for the PCR3BP</b>	57
C.1 Inertial (Sidereal) Coordinates . . . . .	57
C.2 Rotating (Synodic) Coordinates . . . . .	58
C.3 The Jacobi Constant . . . . .	59

**APPENDIX D**

<b>Invariant Manifold Computation</b>	61
D.1 Lagrange Points . . . . .	61
D.2 Linearization About the Collinear Lagrange Points . . . . .	63
D.3 Periodic Orbits in the Linearized System . . . . .	64
D.4 Lyapunov Orbits by Differential Correction . . . . .	65
D.5 Stability Directions: The Monodromy Matrix . . . . .	69
D.6 Integration of Perturbations Along the Stability Directions . . . . .	73
D.7 Manifold Propagation: Parameter Considerations and Adaptive Methods . .	73

**APPENDIX E**

<b>Coordinate Transformations</b>	83
E.1 Geometry of the Coupled Systems . . . . .	83
E.2 Coordinate Transformations . . . . .	83
E.3 Non-Dimensional Coordinates . . . . .	85

**APPENDIX F**

<b>The MATLAB Toolbox</b>	87
F.1 Manifold Computation . . . . .	87
F.2 Manifold Transfer . . . . .	89
F.3 Trajectory Correction . . . . .	92
F.4 Database . . . . .	92
F.5 Integration . . . . .	93
<b>Bibliography</b>	95





## List of figures

---

1.1	Artist's conception of the Interplanetary Superhighway . . . . .	2
2.1	Propellant mass fraction as a function of $\Delta v$ . . . . .	6
3.1	Schematic diagram of the PCR3BP . . . . .	12
3.2	Zero-velocity curves of the PCR3BP . . . . .	14
3.3	Lagrange points of the PCR3BP. . . . .	15
3.4	Invariant manifolds projecting from $LL_2$ . . . . .	17
4.1	Lack of suitable Earth orbit transfers for small $EL_2$ manifolds . . . . .	20
4.2	Data generated by the continuation method . . . . .	22
5.1	Intersection of unstable $LL_2$ manifold with LO . . . . .	27
5.2	Schematic diagram of a Poincaré section . . . . .	29
5.3	Low-energy transfer regions between $EL_2$ and $LL_2$ manifolds . . . . .	33
6.1	Intersection of unstable $EL_2$ manifold with stable $LL_2$ manifold . . . . .	36
6.2	Contour plot of $\Delta v$ for transfer between $EL_2$ and $LL_2$ manifolds . . . . .	37
6.3	Contour plot of $\Delta v$ superimposed on manifolds . . . . .	38
6.4	Zoomed-in contour plot of $\Delta v$ superimposed on manifolds . . . . .	39
7.1	Schematic diagram of the bicircular model . . . . .	42
7.2	Transfer of minimum $\Delta v$ connecting LEO with $EL_2$ manifold . . . . .	43
7.3	Transfer of minimum $\Delta v$ connecting LO with $LL_2$ manifold . . . . .	44
7.4	Transfer of minimum $\Delta v$ connecting $EL_2$ and $LL_2$ manifold . . . . .	45
7.5	Coupled PCR3BP trajectory from LEO to LO . . . . .	46
7.6	Coupled PCR3BP trajectory with corresponding bicircular trajectory . . . .	47
C.1	Schematic diagram of the PCR3BP in the inertial frame. . . . .	58
C.2	Schematic diagram of the PCR3BP in the rotating frame. . . . .	59
D.1	Lagrange points of the PCR3BP. . . . .	62
D.2	Comparison of periodic orbits in the linear and nonlinear systems . . . . .	66
D.3	Lyapunov orbit corrections with $\delta x_0 = 0$ . . . . .	69
D.4	Lyapunov orbit corrections with $\delta \dot{y}_0 = 0$ . . . . .	70
D.5	Corrected Lyapunov orbits versus linear approximations . . . . .	71

D.6	The relationship between $\Phi$ and $\Psi$ . . . . .	72
D.7	Stable and unstable $LL_2$ invariant manifolds . . . . .	74
D.8	Small manifolds satisfying the evaluation criteria . . . . .	77
D.9	Medium manifolds satisfying the evaluation criteria . . . . .	78
D.10	Large manifolds satisfying the evaluation criteria . . . . .	79
D.11	Invariant manifolds violating the first-pass restriction . . . . .	80

## *List of tables*

---

B.1	Table of parameter values for the Sun-Earth system. . . . .	55
B.2	Table of parameter values for the Earth-Moon system. . . . .	56
D.1	Jacobi constant bounds in the manifold database. . . . .	78
D.2	Jacobi constant bounds for intersection with LEO and LO. . . . .	78



## *Acknowledgements*

---

First and foremost, we would like to thank Dr. Martin Lo of the Jet Propulsion Laboratory (JPL), and the Institute for Pure and Applied Mathematics (IPAM) for sponsoring this project and for providing us with such an interesting and informative summer. Thanks also to Martin for all of the time that he has spent with us over the course of the program. Throughout this project, faculty advisor Stefano Campagnola was an invaluable source of support and information. We would like to thank him for providing us with such in-depth background knowledge and for giving us an insight into the realities of project-based research.

We would also like to thank Prof. Mike Raugh for all of his help with presentations and reports. Finally, we would like to thank all of the staff at IPAM for their help this summer and for organizing this extraordinary program, in particular, Prof. Mark Green, Stacey Beggs, and Liza Manukyan. Special thanks also go to IPAM's technical staff Edward Soong, Michael Wu, and Jim Kimmick for all of their help in resolving technical support issues.



# CHAPTER 1

## *Introduction*

---

This report documents research work performed during the summer of 2006 as part of the Research in Industrial Projects for Students (RIPS) program at the Institute for Pure and Applied Mathematics (IPAM). The project was proposed by the Jet Propulsion Laboratory (JPL) to study the classes of impulsive low-energy transfers between the Earth and the Moon. The California Institute of Technology established JPL in the 1930's as a rocket propulsion experimental laboratory. The United States' first successful satellite, Explorer 1, was created at JPL. Currently, JPL builds and operates unmanned spacecraft for the National Aeronautics and Space Administration (NASA) to support the exploration of the solar system.

Over the years, JPL has led several outstanding missions to explore the solar system. Of particular interest is the Genesis Discovery Mission, designed by JPL to collect samples of the solar wind for the purpose of furthering the understanding of planetary formation. Launched on August 8, 2001, Genesis was unique in that its return trajectory required no deterministic maneuvers. This is a consequence of using the Interplanetary Superhighway (Figure 1.1), a system of low-energy transport conduits throughout the solar system predicted by nonlinear dynamical systems theory and discovered by Dr. Martin Lo of JPL. These conduits, known as invariant manifolds, support low-energy transfers between the celestial bodies in the solar system.

An invariant manifold can be thought of as a gravitational passageway that connects different regions of space through natural dynamics. A body on a manifold will remain on the manifold purely as a consequence of gravitational forces. Thus, for trajectories following a manifold, no thrusts are required to keep on course. Furthermore, these invariant manifolds govern the behaviors of nearby trajectories, hence it is possible to design mission trajectories by considering the qualitative dynamics imposed by the invariant manifold structure of the system.

The concepts underlying the dynamics of the Interplanetary Superhighway have already been used successfully in mission design: ICEE-3/ICE (1978), WIND (1994), SOHO (1995), ACE (1997), MAP (2001), Genesis (2001) [3]. With the exception of the Genesis mission, however, these have all occurred without the conscious recognition of the use of invariant manifold theory. Thus, the trajectories of these missions have been retroactively explained by the dynamics of the invariant manifold structure of the solar system. Similarly, the trajectories of natural phenomena, such as the strange orbit of the comet Oterma around Jupiter, have also been explained by these dynamics [12]. More designs exploiting invariant manifolds are currently in place for future missions: TRIANA (2008), NGST/JWST (2011), Constellation X (2013), BepiColombo (2014) [3, 11].

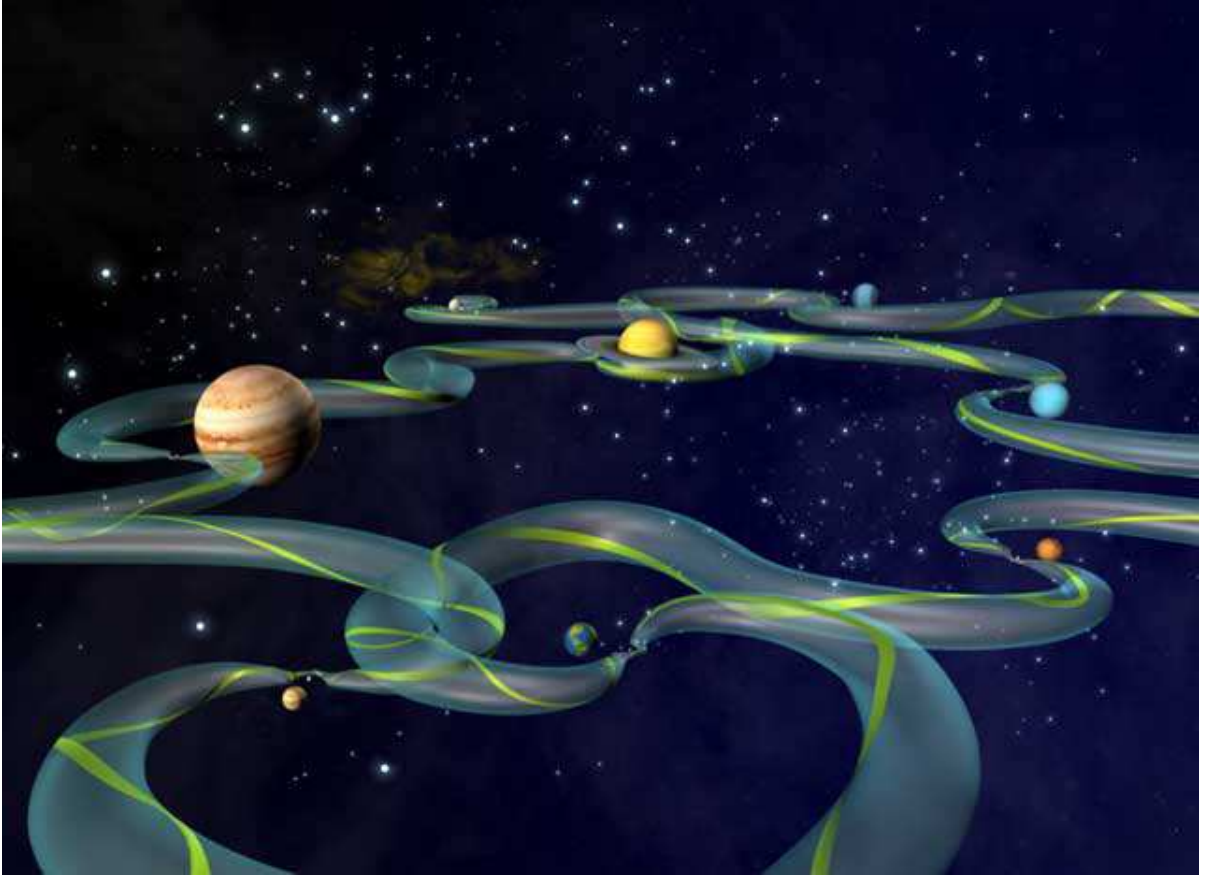


FIGURE 1.1. Artist's conception of the Interplanetary Superhighway. Image courtesy of JPL: <http://www.jpl.nasa.gov/>.

This project aims to develop a systematic method for the design of low-energy transfers between the Earth and the Moon by the explicit use of invariant manifold theory. The four-body Sun-Earth-Moon-spacecraft (-SC) system is chosen as a suitable reference system, but our approach considers its approximation as two coupled three-body systems: Sun-Earth-SC and Earth-Moon-SC. The three-body model considered is the planar circular restricted three-body problem (PCR3BP), which is a standard model used in astrodynamics research that captures the nonlinear dynamics present in our problem. The invariant manifolds considered are the invariant manifolds of each PCR3BP. The main contribution of this project is a study of the nature of low-energy transfers available between the invariant manifolds of the Sun-Earth and Earth-Moon systems. Full trajectories are obtained by patching together the solutions in each PCR3BP and then correcting using four-body dynamics.

Although Earth-Moon mission trajectories designed using this method are expected to have significantly longer in-flight times due to the roundabout nature of the flight



path, the amount of fuel saved and, thus, the reduction in mission cost allow otherwise impossible missions to be undertaken. In the context of NASA's adherence to the separation of manned and unmanned spaceflight, and its new resolve in returning to the Moon, this therefore has applications in the transport of heavy cargo to and from the Moon.

As a result of the project, the following will be delivered to JPL: a MATLAB (*The MathWorks*, Natick, MA) toolbox implementing all of the computations described; a database of invariant manifolds in the Sun-Earth and Earth-Moon systems, together with file processing and visualization routines; a study of transfers between the invariant manifolds of the Sun-Earth and Earth-Moon systems; sample trajectories designed with the method; and recommendations for future research.

The problem statement and approach are reviewed and discussed in more detail in the next chapter. In Chapter 3, theoretical aspects of the PCR3BP are introduced, and a dynamical treatment of invariant manifolds is given. Chapter 4 presents continuation methods for the computation of the periodic orbits from which invariant manifolds project. Methods for computing manifold transfers are presented in Chapter 5. This is decomposed into two categories: transfers between circular orbits about the Earth or the Moon and the manifolds in their respective systems, and transfers between Sun-Earth and Earth-Moon manifolds. In particular, for the latter, a novel method based on bounding low-energy transfer regions is developed. This method also motivates a new perspective on investigating manifold transfers by characterizing the transfer region energy surface; this potential extension is discussed in detail in Chapter 6. Various formulations and extensions of trajectory correction using four-body dynamics are introduced in Chapter 7. Chapter 8 concludes the report with a summary of results.

The restricted two-body problem (R2BP) is considered for circular orbits about a body; its dynamics are reviewed in Appendix A. A table of parameter values used is given in Appendix B. Appendix C derives the equations of motion for the PCR3BP. In Appendix D, the mathematical details of invariant manifold computation are explicitly presented. Appendix E derives coordinate transformations between the inertial, Sun-Earth rotating, and Earth-Moon rotating frames. The MATLAB toolbox and implementation details are documented in Appendix F.



# CHAPTER 2

## Low-Energy Transfers Between the Earth and the Moon

---

In this chapter, the problem statement, motivation, and approach are presented in more detail. In particular, the  $\Delta v$  measure of a low-energy transfer is defined. The standard Hohmann transfer orbit as an Earth-Moon trajectory is reviewed, and the consequences of its energy costs are analyzed. The use of invariant manifold theory to design low-energy Earth-Moon transfers is then motivated and discussed. Finally, an outline of the design method is given.

### 2.1 The $\Delta v$ Cost Function

In astrodynamics, a transfer trajectory from one orbit to another is often characterized by its  $\Delta v$  cost.

**Definition 2.1.** The  $\Delta v$  cost of an orbital transfer is the total magnitude of velocity change caused by engine thrust required for the execution of the transfer. For example, if a transfer requires engine thrusts corresponding to velocity changes  $\Delta v_1, \Delta v_2, \Delta v_3, \dots$  at distinct points along the transfer, then the  $\Delta v$  cost of the transfer is  $\Delta v = \sum_i |\Delta v_i|$ .

By a low-energy transfer, it is meant a transfer with a low  $\Delta v$ . Through the Tsiolkovsky rocket equation

$$\Delta v = v_e \log \frac{m_i}{m_f},$$

where  $v_e$  is the engine exhaust velocity,  $m_i$  is the wet mass (with fuel) of the spacecraft, and  $m_f$  is the dry mass (without fuel) of the spacecraft, the mass fraction  $\alpha$  of the propellant required for transfer may be computed from  $\Delta v$ :

$$\alpha \equiv 1 - \frac{m_f}{m_i} = 1 - e^{-\Delta v/v_e}.$$

Note that the exhaust velocity may be expressed as

$$v_e = I_{sp} g_0,$$

where  $I_{sp}$  is the specific impulse provided by the engine and  $g_0 = 9.80665 \times 10^{-3} \text{ km/s}^2$  is the gravitational acceleration at sea level on Earth.

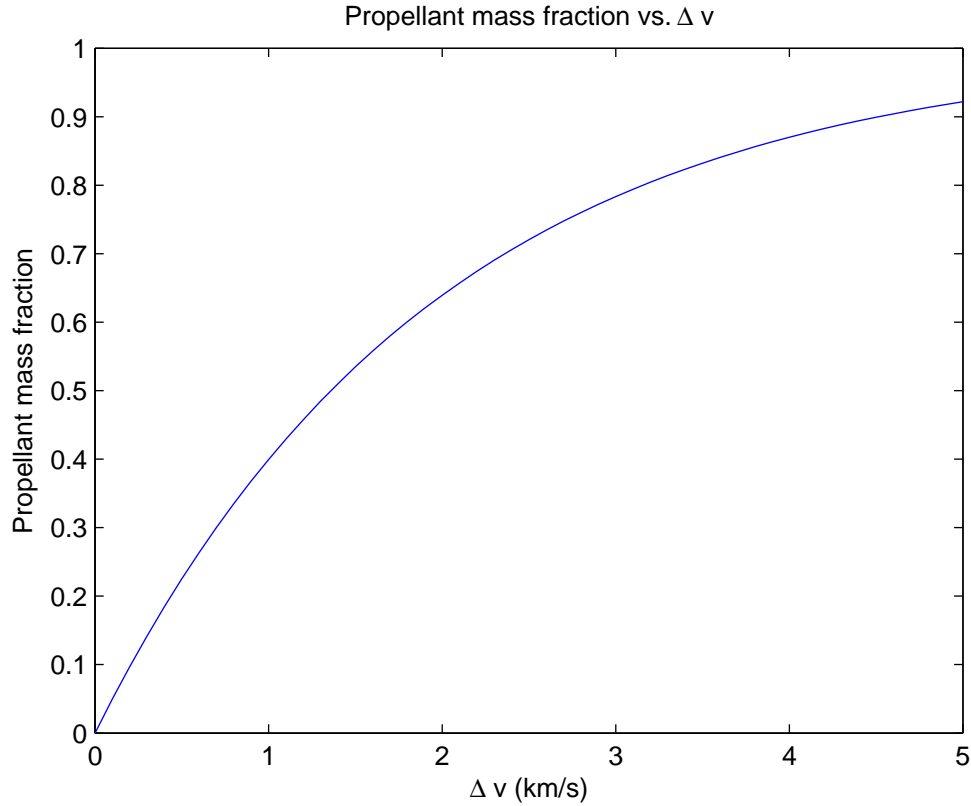


FIGURE 2.1. Propellant mass fraction as a function of  $\Delta v$  for a standard solid rocket booster providing specific impulse  $I_{sp} = 200$  s.

For a standard solid rocket booster providing specific impulse  $I_{sp} = 200$  s, the propellant mass fraction plotted as a function of  $\Delta v$  is shown in Figure 2.1. As the figure shows, for moderate values of  $\Delta v$  (say,  $\Delta v < 3$  km/s), even a modest decrease in the  $\Delta v$  cost results in a dramatic reduction in the required propellant mass fraction. This is especially true toward the lower end of the  $\Delta v$  spectrum. Thus, low-energy transfers significantly reduce the cost of a mission by decreasing the need for engine fuel. Alternatively, the spacecraft mass not required for propellant may be used for scientific equipment and other cargo. By either interpretation, low-energy transfers make viable again a variety of missions which were previously considered impossible. Thus, a general aim of space mission design is the minimization of the  $\Delta v$  cost function.

## 2.2 The Hohmann Transfer

The Hohmann transfer is a standard method of transferring from one circular orbit about a body to another. Hohmann transfers are designed by elongating the starting orbit into

an ellipse such that its apsis coincides with the ending orbit collinearly with the central body and the initial point of transfer. Two burns are required for this maneuver: one at the initial point of transfer to escape from the initial orbit, and another at the final point of transfer to insert into the final orbit. Under the dynamics of the restricted two-body problem (R2BP), it has been demonstrated that the Hohmann transfer is one of the most economical transfers available in the  $\Delta v$  sense. Therefore, it has become the standard in orbital transfers and provides a benchmark against which novel transfer methods may be compared.

The Hohmann transfer may be easily extended to a transfer from a circular orbit about a primary mass to a circular orbit about a secondary mass, where the secondary mass moves in a circular orbit about the primary mass. This describes the Earth-Moon system. Since the goal of this project is to investigate low-energy transfers from the Earth to the Moon, the  $\Delta v$  cost of transferring from an Earth orbit to a lunar orbit using the Hohmann transfer will now be computed.

This computation assumes familiarity with the R2BP; for a review, the reader is directed to Appendix A.

### 2.2.1 Earth Orbit

The spacecraft begins in a circular orbit about the Earth of distance  $r_E$  above the surface. Assume that the mass of the spacecraft is negligible compared to the mass of the Earth. Then the results of the R2BP apply, and the circular orbital velocity formula (A.5) gives the spacecraft orbital velocity

$$v_{EO} \equiv \sqrt{\frac{\mu_E}{R_E + r_E}},$$

where  $R_E$  is the radius of the Earth,  $\mu_E \equiv Gm_E$  is the gravitational constant of the Earth, where  $G$  is the gravitational constant and  $m_E$  is the mass of the Earth (for a table of parameter values used, see Appendix B).

### 2.2.2 The Hohmann Transfer Trajectory

Consider the Hohmann transfer from the specified Earth orbit to the orbit of the Moon about the Earth. Construct the ellipse containing the transfer trajectory; in this case, the initial and final points of transfer are the periapsis (point of minimum distance from the primary) and apoapsis (point of maximum distance from the primary), respectively, of the ellipse. Compute the velocity necessary to travel along that ellipse at periapsis from the elliptical orbital velocity formula (A.7):

$$v_P \equiv \sqrt{2\mu_E \left( \frac{1}{R_E + r_E} - \frac{1}{l + R_E + r_E} \right)},$$

where  $l$  is the radius of the Moon's orbit about the Earth. The velocity change required to transfer from the initial orbit to the elliptical orbit is therefore

$$\Delta v_1 \equiv v_P - v_{EO}.$$

### 2.2.3 Lunar Orbit

From (A.7), the velocity of the spacecraft at apoapsis is

$$v_A \equiv \sqrt{2\mu_E \left( \frac{1}{l} - \frac{1}{l + R_E + r_E} \right)}.$$

Assume that the spacecraft and the Moon meet at this point. It is convenient to consider the transfer into lunar orbit from the reference frame of the Moon. Therefore, compute the orbital velocity of the Moon about the Earth:

$$v_M \equiv \sqrt{\frac{\mu_E}{l}}$$

and apply a burn corresponding to

$$\Delta v_M \equiv v_M - v_A$$

to enter the lunar reference frame. Assume that the spacecraft is just outside of the influence of the Moon's gravitational field, and study the the reduced energy (A.3) of the spacecraft as  $r \rightarrow \infty$  to obtain

$$E = \frac{1}{2}v_\infty^2,$$

where  $v_\infty$  is the velocity “at infinity” in the lunar reference frame. For a mass just reaching infinity, then,  $v_\infty = 0$  gives  $E = 0$ , so by (A.4), a mass with zero velocity at infinity has velocity

$$v = \sqrt{\frac{2\mu_M}{r}}$$

at orbital radius  $r$  from the Moon, where  $\mu_M \equiv Gm_M$  is the gravitational constant of the Moon, where  $m_M$  is the mass of the Moon. Therefore, insertion into a lunar orbit of radius  $r_M$  above the surface of the Moon requires a decrease in velocity corresponding to

$$\Delta v_{LO} \equiv \left(1 - \sqrt{2}\right) \sqrt{\frac{\mu_M}{R_M + r_M}},$$

where  $R_M$  is the radius of the Moon. Both burns are applied together to obtain

$$\Delta v_2 \equiv \Delta v_M + \Delta v_{LO}.$$

The total cost of making the transfer is thus

$$\Delta v = |\Delta v_1| + |\Delta v_2|.$$

For a low Earth orbit of radius  $r_E = 200$  km and a lunar orbit of  $r_M = 1000$  km, the  $\Delta v$  cost of the Hohmann transfer with specific impulse  $I_{sp} = 200$  s is 3.4088 km/s. This corresponds to a propellant mass fraction of 0.8241. At this value of  $\Delta v$ , a 20% reduction to  $\Delta v = 2.7270$  km/s will reduce the propellant mass fraction to 0.7510, equivalent to a payload capacity increase of 7.31% of the spacecraft's wet mass. This is a significant increase; the advantages of using transfers with a lower  $\Delta v$  than the Hohmann transfer are thus clear.

### 2.3 Invariant Manifolds in the Planar Circular Restricted Three-Body Problem

While the Hohmann transfer is a very low-energy transfer when considered under the dynamics of the R2BP, it is important to realize that the R2BP is not a good approximation of the system at hand for the purposes of this project. For the low-energy transfers considered, the perturbations induced by the gravitational influences of the Sun and Moon are also important considerations. Thus, an adequate description of the problem really requires treatment of the four-body Sun-Earth-Moon-SC system.

Under the dynamics of this system, alternative solutions are permitted and potential trajectories with lower  $\Delta v$  costs than the Hohmann transfer become available. In fact, it is not immediately necessary to investigate the full four-body behavior of solutions. By considering the dynamics of two coupled three-body problems, the invariant manifold structure of the Interplanetary Superhighway introduced in Chapter 1 may be generated. These invariant manifolds support Earth-Moon transfers with significantly reduced  $\Delta v$  by allowing transfers to work with the gravitational structure of the system instead of against it.

For ease of analysis, the particular three-body problem considered is the planar circular restricted three-body problem (PCR3BP). The PCR3BP is defined in the following chapter. The invariant manifolds of the PCR3BP have been studied in extensive detail [4, 7, 10, 12–15, 19]; therefore, the method begins here.

### 2.4 Impulsive Low-Energy Earth-Moon Mission Design

As an approximation to the Sun-Earth-Moon-SC four-body system, two coupled PCR3BPs are considered: Sun-Earth-SC and Earth-Moon-SC. Near the Earth, the dynamics of the former are more valid; while near the Moon, the dynamics of the latter are

more valid. Locally, the three-body solutions are expected to be good approximations of solutions in the four-body system. Therefore, a mission trajectory may be designed piecewise with the local escape from the Earth and the local capture by the Moon given directly by the appropriate PCR3BP. In the intermediate region, a frame transfer is performed.

The local maneuvers about the Earth or the Moon are transfers between circular orbits and manifolds, and are the highest expected contributions to the  $\Delta v$  of the mission trajectory. This is because these transfers still likely have the qualitative characteristics of a Hohmann transfer in that some amount, albeit a smaller amount, of work against gravity is inevitably required. Thus, the  $\Delta v$  costs associated with these transfers are to be minimized. This minimization selects a subset of the invariant manifolds in each system; low-energy transfers between these selections are then investigated. In particular, only impulsive transfers, where the applied thrust is instantaneous, are considered. A consequence of this is that potential transfers will necessarily require spatial intersections.

Low-energy transfers between Sun-Earth and Earth-Moon manifolds may usually be achieved by varying the phase of the Moon about the Earth. Slight corrections may be needed at transfer, but these corrections have  $\Delta v$  costs that are expected to be much smaller (on the order of m/s) than those associated with transfers between circular orbits and manifolds. At this point, a frame transfer is also performed. Therefore, the two PCR3BPs are linked by manifold transfer.

Through this process, four trajectory pieces are created: transfer between an Earth circular orbit and a Sun-Earth manifold, transfer between a lunar circular orbit and an Earth-Moon manifold, the Earth-side of the manifold transfer, and the Moon-side of the manifold transfer. The trajectory obtained by patching these separate three-body solutions together will not be an actual trajectory in the four-body system. However, it should be a reasonably good approximation of one, hence a true four-body solution may be derived by correction using an appropriate four-body model. The choice of this four-body model controls the final accuracy of the mission trajectory. The four-body model considered for correction in this project is the bicircular model (Chapter 7).

In brief, then, the mission design process considered in this report is summarized as follows: first, the invariant manifolds of each PCR3BP are computed (Chapter 3); then transfers using these manifolds are investigated (Chapter 5); and finally, the patched three-body trajectory is corrected into an actual four-body solution (Chapter 7).

Using this method, an initial three-body guess of an Earth-Moon mission trajectory with  $\Delta v \approx 2.75$  km/s was achieved. This is a reduction of nearly 20% from the benchmark established by the Hohmann transfer. This trajectory has not yet been corrected in a four-body model.



# CHAPTER 3

## The Planar Circular Restricted Three-Body Problem

---

This chapter introduces the planar circular restricted three-body problem (PCR3BP). The significance of the Jacobi constant as a parameter of solution trajectories is discussed. A dynamical treatment of Lagrange points, Lyapunov orbits, and invariant manifolds is also given.

### 3.1 Introduction

In the general problem of three bodies, the aim is to determine the positions and velocities of all three bodies for all time, for any initial conditions, as acted upon by gravity. In the general case, there is no closed form solution. For a spacecraft moving under the influence of two celestial bodies, however, the three-body problem is well-approximated by the restricted three-body problem, where the mass of the third body—here, the spacecraft—is considered negligible compared to either of the other two. The problem can be further simplified by assuming that the two larger masses move in circular orbits about their barycenter. If it is further assumed that the third body travels in the same plane as the two larger bodies, then we have the PCR3BP.

**Definition 3.1.** The *planar circular restricted three-body problem (PCR3BP)* is a special case of the three-body problem with three assumptions:

1. The mass of the third body is negligible compared to either of the other two, hence only the gravitational forces of the two larger masses are considered;
2. The two larger masses move in circular orbits about their barycenter; and
3. The motion of all three bodies is constrained to the plane.

### 3.2 Equations of Motion

Let the two larger masses,  $m_1$  and  $m_2$ , where  $m_1 > m_2$  without loss of generality, rotate about their barycenter in circular orbits with constant angular velocity  $n$ . Since their orbits are circular, the distance from each body to the barycenter is fixed. Let  $R_1$  and  $R_2$  be this distance for  $m_1$  and  $m_2$ , respectively. Define  $\mu \equiv m_2/(m_1 + m_2)$  to be the

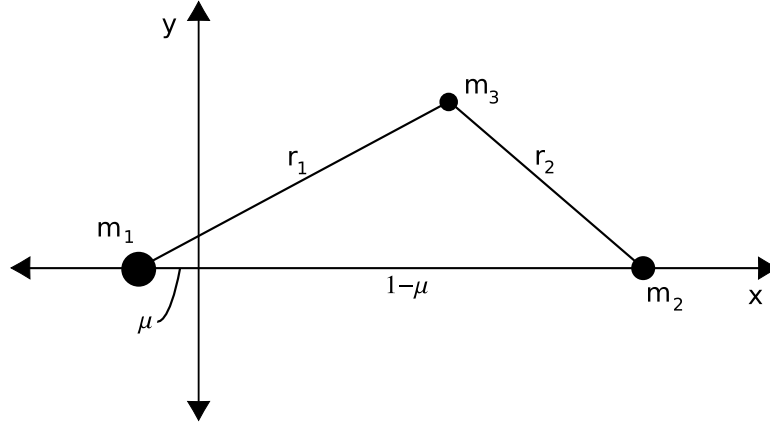


FIGURE 3.1. Schematic diagram of the PCR3BP in the non-dimensional rotating frame.

mass ratio of the system. Then  $R_1 = \mu l$  and  $R_2 = (1 - \mu)l$ , where  $l \equiv R_1 + R_2$  is the total distance between  $m_1$  and  $m_2$ . The system is non-dimensionalized as follows:

$$t \mapsto nt, \quad r \mapsto \frac{r}{l}, \quad m \mapsto \frac{m}{m_1 + m_2},$$

where  $t$ ,  $r$ , and  $m$  denote any measurements of time, distance, and mass, respectively. For example, the non-dimensional mass of the second body is  $m_2/(m_1 + m_2) = \mu$ .

In an inertial frame with origin at the barycenter, the positions and velocities of the masses  $m_1$  and  $m_2$  are explicit functions of time. If, however, the system is viewed from a non-inertial frame that rotates with angular velocity  $n$  (or 1 in non-dimensional units) with origin at the barycenter, then the standard coordinate  $(x, y)$  positions of  $m_1$  and  $m_2$  are  $(-R_1, 0)$  and  $(R_2, 0)$  (or  $(-\mu, 0)$  and  $(1 - \mu, 0)$  in non-dimensional units), respectively, and their velocities are zero. The PCR3BP is typically studied in the non-dimensional rotating frame. See Figure 3.1 for a schematic diagram.

In the non-dimensional rotating frame, the equations of motion for the position of the third body are

$$\begin{cases} \ddot{x} - 2\dot{y} = \Omega_x, \\ \ddot{y} + 2\dot{x} = \Omega_y, \end{cases} \quad (3.1)$$

where dot notation denotes differentiation with respect to time and subscripts denote partial differentiation, and

$$\Omega \equiv \frac{1}{2} (x^2 + y^2) + \frac{1 - \mu}{r_1} + \frac{\mu}{r_2} + \frac{1}{2} (\mu - 1) \mu,$$

where  $r_1$  and  $r_2$  are the distances from the third body to  $m_1$  and  $m_2$ , respectively. The state vector is therefore given by  $\mathbf{x} \equiv (x, y, \dot{x}, \dot{y})^\top$ . See Appendix C for a derivation.

It is important to note here that high-order numerical integration schemes such as the Runge-Kutta 7(8) method are required to maintain numerical accuracy in the integration of (3.1). For a discussion of such issues, see Appendix D.

### 3.3 The Jacobi Constant and Zero-Velocity Curves

The system (3.1) admits a quantity that is conserved for any solution. This quantity is called the Jacobi constant and is given by

$$J \equiv 2\Omega - (\dot{x}^2 + \dot{y}^2). \quad (3.2)$$

The Jacobi constant gives some insight into the qualitative behavior of trajectories in the PCR3BP. Set  $\dot{x} = \dot{y} = 0$  in (3.2) and plot the resulting zero-velocity curves implicitly defined by

$$J - 2\Omega = 0.$$

This gives a set of closed curves for each  $J$ , as shown in Figure 3.2. Solving for the velocity in the interior of these curves gives a complex value. This is unphysical, so the interior of the zero-velocity curves are regions forbidden to spacecraft with that associated  $J$ .

Figure 3.2 considers the zero-velocity curves of an arbitrary PCR3BP, where  $S$  denotes the larger mass (e.g., the Sun) and  $E$  denotes the smaller mass (e.g., the Earth). For sufficiently high  $J$ , the forbidden region completely encloses and divides the space around  $S$  and  $E$  (top left). No transfer between the bodies is possible. As  $J$  is decreased, the forbidden region retreats and neck regions form on either side of  $E$ . The subfigure in the top right shows the possibility of travel between  $S$  and  $E$ ; the subfigure in the bottom left also shows the possibility of travel to the external region through the neck on the far side of  $E$ . Further decreases to  $J$  result in the opening of the forbidden region on the far side of  $S$  as well (bottom right). For sufficiently low  $J$ , the forbidden region disappears completely, and the spacecraft is allowed to be in the entire space.

The Jacobi constant  $J$  therefore controls the types of transfers allowed in the PCR3BP. Parameterization of solution trajectories on  $J$  then gives a useful way of indexing through transfer trajectories.

### 3.4 Lagrange Points, Lyapunov Orbits, and Invariant Manifolds

This section describes the dynamical aspects of primary interest in the PCR3BP, including Lagrange points, Lyapunov orbits, and invariant manifolds. For details on their computation, see Appendix D.

The invariant manifolds of the PCR3BP are generated by the Lagrange point structure of the system.

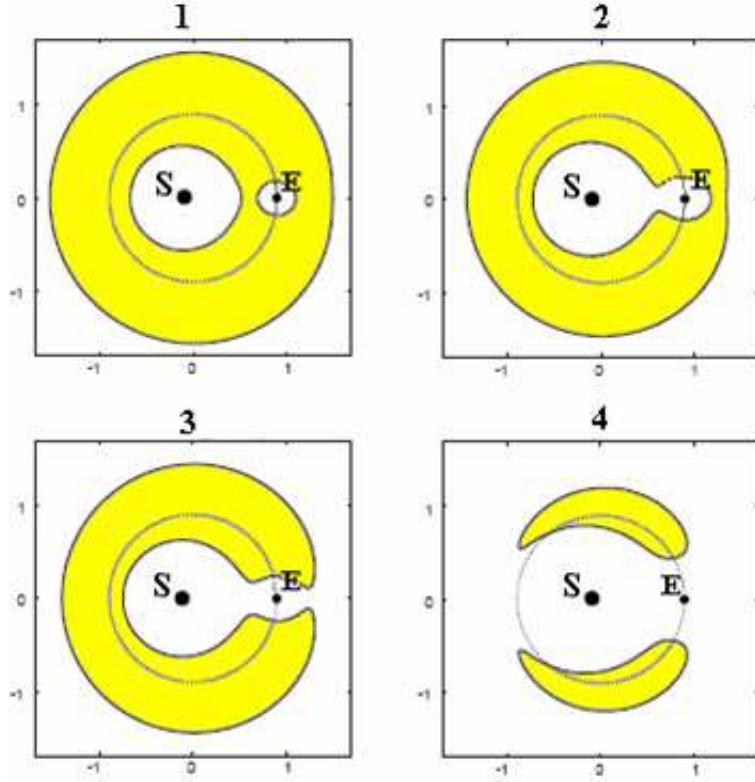


FIGURE 3.2. Zero-velocity curves of the PCR3BP for decreasing  $J$ .  $S$  is the larger mass (e.g., the Sun) and  $E$  is the smaller mass (e.g., the Earth). The yellow regions are forbidden to the spacecraft with that  $J$ .

**Definition 3.2.** The *Lagrange points*  $L_1, \dots, L_5$  of the PCR3BP are the equilibrium solutions of (3.1). Of the five, three are called the *collinear Lagrange points* ( $L_1, L_2, L_3$ ), and the other two are called the *triangular Lagrange points* ( $L_4$  and  $L_5$ ).

These Lagrange points are stationary only in the rotating frame. The locations of the Lagrange points are shown in Figure 3.3.

For the Sun-Earth and Earth-Moon systems, the Lagrange points are given the designations  $EL_i$  and  $LL_i$ , respectively, where the numbering of the subscript  $i$  corresponds to the numbering of the Lagrange points  $L_i$ . For this project, only the  $L_2$  Lagrange point of each system is considered; the choice of  $L_2$  was based on previous work [19]. For reference,  $EL_2$  is located at  $x = 1.0100$  in the non-dimensional Sun-Earth rotating frame, and  $LL_2$  is located at  $x = 1.1551$  in the non-dimensional Earth-Moon rotating frame.

It may be shown that the collinear Lagrange points are saddle-center equilibria. Therefore, Lyapunov orbits exist around these points [4].

**Definition 3.3.** A *Lyapunov orbit* is an unstable periodic orbit about a collinear La-

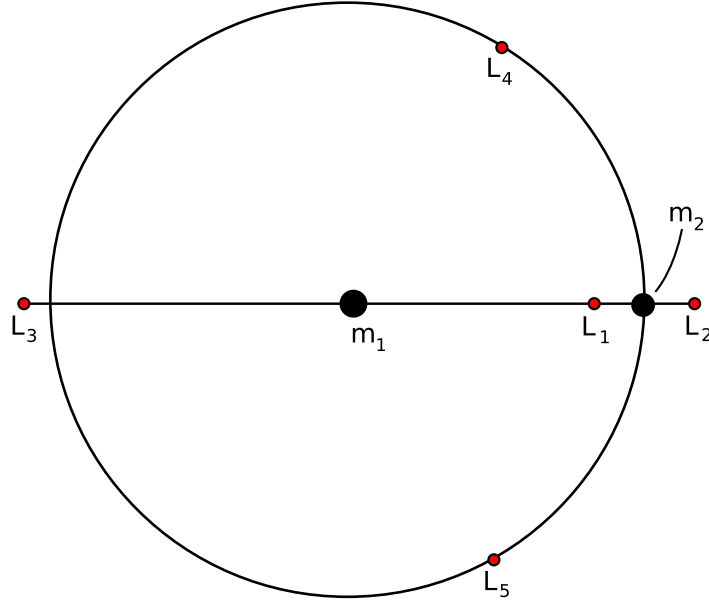


FIGURE 3.3. Lagrange points of the PCR3BP.

grange point that satisfies (3.1) at each point on the orbit.

Lyapunov orbits are computed in two steps: first, an approximation of a Lyapunov orbit is obtained; second, this approximation is differentially corrected to produce an actual Lyapunov orbit. One method for obtaining this initial approximation is through the linearization of (3.1) about the Lagrange point concerned: a periodic solution in the linearized system may be derived analytically and used as an initial guess close to the equilibrium region. Another method based on the extrapolation of Lyapunov orbital data is discussed in the next chapter. For details, see Appendix D.

These Lyapunov orbits are the gateways to the Interplanetary Superhighway. In Figure 3.2, the neck regions are centered about the collinear Lagrange points and are pushed outward by the Lyapunov orbits surrounding them. Thus, the Lyapunov orbits control transfers with Jacobi constants just below those of the Lagrange points in question. This control is exerted by the invariant manifold structure of the Lyapunov orbits.

**Definition 3.4.** An *invariant manifold* is a solution surface of (3.1) obtained by perturbation along the saddle directions of a Lyapunov orbit.

Each invariant manifold is associated with a Lyapunov orbit from which it projects. An invariant manifold is generated as follows. At each point on a Lyapunov orbit, the saddle directions of stability and instability may be computed. Perturbation along these directions followed by numerical integration of (3.1) (forward in time for instability, backward in time for stability) then generates a set of projecting trajectories. The

solution surfaces formed by these trajectories are the invariant manifolds corresponding to that Lyapunov orbit.

There are two types of invariant manifolds, corresponding to the stability of the perturbation direction.

**Definition 3.5.** A *stable manifold* is an invariant manifold generated by backward propagation of (3.1) along the stable direction of perturbation; an *unstable manifold* is an invariant manifold generated by forward propagation of (3.1) along the unstable direction of perturbation. The *stability type* of a manifold refers to whether it is stable or unstable.

When propagated forward in time, a trajectory on a stable manifold will converge to the Lyapunov orbit, while a trajectory on an unstable manifold will diverge from it. A set of invariant manifolds projecting from an  $LL_2$  Lyapunov orbit with  $J = 3.156616$  is shown in Figure 3.4. Manifold propagation issues are considered in detail in Appendix D; in particular, an adaptive perturbation magnitude scheme is developed to standardize the manifold propagation range.

It is important to note that there are two branches for each manifold propagated, corresponding to positive and negative perturbations along the saddle directions. It is convenient to introduce an heuristic definition here.

**Definition 3.6.** The *external branch* of a manifold, regardless of stability type, is the manifold that results when a perturbation with positive  $x$ -component is propagated; the *internal branch* of a manifold, regardless of stability type, is the manifold that results when a perturbation with negative  $x$ -component is propagated.

A particularly interesting dynamical property of invariant manifolds is that they are separatrices for the allowed motions of the PCR3BP [7, 8]. Therefore, the types of transfers available are determined by the invariant manifold structure of the system. Furthermore, the invariant manifolds guide the behaviors of nearby trajectories as they separate the solution phase space into distinct regions. Thus, invariant manifold theory may be used to design mission trajectories which do not lie on any particular manifold, but are nevertheless influenced by the manifold dynamics of the system. In this way, the invariant manifolds give a global characterization of the qualitative dynamics of the system.

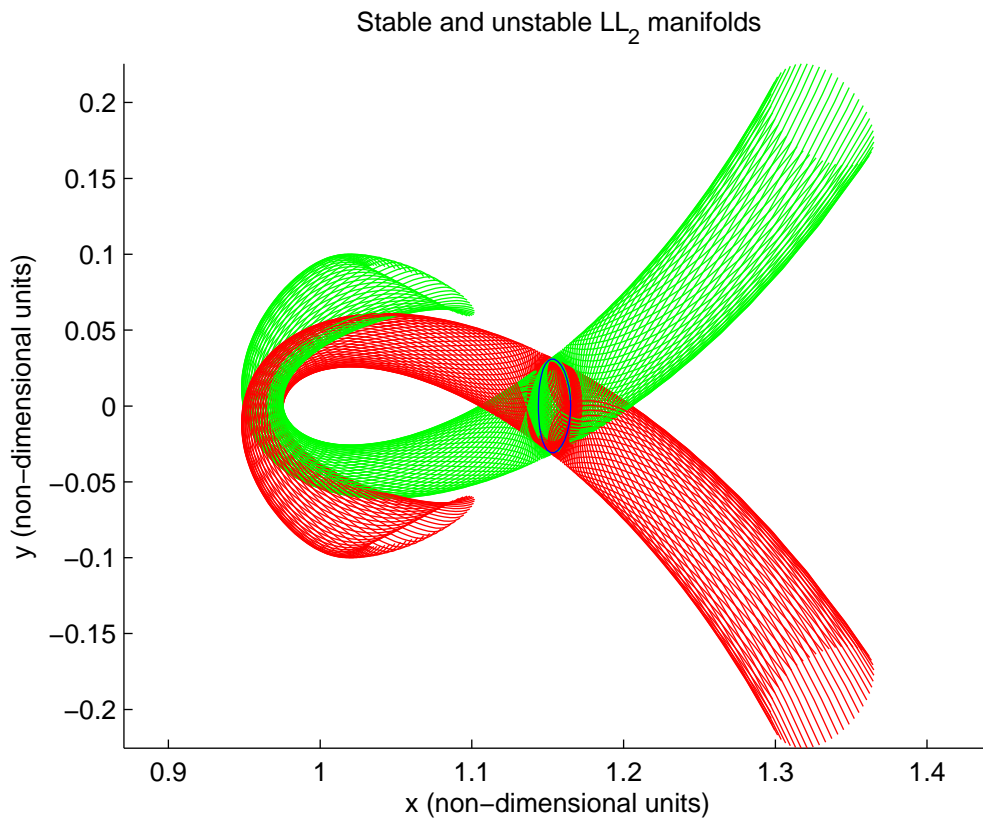


FIGURE 3.4. Invariant manifolds projecting from  $LL_2$  in the Earth-Moon rotating frame. Green, stable manifold; red, unstable manifold. Blue,  $LL_2$  Lyapunov orbit with  $J = 3.156616$ . The manifolds branches projecting to the right are the external branches of each manifold; those projecting to the left are the internal branches.





# CHAPTER 4

## *Continuation Methods for Lyapunov Orbits*

---

In this chapter, the limitations of the linearization method in producing initial guesses for large Lyapunov orbits as introduced in Chapter 3 are discussed. A continuation method, based on the continuous variation of Lyapunov orbits, is presented as a way to extend the range of Lyapunov orbits computed. Results of the method applied to the Sun-Earth and Earth-Moon systems are provided.

Continuation methods are required since the manifolds projecting from the Lyapunov orbits derived from the linearization method do not intersect with the Earth in the Sun-Earth system. Under the assumption of impulsive thrusts, this means that no transfer is possible. Thus, a method to obtain manifolds which do permit these intersections is required.

Typically, manifolds projecting from larger Lyapunov orbits have more intersections with the region about the smaller mass in the PCR3BP. Thus, the continuation method is required for Earth-Moon mission design.

### 4.1 Breakdown of the Linearization Method

The linearization method outlined in Appendix D for computing Lyapunov orbits breaks down at large amplitudes, providing smaller orbits than required for Earth-Moon mission design. (A demonstration of this will be shown in the next section when the proper terminology has been defined.) The method is said to break down if the linear approximation cannot be corrected to an actual Lyapunov orbit within a set number of iterations of the differential corrector used (see Appendix D for details). This number was chosen heuristically to be 30 iterations; for comparison, most corrections which did not break down converged in less than 10 iterations (for the default tolerance of  $10^{-8}$ ; see Appendix D).

A Lyapunov orbit may be identified by a number of different parameters. For this purpose, we use the initial condition of an orbit.

**Definition 4.1.** The *initial condition* of a Lyapunov orbit is the coordinate  $(x_0, y_0, \dot{x}_0, \dot{y}_0)^T$  on the orbit at an angle  $\theta = 0$  in the standard axial system centered at the Lagrange point which the orbit encloses.

Each orbit is uniquely identified by its initial condition. Another useful identifier is the  $x$ -amplitude of an orbit.

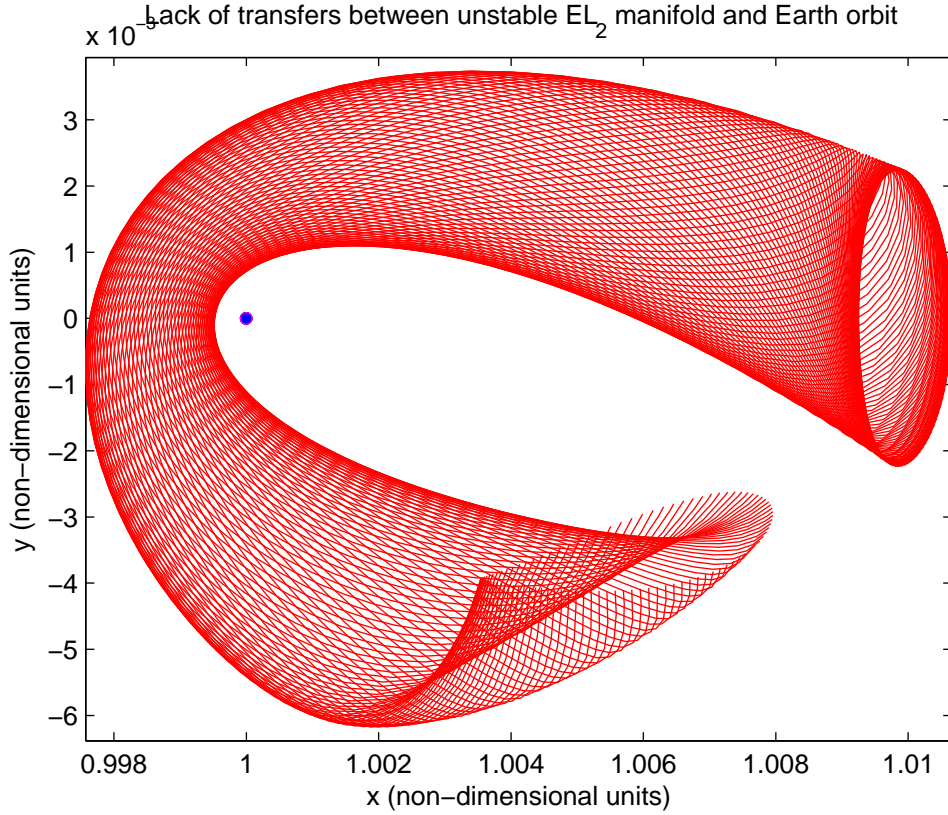


FIGURE 4.1. Lack of transfers between the internal branch of the unstable  $EL_2$  manifold (red) projecting from a Lyapunov orbit with  $A_x = 0.00065$  and Earth orbit (magenta). The blue circle is the Earth.

**Definition 4.2.** The  $x$ -amplitude  $A_x$  of a Lyapunov orbit is the distance  $|x_0 - l|$ , where  $x_0$  is the  $x$ -coordinate of the initial condition of the orbit, and  $l$  is the  $x$ -coordinate of the Lagrange point which the orbit encloses.

The linearization method breaks down at  $x$ -amplitudes of  $A_x \approx 0.00065$  and  $A_x \approx 0.04$  in the Sun-Earth and Earth-Moon systems, respectively.

## 4.2 Extrapolation of Initial Conditions for Lyapunov Orbits

This limitation must be overcome because Lyapunov orbits with  $A_x > 0.00065$  in the Sun-Earth system are required for manifold intersections with the space near the Earth. A demonstration is given in Figure 4.1, where the internal branch of the unstable manifold projecting from  $EL_2$  Lyapunov orbit with  $A_x = 0.00065$  is shown. Notice that the manifold does not intersect the Earth orbit chosen, hence no transfer is possible.

In order to compute the required Lyapunov orbits with larger  $A_x$ , a continuation

method is applied. This continuation method depends on the assumption that the Lyapunov orbits of the PCR3BP vary continuously in their initial conditions. As discussed in Appendix D, due to certain symmetries in the equations of motion, the  $y$ - and  $\dot{x}$ -coordinates of an initial condition are necessarily zero. Thus, there are two free coordinates ( $x$  and  $\dot{y}$ ) with which to specify a Lyapunov orbit. The general aim of the continuation method is to compute one of the remaining coordinates as a function of the other from data generated by the linearization method.

Sets of data may be generated for each system by storing the initial conditions derived at increasing  $x$ -amplitudes produced by the linearization method until the breakdown point. These data are then used by the continuation method to compute Lyapunov orbits with larger  $A_x$  by extrapolation. These extrapolations are, in turn, used to generate more data according to the following algorithm: take the largest  $x$ -coordinate in the data, increase it by a step size (whose value depends on the system), and extrapolate from the data to find the corresponding  $\dot{y}$  for a Lyapunov orbit. Here cubic splines were used for extrapolation as it was found that the initial condition data was nonlinear. This  $(x, \dot{y})$  pair is then added to the data. The period is obtained by integration.

A visualization of the data is shown in Figure 4.2. In the top left subfigure,  $LL_2$  Lyapunov orbits are shown. The blue orbits computed using the linearization method are shown until the linearization breakdown point; continuation methods then take over, computing the orbits shown in red until the continuation breakdown point. It is easily seen that the size of the Lyapunov orbits computed increase significantly with the use of the continuation method. Also shown in this figure are the nonzero coordinates  $(x, \dot{y})$  of the initial conditions of the Lyapunov orbits (top right). Dots denote the coordinates obtained by the appropriate approximation (blue, linearization; red, continuation); lines connect the corrected data. The initial conditions obtained is slightly nonlinear, so the cubic spline is used to fit the observed curve. Similarly, the periods of the Lyapunov orbits are also shown (bottom left). Of particular interest is the fact that the period is constant in the linearized approximation. Finally, the number of iterations of the differential corrector required for convergence to an actual Lyapunov orbit from the initial guesses obtained by both methods are shown in the subfigure in the bottom right. More Lyapunov orbits may be found by setting a lower tolerance in the differential corrector (see Appendix D).

The continuation method applied with fixed step sizes of 0.0001 and 0.00001 for the Earth-Moon and Sun-Earth systems, respectively, allows the computation of Lyapunov orbits with  $x$ -amplitudes of up to  $A_x = 0.0742$  and  $A_x = 0.001865$ , respectively, using the default differential corrector tolerance of  $10^{-8}$ . These correspond to increases of  $\Delta A_x = 0.0342$  and  $\Delta A_x = 0.01215$ , respectively. After this point, the continuation method breaks down.

Interpolation of the data within the range of initial conditions stored then gives accurate approximations of Lyapunov orbits which are then easily corrected. The larger Lyapunov orbits so obtained give manifolds which now intersect with circular orbits about the Earth (see Chapter 5), and so allows us to find the required low-energy transfers.

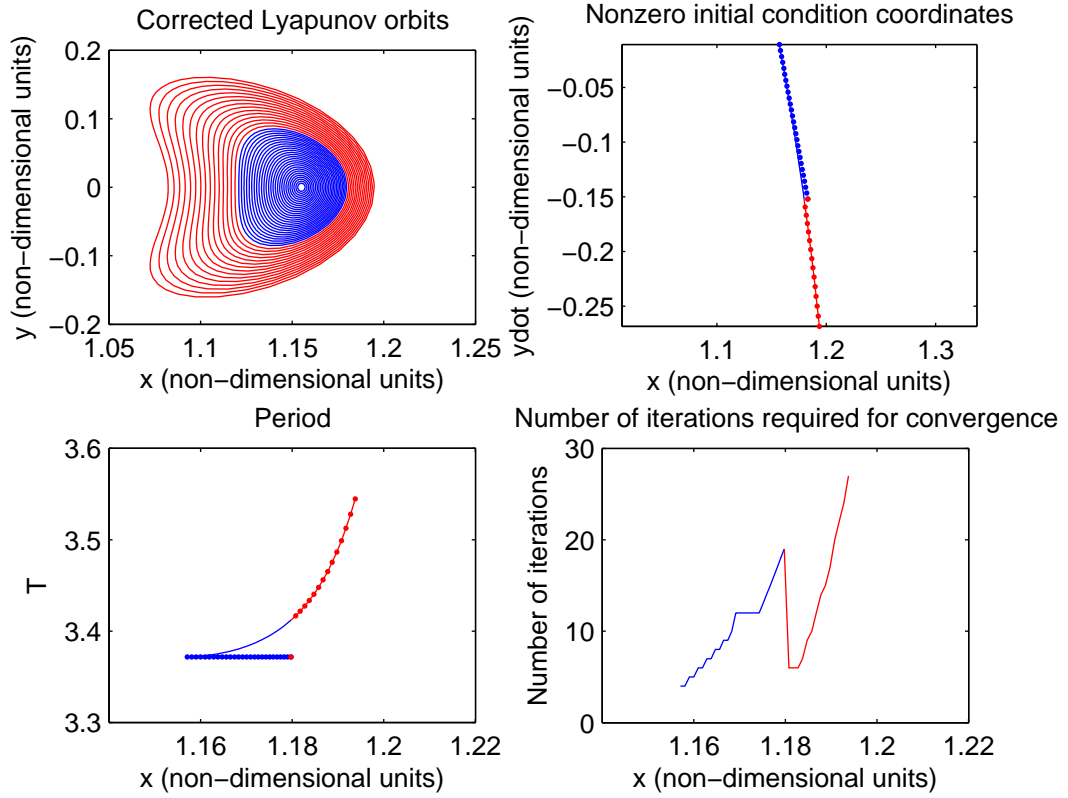


FIGURE 4.2. Data generated by the continuation method. Blue, data derived using the linearization method; red, data derived using the continuation method. **Top left:** Corrected Lyapunov orbits with orbits obtained by both methods plotted up to their respective breakdown points. **Top right:** Nonzero initial condition coordinates of corrected Lyapunov orbits. Dots denote initial data from the approximations; lines connect the corrected data. **Bottom left:** Periods of corrected Lyapunov orbits. Dots denote initial data from the approximations; lines connect the corrected data. **Bottom right:** Number of iterations required for the differential corrector to produce Lyapunov orbits from the approximations.

The results of the continuation method discussed here facilitate the computation of an invariant manifold database cataloguing possible Sun-Earth and Earth-Moon manifolds to be used for mission design (see Appendix F for details).



# CHAPTER 5

## *Invariant Manifold Transfers*

---

In Chapters 3 and 4, the process of computing invariant manifolds suited to the task of low-energy Earth-Moon transfer was outlined. The question then remains as to how these manifolds might be used to design actual mission trajectories. This problem is approached by first considering the types of transfers available using these manifolds. In this chapter, methods for computing candidate transfer points are discussed.

In our application, invariant manifold transfers are separated into two categories: transfers between circular orbits about the Earth or the Moon and the manifolds in their respective systems, and transfers between Sun-Earth and Earth-Moon manifolds. The method used in the first is relatively straightforward; in fact, this first case may be reduced to the second by considering a circular orbit as a degenerate manifold in our implementation. The second case is much less well understood and hence is of much more interest; it is responsible for the bulk of the material presented here.

For this case of direct manifold-manifold transfer, two methods are presented. The first is the Poincaré section, whose advantages and disadvantages we describe. Previous work in manifold transfers has made extensive use of the Poincaré section. Indeed, the power of the Poincaré section in the planar case considered was part of the original motivation for choosing the PCR3BP. The drawbacks of the Poincaré section in our particular application, however, ultimately motivate the development of a new method of studying manifold transfers. This is the second method presented and considers the bounding of low-energy transfer regions.

This low-energy transfer region boundary method is a novel approach to the problem of manifold transfers. Thus, its theoretical development and implementation are explained in detail. Extensions of this method are also discussed. A minor implementation extension regarding the density control of low-energy transfers is included in this chapter; the more major extension of the characterization of the  $\Delta v$  surface between Sun-Earth and Earth-Moon manifolds is given its own treatment in Chapter 6. The chapter concludes with a discussion on how the transfer region boundary method may be used with the manifold database for mission design.

### **5.1 Transfers Between Circular Orbits and Manifolds**

The problem of transferring between circular orbits and manifolds is considered first. In order to complete a low-energy transfer between the Earth and Moon, the transfers between invariant manifolds and circular orbits of the Earth and the Moon must be studied. The trajectory designed here begins in a low circular orbit around the Earth

and ends in a circular orbit around the Moon. By convention, set a low Earth orbit (LEO) to be at 200 km above the planet's surface and a lunar orbit (LO) to be at 1000 km. The stability properties of the manifolds then determine which are considered for use in a final trajectory. For the Sun-Earth system, an intersection of the stable manifold from  $EL_2$  with LEO is desired. For the Earth-Moon system, an intersection of the unstable manifold from  $LL_2$  with LO is desired. Both of these intersections can be studied using the same methods, by merely changing parameters such as the mass ratio  $\mu$  and the radius of the orbit. These intersections are considered in the non-dimensional rotating frame for which the body whose circular orbit is of concern is the smaller mass of the associated PCR3BP.

Transfers between circular orbits and manifolds are studied first because these transfers give the highest expected contributions to the  $\Delta v$  of the entire mission trajectory. The majority of the manifolds considered are consequences of the continuation methods described in Chapter 4.

### 5.1.1 Circular Orbit About a Stationary Body

The first step is to study the conditions needed for a spacecraft to remain in a circular orbit around a planetary mass. To do this consider the restricted two-body problem (R2BP) of either the Earth-SC or Moon-SC systems, and solve for the orbital velocity using (A.5). Here motion in the circular orbit is taken to be counterclockwise around the larger mass. For more information on the R2BP, see Appendix A.

### 5.1.2 Parametric Search of Intersections with Manifolds

Using (A.5), a function was written in MATLAB which takes as input any  $(x, y)$  point and finds the velocity needed to stay in a circular orbit around the specified body with a radius  $r \equiv \sqrt{x^2 + y^2}$ , i.e.,  $r$  is the distance from this point to the central body positioned at the origin. Using this and intersection code developed for calculating manifold spatial intersections (see the following sections), the trajectories comprising each manifold (as computed in the database) that intersect with either LEO or LO, depending on the case considered, can be found.

An example of one of these intersections is shown in Figure 5.1, which considers the intersection of an unstable  $LL_2$  manifold with LO. The trajectory identified in black is a candidate for the final transfer in a full Earth-Moon trajectory. Once trajectories within a manifold are found, either from the Earth or to the Moon, the  $\Delta v$  required to leave LEO or enter LO, respectively, at each intersection point can be calculated from the velocity on the manifold and that of the circular orbit.

Using the database, a parametric search through the manifolds, indexed by the Jacobi constant, was implemented to find all trajectories which intersect LEO and LO. The search ran through only the internal branches of the stable and unstable manifolds in the Sun-Earth and Earth-Moon systems, respectively. It was found that the Jacobi constants



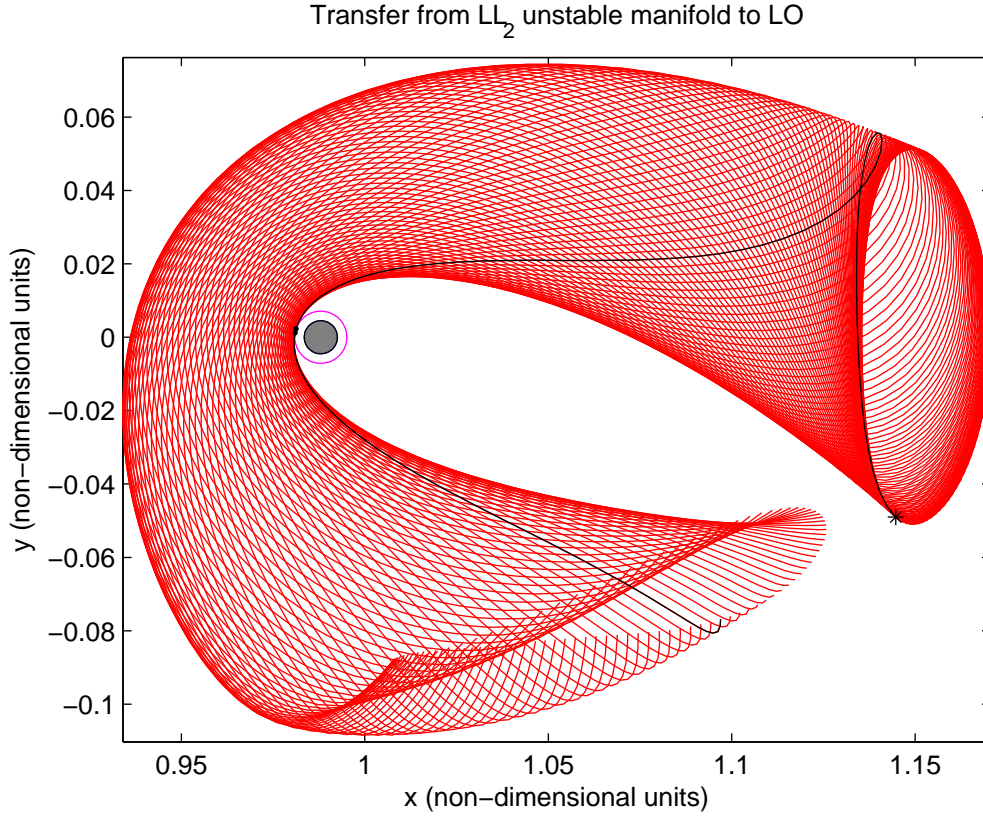


FIGURE 5.1. Intersection of unstable  $LL_2$  manifold (red) with LO (magenta) at a distance of 1000 km above the Moon's surface (gray) in the non-dimensional Earth-Moon rotating frame. The black curve denotes a trajectory that intersects this orbit with the star representing its initial condition on the Lyapunov orbit about  $LL_2$  (red dot).

for the transfers with the lowest  $\Delta v$  are  $J_{SE} = 3.000816144$  and  $J_{EM} = 3.150493$  for LEO and LO, respectively, where  $J_{SE}$  is the Jacobi constant in the Sun-Earth frame and  $J_{EM}$  is the Jacobi constant in the Earth-Moon frame. These values of  $\Delta v$  are correspondingly 2.2518 km/s and 0.4930 km/s. These values thus provide an estimate of the  $\Delta v$  achievable for the full Earth-Moon trajectory using the method:  $\Delta v \approx 2.75$  km/s.

The trajectories requiring the lowest  $\Delta v$  were then used as pieces of the patched initial guess of the full mission trajectory.

## 5.2 Transfers Between Sun-Earth and Earth-Moon Manifolds

With methods for transferring between circular orbits and manifolds in place, the only remaining problem is to link the coupled PCR3BPs together by finding low  $\Delta v$  transfers between their invariant manifolds.

### 5.2.1 Coordinate Transformations

As seen in Chapter 3, the invariant manifolds of each PCR3BP are computed in the local rotating frame. In order to investigate manifold intersections between PCR3BPs, the invariant manifolds must be transformed into a common reference frame. The coordinate transformations outlined here are derived in detail in Appendix E.

The non-dimensional Sun-Earth rotating frame is chosen as the common reference frame. With this choice, only the transformation from the non-dimensional Earth-Moon rotating frame to the non-dimensional Sun-Earth rotating frame needs to be computed. The transformation takes place in three steps: first, the non-dimensional Earth-Moon rotating coordinates are dimensionalized; then, the dimensional Earth-Moon rotating coordinates are transformed to the dimensional Sun-Earth rotating frame by using the bicircular model (see Chapter 7); and finally, the dimensional Sun-Earth rotating coordinates are non-dimensionalized.

## 5.3 Poincaré Sections

The first method considered for intersecting Sun-Earth and Earth-Moon manifolds is the Poincaré section, which is used to analyze the problem by dimensional reduction. To construct a Poincaré section, one coordinate is restricted (a spatial coordinate, in our case, since impulsive thrusts are assumed), thereby cutting the manifold at a hyperplane. The projection of the remaining coordinates for each manifold are then considered. See Figure 5.2 for a schematic diagram. By dimensional reduction, the Poincaré section allows us to better visualize the nature of these intersections.

In the full three-space case, the high dimensionality of the state vector (six coordinates are necessary) makes the Poincaré section difficult to apply. In the planar case, however, the useful constraint provided by the Jacobi constant makes the method viable. The steps of the Poincaré section are enumerated below:

1. Restrict one coordinate (e.g., the spatial coordinate  $x$ ).
2. Plot two of the remaining coordinates (e.g.,  $y$  against  $\dot{y}$ ).
3. The manifold intersections are given by the intersections of this plot, as the last coordinate may be computed from the other three by using the Jacobi constant (for velocities, this is given up to sign; for positions, the equation is nonlinear).

Thus, in the planar case, the nature of these intersections is given completely by a simple two-dimensional plot.

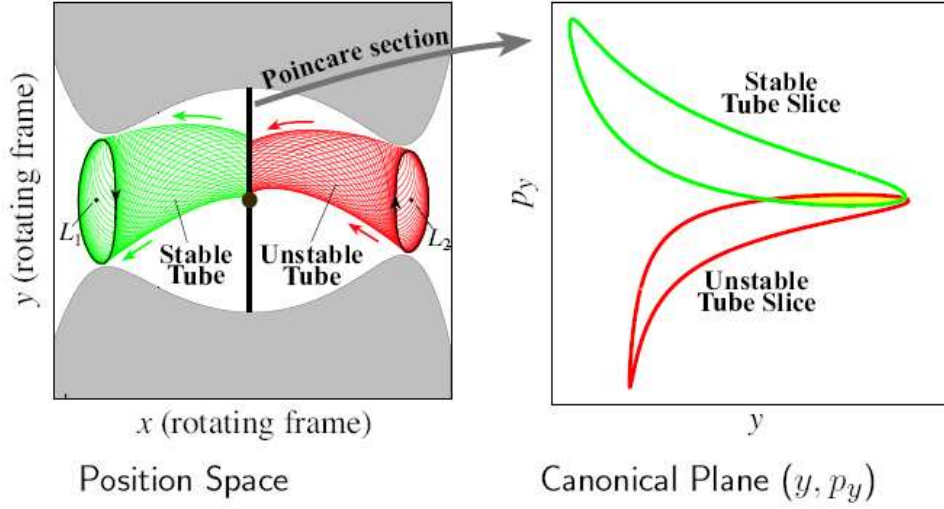


FIGURE 5.2. Schematic diagram of a Poincaré section. From a spatial manifold intersection ( $x = 1 - \mu$ ), a map is created by plotting the coordinate  $y$  against  $\dot{y}$  ( $p_y$  in the figure). The intersections of these projected curves mark intersections of the manifolds in all four coordinates. Green, stable manifold from  $L_1$ ; red, unstable manifold from  $L_2$ . Image courtesy of Ross (2002).

The Poincaré section has been used extensively to study manifold intersections in previous work [12, 13, 15, 19], but when approaching a problem such as that considered in this report, which involves manifolds belonging to two independent systems, there arises the difficulty of choosing where to place the cut. When manifolds from the same system intersect, natural choices for candidate transfers exist due to symmetry considerations, but this intuition is lost in the multi-system case. Therefore, for the particular problem considered, the Poincaré section suffers from a fundamental arbitrariness regarding the placement of the hyperplane cut. Admittedly, it is possible to take cuts at regular points along an interval and search for intersections that way, but this is not a particularly computationally efficient approach.

Thus motivated, the project direction turned to the investigation of a new method which remains visual, but that removes the limitations of the Poincaré section. Moreover, the method should be designed for significant interaction with the manifold database. In particular, intersections analyses should be systematic and easily automated. The method designed considers the computation of regions of low-energy transfer.

## 5.4 Low-Energy Transfer Regions

A low-energy transfer region is defined as follows.

**Definition 5.1.** A *low-energy transfer region* is a region which bounds points of local

spatial intersection between manifolds that correspond to a low  $\Delta v$  of transfer. More precisely, if the intersecting trajectories on each manifold have coordinates  $(x, y, \dot{x}_1, \dot{y}_1)^\top$  and  $(x, y, \dot{x}_2, \dot{y}_2)^\top$ , respectively, at the spatial intersection, then the low-energy transfer region bounds all local points with  $\Delta v = \|(\dot{x}_1, \dot{y}_1) - (\dot{x}_2, \dot{y}_2)\|$  below a certain tolerance.

Points in a low-energy transfer region are likely to give points of low- $\Delta v$  transfer. Thus, the problem of finding low-energy transfer regions is considered. In particular, the boundaries of these regions are considered.

It is important to note that only impulsive thrusts are considered in this project. As a consequence, a transfer between manifolds necessarily requires a spatial intersection of those manifolds. Thus, the initial step of any investigation of manifold intersections is to compute their spatial intersections. Once spatial intersections have been computed, the velocity coordinates of each manifold at those intersections may be determined (perhaps by interpolation), thus directly giving a measure of the  $\Delta v$  cost. A characterization of whether a low-energy transfer exists then follows immediately.

## 5.5 Transfer Region Boundaries by Polygon Construction

Assume that points of possible low-energy transfer are available. It is useful to introduce the following notation.

**Definition 5.2.** The *manifold type* of a point  $(x, y, \dot{x}, \dot{y})^\top$  refers to the manifold to which it belongs. If two manifolds are considered, then points on the first and second manifold may be called of manifold type 1 and 2, respectively.

Consider each point in the following form:  $\mathbf{x} \equiv (x, y, \dot{x}_1, \dot{y}_1, \dot{x}_2, \dot{y}_2)^\top$ , where  $(\dot{x}_i, \dot{y}_i)$  are the velocity coordinates of the point of manifold type  $i$  at the spatial coordinates  $(x, y)$ . Let  $X$  be the set containing all such  $\mathbf{x}$ .

These points are distributed in four-dimensional space. It is natural, therefore, to consider taking the four-volume of the space enclosed by these points as a low-energy transfer region, subject to the condition that it may be more appropriate to consider multiple distinct such spaces. For ease of application, consider only planar projections of this space. Polygons constructed about these points and their areas then give reasonable approximations of low-energy transfer regions.

## 5.6 Types of Boundary Polygons

Several types of polygons are used to construct boundaries of low-energy transfer regions. Three types are considered in this method: the total polygon, the intersection polygon, and the spatial polygon.

### 5.6.1 The total polygon

The first polygon considered is the total polygon.

**Definition 5.3.** The *total polygon* is the polygon constructed from the velocity coordinates of all  $\mathbf{x} \in X$ , regardless of manifold type.

In other words, for each  $\mathbf{x} \in X$ , the total polygon considers both the points  $(\dot{x}_1, \dot{y}_1)$  and  $(\dot{x}_2, \dot{y}_2)$  and bounds the set of points constructed by considering all such  $x$ . The total polygon bounds the total region in velocity space considered for low-energy transfer and gives an expectation of the amount of  $\Delta v$  needed for transfer.

### 5.6.2 The intersection polygon

However, it is entirely possible that there are regions of the total polygon in which only points of one manifold type lie. Thus, if low-energy transfers approaching the limit of  $\Delta v = 0$  are desired, then it may be more useful to consider the intersection polygon.

**Definition 5.4.** The *intersection polygon* is the intersection of the polygons  $P_1$  and  $P_2$ , where  $P_i$  is the polygon constructed from the velocity coordinates of all  $\mathbf{x} \in X$  of manifold type  $i$ , i.e.,  $(\dot{x}_i, \dot{y}_i)$ .

The intersection polygon is highly likely to contain points of exact intersection (this is dependent on the actual geometries of these polygons), so the region bounded by the intersection polygon gives a rough approximation of the space in which transfers of very low  $\Delta v$  lie.

### 5.6.3 The spatial polygon

A third boundary polygon that may be useful to consider is the spatial polygon, which may be most conveniently described as the total polygon in position space.

**Definition 5.5.** The *spatial polygon* is the polygon constructed from the spatial coordinates of all  $\mathbf{x} \in X$ , regardless of manifold type.

The spatial polygon gives a measure of the range over which transfers are possible in position space. Note that the position space analogues of the total and intersection polygons are identical given impulsive thrusts.

## 5.7 Polygon construction

In general, the task of constructing a suitable polygon from a set of points is not simple. We use the Polygon Clipper routine written by Sebastian Hölz, obtained online from the MATLAB Central File Exchange for many functions which would otherwise be very difficult to implement. The Polygon Clipper routine essentially gives the ability to perform set theoretic operations on polygons, e.g., take differences, unions, and intersections. Thus, the problem may be reduced to that of constructing many small polygons from which to build large polygons using the union function of Polygon Clipper.

MATLAB implements the Delaunay triangulation (`delaunay`), which may be used to good effect in constructing a covering of triangles over the points of interest. These triangles may then be unioned to obtain a full polygon containing all of the points.

However, the polygon so constructed is necessarily convex by virtue of the triangulation. Thus, for points which do not admit this geometry, we have to consider a modified approach. A useful method is to consider the polygon  $P$  as the union  $P \equiv \cup P_{ij}$ , where each  $P_{ij}$  is a convex polygon. This may be implemented by enforcing a grid partition  $(x_1, \dots, x_m), (y_1, \dots, y_n)$  on the set of points of interest. Letting each  $P_{ij}$  be the polygon constructed as discussed above by the union of triangulations on all  $(x, y) \in [(x_i, x_{i+1}), (y_j, y_{j+1})]$  then completes the construction.

In practice, there may be issues with computing overlaps of the  $P_{ij}$ , so we relax the grid constraints and construct  $P_{ij}$  based on the points  $(x, y) \in [(x_{i-1}, x_{i+1}), (y_{j-1}, y_{j+1})]$ .

An example of the use of the three polygons described above is given in Figure 5.3.

## 5.8 Extension: Density Control by Grid Selection

An interesting extension presents itself as a consequence of the polygon construction scheme employed. More precisely, the triangulation scheme applied may be used as a clever way to set a tolerance on the density of the transfer point distributions.

Under the grid partition used, there are two cases: there are three or more points in the gridded region under consideration, or there are fewer than three points in the gridded region. In the first case, a triangle is constructed, and the polygon union proceeds as outlined. In the second, no triangle is constructible, hence those points which do lie in that region are effectively disregarded. This, in effect, sets a tolerance on the density of the transfer point distribution.

An interesting problem is to determine whether there exists an method of controlling this density tolerance as a function of the grid partition. Roughly speaking, by relaxing the grid separation, the tolerance is decreased; while the tolerance is increased if more partitions are made. Although a bit of a digression, this is nevertheless an interesting problem to consider.

### 5.8.1 Transfer Region Boundaries for Mission Design

The transfer region boundary developed may be used in conjunction with the database to create rankings of manifold pairs for potential low-energy transfer. Three metrics to induce this ranking that fit easily into this framework are the areas of the total, intersection, and spatial polygons. Although it is nowhere claimed that these polygons give particularly well defined results on the types of transfers located in their interiors (for example, not all points within the polygons give good transfers, but all good transfers recorded are accounted for by these polygons), these areas should still give us a reasonably good idea of how well two given manifolds intersect in that manifold pairs which score

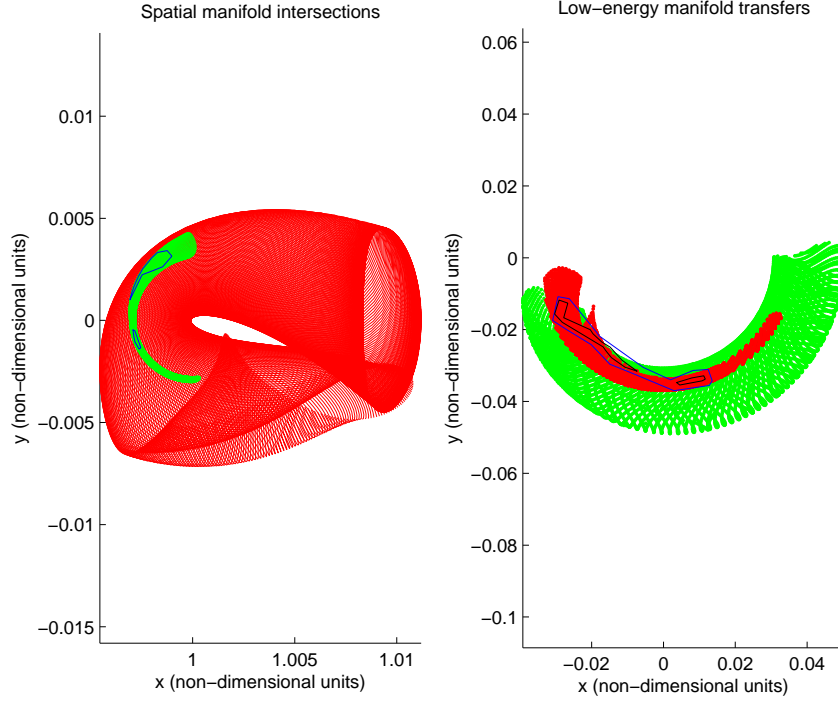


FIGURE 5.3. Regions of potential low-energy transfer between manifolds.  $A_x^{EM} = 0.05$ ,  $A_x^{SE} = 0.001$ . **Left:** the manifolds in position space. Red, unstable  $EL_2$  manifold directed toward the Earth; green, stable  $LL_2$  manifold directed away from the Earth. The blue points mark interpolated spatial intersections of the manifolds. The blue polygon is the spatial polygon for this manifold pair and encloses the region of points in position space for which low-energy transfer is likely.  $A_{sp} = 1.0768 \times 10^{-6}$ . **Right:** the velocity coordinates of each spatial intersection as marked off in the left figure. Green dots, velocity coordinates of points on the stable  $LL_2$  manifold; red dots, velocity coordinates of points on the unstable  $EL_2$  manifold. The blue polygon is the total polygon and encloses all velocity projections of the blue points in the left figure. The black polygon is the intersection polygon and is a region of possible zero-correction transfer.  $A_{tot} = 2.1108 \times 10^{-4}$ ,  $A_{int} = 5.6961 \times 10^{-5}$ .

high on all three metrics are expected to be good candidates for transfer. Thus, these area metrics may be used as an efficient method of sorting through the many potential manifold pairs available in the database. In this way, high-potential candidate pairs may be identified and transfers may be constructed.

For mission design, these transfer regions may also be interpreted as an initial step for the Poincaré section: the method introduced here essentially take two manifolds as input and returns a good region to look at as output. A Poincaré section may be taken somewhere in this region, for example, at the centroid. By coupling the two methods in this way, the disadvantages of the Poincaré section may be eliminated.



# CHAPTER 6

## *Extension: Characterization of the $\Delta v$ Surface*

---

Although useful as a preliminary metric, the transfer region polygon boundaries considered in Chapter 5 set very crude cuts on the transfer region and much information is lost in the process. Instead of considering a fixed tolerance cut-off, it may be more worthwhile to consider the  $\Delta v$  surface as a whole. In this manner, the expected smooth variation in the  $\Delta v$  of transfer may be obtained, and a more qualitative understanding of the potential transfer region may be developed. This chapter discusses the direction and potential of this future research.

Of particular interest to note is that this perspective of considering the  $\Delta v$  surface is not easily arrived at by considering the Poincaré section, but is a natural consequence of the transfer region polygon boundaries developed. Thus, in this sense, the qualitative understanding and characterization of the  $\Delta v$  surface described here is novel.

The ideas described here hold much potential for future research.

### 6.1 Introduction

It is useful to introduce the study of the  $\Delta v$  surface by beginning with an example. Figure 6.1 shows the intersection of the internal branch of the unstable  $EL_2$  manifold ( $J_{SE} = 3.000838525$ ) with the external branch of the stable  $LL_2$  manifold ( $J_{EM} = 3.039746895$ ). Rather than apply hard thresholds on the  $\Delta v$  of transfer at each spatial intersection, a contour plot may be considered. Figure 6.2 shows a contour plot computed from the  $\Delta v$  values at the interpolated spatial intersections.

Of particular interest are the jagged lines running from the bottom of the circular arc to the sides of the graph window. These lines are consequences of the implementation: in MATLAB, the contour plot routine `contour` requires `meshgrid` input, in which the function values must be specified at all points of some  $xy$ -matrix. Due to the concave geometry of the region of spatial intersection, it is necessary to incorrectly impose such a grid onto the data in order to generate this visualization. The result is this interpolation phenomenon which connects one portion of the arc to another. The region of interest (i.e., the arc) may be more easily visualized in relation to Figure 6.1 by considering Figure 6.3.

### 6.2 Manifold Layers

Another point of interest in Figure 6.3 is the lack of a continuous region of low-energy transfer. It is reasonable to expect that the  $\Delta v$  cost varies smoothly along some direc-

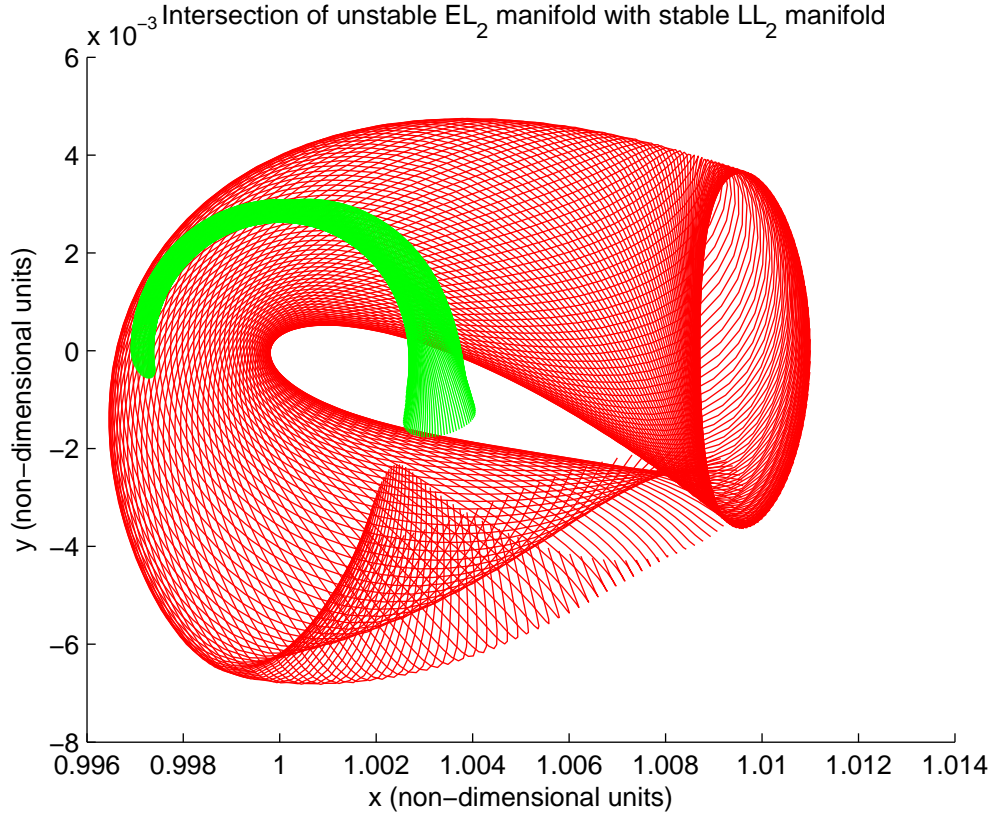


FIGURE 6.1. Intersection of the internal branch of the unstable  $EL_2$  manifold ( $J_{SE} = 3.000838525$ ) with the external branch of the stable  $LL_2$  manifold ( $J_{EM} = 3.039746895$ ) in the non-dimensionalized Sun-Earth rotating frame. Red, internal branch of unstable  $EL_2$  manifold; green, external branch of stable  $LL_2$  manifold.

tion in  $xy$ -space, so it is surprising that this is not demonstrated in the contour plot. Instead, interspersions of low-energy transfer are observed. Upon further investigation, it is readily seen that this is a direct consequence of the layering of the invariant manifolds.

Consider Figure 6.4, which is a zoomed-in version of Figure 6.3 about the area of interest. Careful inspection of the plot reveals that each manifold contains two layers in the sense that there are two families of trajectories crossing the same region of space (at different times). In particular, study of the trajectories comprising each manifold in Figure 6.4 reveals that there is a set of trajectories which cross with positive  $\dot{y}$  and also another which cross with negative  $\dot{y}$ . Thus, at any given point in space, there are two different  $\Delta v$  costs which may be considered. This is manifested in Figure 6.4 by the separation of low-energy transfer regions at the points where the family of trajectories with incompatible velocities cross. For a concrete example, consider any trajectory on

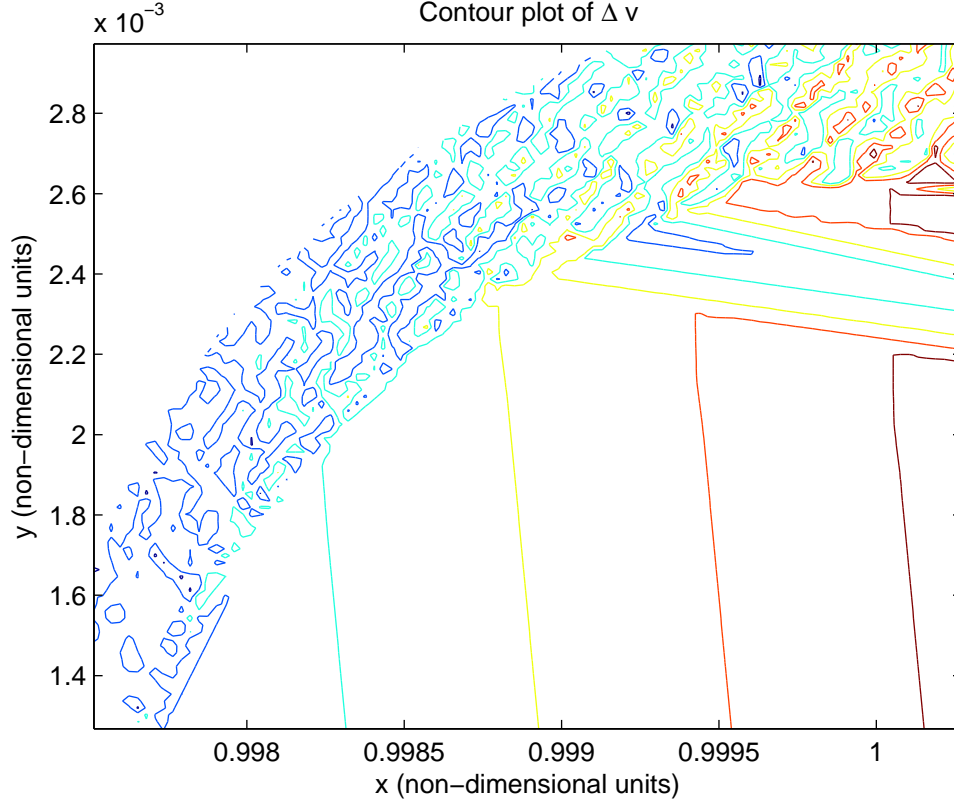


FIGURE 6.2. Contour plot of  $\Delta v$  for the manifolds considered in Figure 6.1. Dark colors (e.g., black, blue green) denote regions of low  $\Delta v$  transfer; light colors (e.g., red, orange, brown) denote regions of high  $\Delta v$  transfer. Only the curved arc is of interest here; the jagged lines connecting the bottom of the arc to the sides of the graph window are artifacts of the regular gridding required by the MATLAB function `contour`. Notice the lack of a continuous region of low-energy transfer.

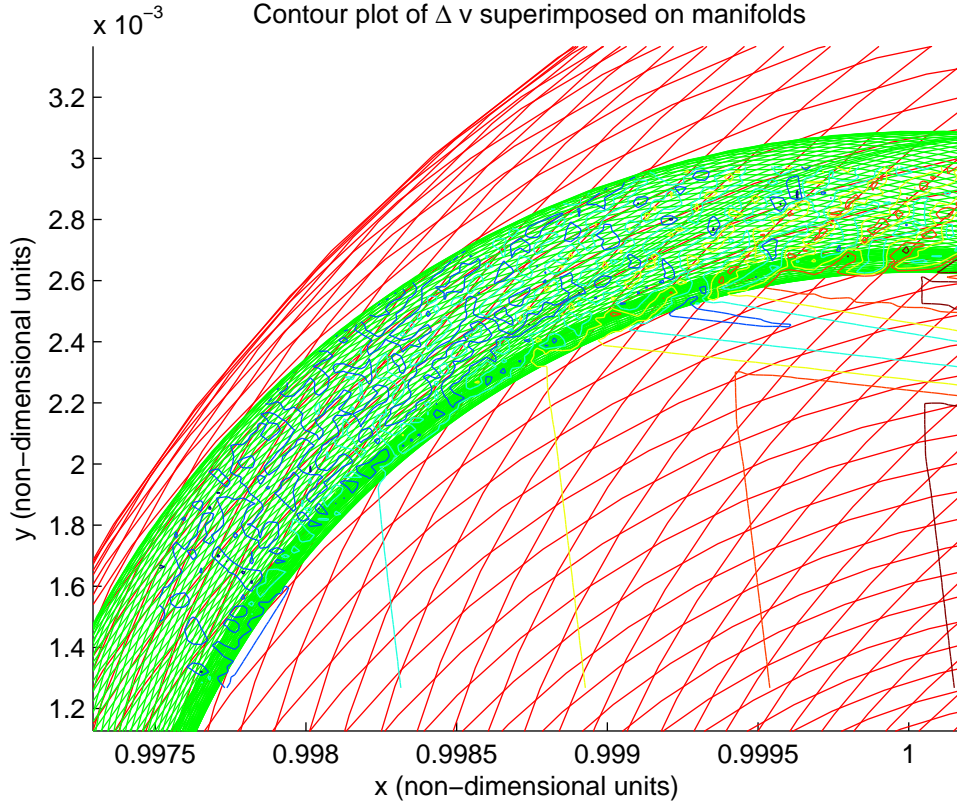


FIGURE 6.3. Contour plot of  $\Delta v$  in Figure 6.2 superimposed on the manifolds in Figure 6.1. Red, internal branch of unstable  $EL_2$  manifold; green, external branch of stable  $LL_2$  manifold. Dark colors (e.g., black, blue green) denote regions of low  $\Delta v$  transfer; light colors (e.g., red, orange, brown) denote regions of high  $\Delta v$  transfer.

the unstable manifold. As this trajectory is traversed, points of tangency with various trajectories on the stable manifold are encountered, but inevitably interspersed in between are intersections with trajectories belonging to the other family. High transfer costs are associated with these points. Linear interpolation then gives the image shown.

This leads directly to the problem of separating the two families of trajectories. By considering only one family at a time, it is reasonable to expect the smooth  $\Delta v$  transitions discussed earlier. This may potentially be implemented by statistical clustering applied directly to the velocity coordinates, or perhaps by considering the temporal coordinate in conjunction with the spatial ones. Neither of these possibilities have yet been explored.

This discussion also motivates a more general question concerning the character of the manifolds considered. Prior to this investigation of the  $\Delta v$  surface, we had not even noticed the layering behavior exhibited. Perhaps these layers may be exploited for our

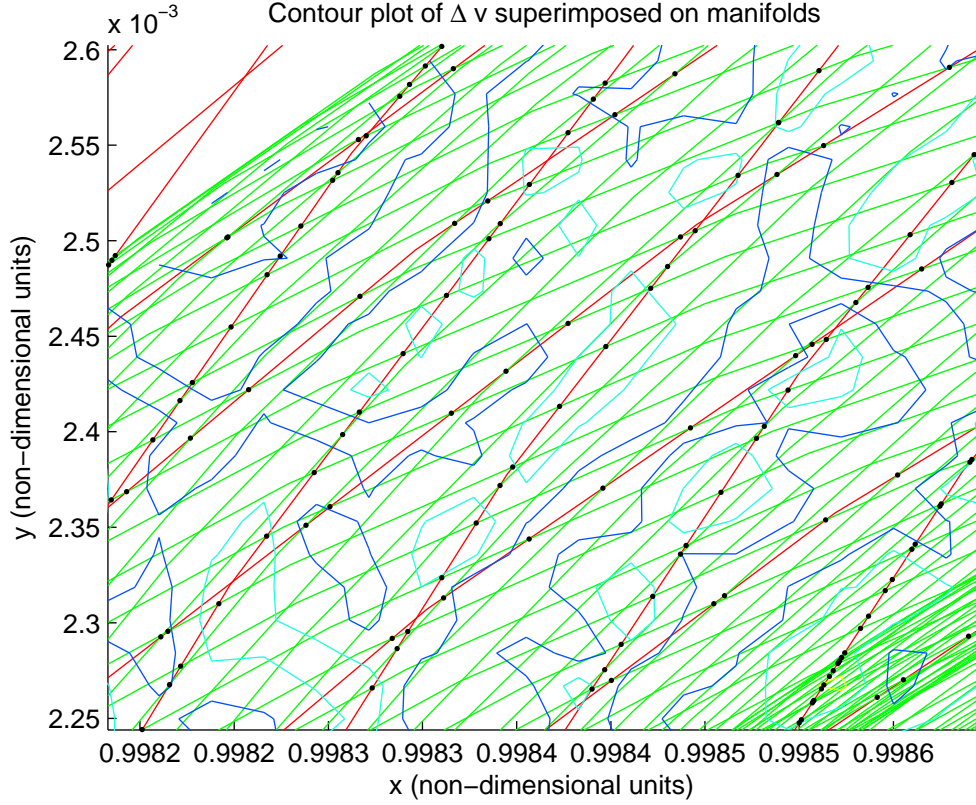


FIGURE 6.4. Zoomed-in version of Figure 6.3. Red, internal branch of unstable  $EL_2$  manifold; green, external branch of stable  $LL_2$  manifold. Dark colors (e.g., black, blue green) denote regions of low  $\Delta v$  transfer; light colors (e.g., red, orange, brown) denote regions of high  $\Delta v$  transfer. Black dots, spatial intersections. Notice the layering behavior in each manifold: for a given region of space, two families of trajectories with qualitatively different behavior (velocities) are defined. This results in the spatial pairing of low-energy transfer points with high-energy transfer points, hence any continuous region of low-energy transfer is necessarily broken up under this implementation.

purpose. In some sense, this layering property has already been used in [15] to target the Earth by exploiting the sensitivity of the twisting character of the manifold; this twisting is directly related to the layering observed.

### 6.3 Parametric Study of the Transfer Region

Once separation of the manifold layers has been achieved, the relevant low-energy transfer region may be observed independently of all other considerations, and a qualitative understanding of the transfers available may be attained. In particular, it may be worthwhile to use this information to investigate the geometry of the transfer region.

Issues of robustness may also play a part. For example, due to inaccuracies of model approximation, it may be advantageous to consider transfers with the highest tolerances to error. This may be defined in a variety of ways, for instance, by considering the transfer region energy trough with the lowest sensitivity to perturbation, either in position or velocity space, or both.

Furthermore, this geometry may be investigated as the parameters of the problem are varied. In this project, for example, features of the transfer region may be considered as a function of the Jacobi constants of each PCR3BP and the phase of the Moon. Thus, a parametric study of the transfer region may be conducted.

### 6.4 Potential for Future Research

It is possible that the research directions outlined in this chapter may be refined to propose another suitable independent research project with the ultimate goal of characterizing the  $\Delta v$  surfaces of manifold transfer. It is difficult to say for certain how fruitful this research will be, but it does seem fundamental to the mission design problem considered. Perhaps by studying the transfer region in such a general manner, alternative trajectory solutions may be inspired.

Moreover, the ideas described may be extended to the three-dimensional case since the dimensional constraint provided by the Jacobi constant is not explicitly used. This constraint is what gives the Poincaré section such applicability in the planar case considered in this project; on the other hand, it also makes the Poincaré section difficult to apply in full three-space. The treatment of  $\Delta v$ , however, may apply more generally.

We conclude this chapter with the restatement that the directions discussed here are consequences of the perspective adopted by considering the transfer region boundary method that we have developed. Although this method was developed heuristically without regard to addressing the broad question presented here, the potential of its implications already shows.

# CHAPTER 7

## Trajectory Correction Using Four-Body Dynamics

---

Trajectories computed in the coupled three-body regime with appropriate parameter restrictions do provide fair approximations to solutions to the more realistic four-body model. However, in order to get more quantitatively correct trajectories for actual missions from the Earth to the Moon, the approximate trajectories need to be corrected in successively more complicated models. As a first step, approximate trajectories will be corrected in the Sun-Earth-Moon four-body problem using the bicircular approximation. In this chapter, equations of motion for this regime are stated and derived and a formulation of the multiple shooting algorithm as an optimization problem is presented so that approximate trajectories can be numerically corrected in more and more complicated regimes, such as the bicircular model.

### 7.1 The Bicircular Model

The bicircular model may be obtained from the PCR3BP by renaming  $m_3$  as  $m_4$  and putting masses  $m_2$  and  $m_3$  into circular orbits their barycenter. Figure 7.1 provides a schematic diagram, viewed from the Sun-Earth rotating frame and non-dimensionalized with respect to the Sun-Earth system. Now masses  $m_1$ ,  $m_2$  and  $m_3$  are considered to be the “primaries,” influencing but not being influenced by the motion of  $m_4$ .

From the derivation of the equations of motion in the PCR3BP in Appendix C, the equations of motion for the bicircular model are a simple extension. Let  $r_1$ ,  $r_2$ , and  $r_3$  be the distances from  $m_4$  to masses  $m_1$ ,  $m_2$ , and  $m_3$ , respectively. From Figure 7.1, it can be seen that

$$\begin{cases} r_1^2 = [x + \mu]^2 + y^2, \\ r_2^2 = [x - (1 - \mu - \nu R \cos(nt + \theta_0))]^2 + [y + \nu R \sin(nt + \theta_0)]^2, \\ r_3^2 = [x - (1 - \mu + (1 - \nu) R \cos(nt + \theta_0))]^2 + [y - (1 - \nu) R \sin(nt + \theta_0)]^2, \end{cases} \quad (7.1)$$

where  $\mu$  is the mass ratio of the Sun-Earth system,  $\nu$  is the mass ratio of the Earth-Moon system,  $R$  is the Earth-Moon separation distance, and  $n$  is the Earth-Moon system’s relative angular velocity, non-dimensionalized with respect to the Sun-Earth frame. Form the Lagrangian  $L$  as kinetic minus potential energy and take derivatives according to the Euler-Lagrange equations to obtain the equations of motion

$$\begin{cases} \ddot{x} - 2\dot{y} = x - U_x, \\ \ddot{y} + 2\dot{x} = y - U_y, \end{cases} \quad (7.2)$$

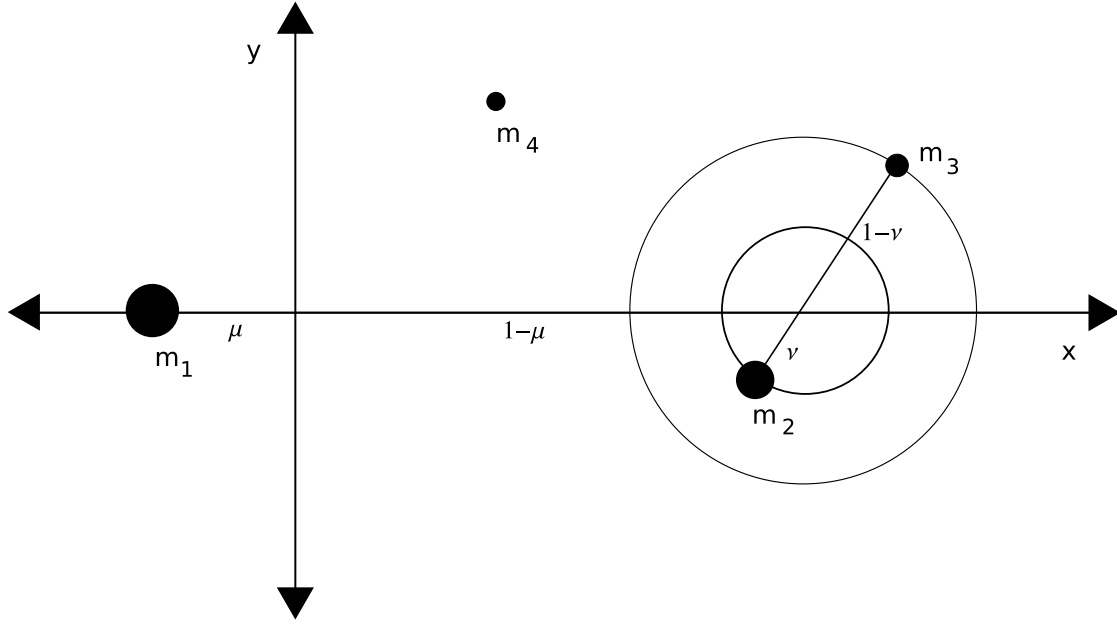


FIGURE 7.1. Schematic diagram of the bicircular model in the non-dimensionalized Sun-Earth frame

where subscripts denote partial derivatives and

$$U \equiv -\frac{\mu_1}{r_1} - \frac{\mu_2}{r_2} - \frac{\mu_3}{r_3},$$

where

$$\mu_1 \equiv \frac{m_1}{m_1 + m_2}, \quad \mu_2 \equiv \frac{m_2}{m_1 + m_2}, \quad \mu_3 \equiv \frac{m_3}{m_1 + m_2}.$$

In the traditional bicircular model, the Earth travels in a circular orbit around the Sun, and the Moon travels in circular orbit around the Earth. The above model differs slightly from the traditional bicircular model, since the barycenter of the Earth-Moon system travels in circular orbit about the barycenter of the Sun-Earth system. To obtain the traditional bicircular model, set  $\mu = \nu = 0$  in (7.1).

## 7.2 Coupling the Three-Body Trajectories

Methods outlined in the previous chapters are used to create a trajectory from low Earth orbit to lunar orbit in three steps. First, the minimum  $\Delta v$  trajectory traveling from low Earth orbit to the  $EL_2$  Lyapunov orbit along a stable manifold is computed, as shown in Figure 7.2. Next, the minimum  $\Delta v$  trajectory traveling from the  $LL_2$  Lyapunov orbit to Lunar orbit is computed, as shown on the left in Figure 7.3. Finally, the trajectory connecting the internal branch of the  $EL_2$  unstable manifold to the external branch



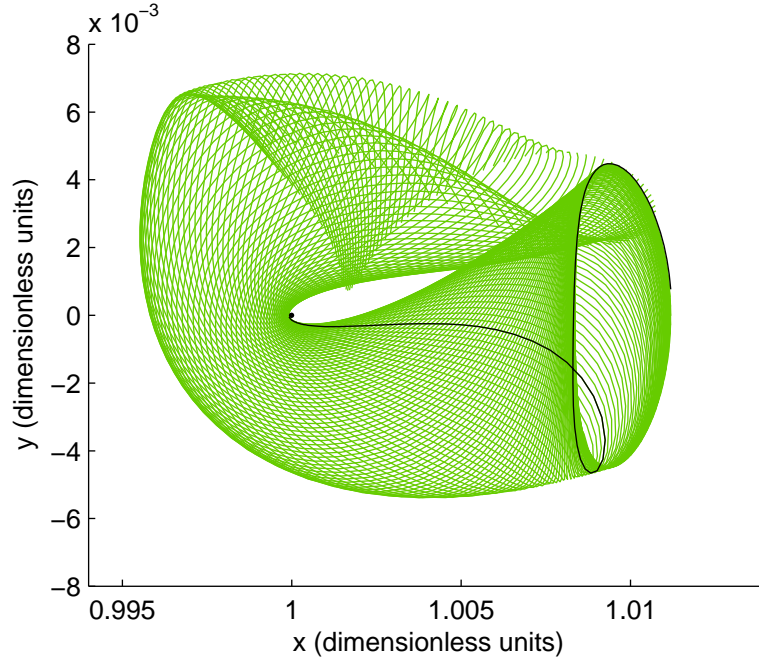


FIGURE 7.2. A trajectory with minimum  $\Delta v$  connecting low Earth orbit to the  $EL_2$  Lyapunov orbit using the internal branch of the  $EL_2$  stable manifold. Sun-Earth rotating frame.

of the  $LL_2$  stable manifold requiring the minimum  $\Delta v$  is found. The first part of this trajectory, viewed from the Sun-Earth rotating frame, is shown in Figure 7.4. The second part of the trajectory, viewed from the Earth-Moon rotating frame, can be seen on the right side Figure 7.3.

The phase of the moon at the time of manifold transfer is manually adjusted until the manifold transfer occurred sufficiently far from  $LL_2$  Lyapunov orbit to represent a good point of transition from the Sun-Earth PCR3BP to the Earth-Moon PCR3BP. The resulting linked PCR3BP trajectory is shown in the Sun-Earth non-dimensional rotating frame in Figure 7.5. Note that part of the  $EL_2$  Lyapunov orbit was used to link the low Earth orbit trajectory to the transfer trajectory. The corresponding link in the Earth-Moon system was not attempted, leaving the task of finding a continuous trajectory to the correction scheme described next.

### 7.3 Multiple Shooting as an Optimization Problem

Such correction schemes have usually implemented multiple shooting methods. In a typical multiple shooting scheme, points along the initial guess trajectory are sampled and integrated forward for a specified length of time. The endpoints of the propagated

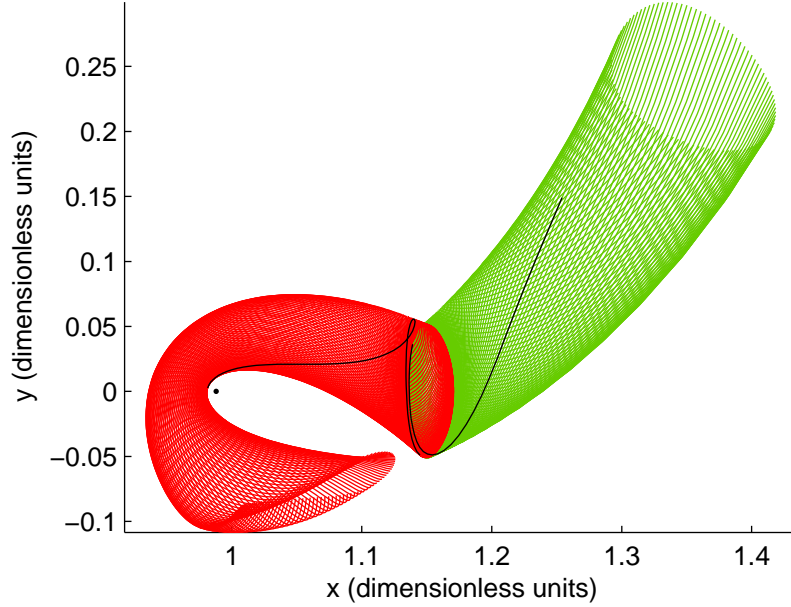


FIGURE 7.3. On the left, the trajectory with minimum  $\Delta v$  connecting the  $LL_2$  Lyapunov orbit to lunar orbit using the internal branch of the  $LL_2$  unstable manifold. On the right, the minimum  $\Delta v$  trajectory connecting the external branch of the  $LL_2$  stable manifold to the internal branch of the  $EL_2$  unstable manifold. Earth-Moon rotating frame.

trajectories are then compared with the initial guess and shooting algorithms are used to correct the initial guess subject to prescribed boundary and matching conditions. Figure 7.6 shows how points sampled from the initial guess in the coupled three-body regime diverge from the initial trajectory when integrated in the bicircular model.

The multiple shooting method may be cast as an optimization problem as follows. Construct a merit function  $f$ , whose arguments are the entire set of points sampled from the initial guess:

$$f = f(t_1, x_1, y_1, \dot{x}_1, \dot{y}_1, \dots, t_n, x_n, y_n, \dot{x}_n, \dot{y}_n).$$

To compute the value of  $f$ , propagate each initial condition  $\{t_i, x_i, y_i, \dot{x}_i, \dot{y}_i\}$  in the set of arguments of  $f$  forward to time  $t_{i+1}$ . Let the endpoint of this trajectory be  $\{t_{i+1}, \bar{x}_{i+1}, \bar{y}_{i+1}, \bar{\dot{x}}_{i+1}, \bar{\dot{y}}_{i+1}\}$ . Then correction is attained by minimization of the merit

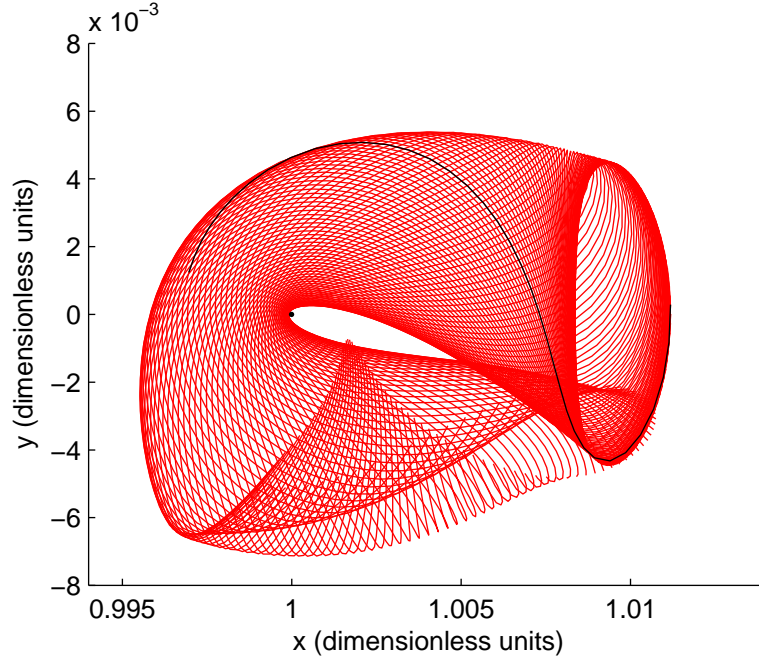


FIGURE 7.4. A trajectory with minimum  $\Delta v$  connecting the  $EL_2$  Lyapunov orbit to the  $LL_2$  Lyapunov orbit using the intersection of the internal branch of the unstable  $EL_2$  manifold and the external branch of the stable  $LL_2$  manifold. Sun-Earth rotating frame.

function

$$f(t_1, x_1, y_1, \dot{x}_1, \dot{y}_1, \dots, t_n, x_n, y_n, \dot{x}_n, \dot{y}_n) = w_x \sum_{i=2}^n [(\bar{x}_i - x_i)^2 + (\bar{y}_i - y_i)^2] \\ + w_v \sum_{i=2}^n [(\dot{\bar{x}}_i - \dot{x}_i)^2 + (\dot{\bar{y}}_i - \dot{y}_i)^2],$$

where  $w_x$  and  $w_v$  are positive weighting factors for position and velocity, respectively.

The merit function described above could be used in conjunction with numerical optimization routines to find a continuous trajectory in the bicircular model, using the coupled PCR3BP trajectory as an initial guess. This allows the application of the extensive work done with numerical optimization methods to the problem of multiple shooting. However, optimization schemes can perform poorly if the merit function  $f$  is poorly conditioned numerically. Due to the limited time available for research this summer, little work was done in order to ensure that  $f$  is numerically well conditioned. In fact, preliminary investigations indicate that this is not the case. This may be because  $f$  is poorly scaled. When plotted in the non-dimensional Sun-Earth rotating frame, trajectories from the Earth to the Moon vary on the order of  $1 \pm 10^{-2}$  in the  $x$ -coordinate,

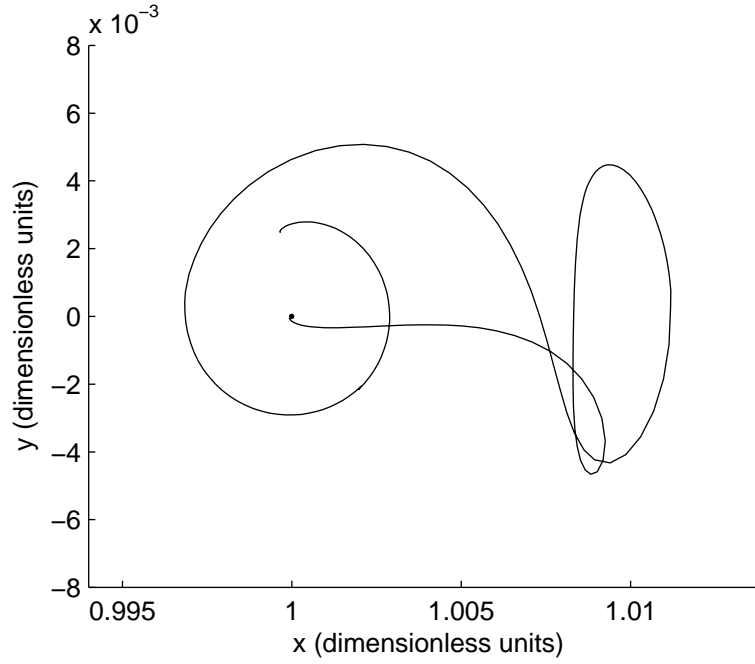


FIGURE 7.5. Coupled PCR3BP initial guess for a trajectory from low Earth orbit to lunar orbit, viewed from the Sun-Earth rotating frame.

for example. In order to keep the optimized solution close to the initial guess, points are sampled so that corrections are on the order of  $10^{-6}$  for each iteration. In other words, while  $x \in (0.98, 1.01)$ , the important corrections to the  $x$ -coordinate occur in the sixth decimal place. This makes the computation of numerical derivatives difficult and leads to optimization algorithms performing poorly. One possible remedy is to scale the problem so that the variation in  $x$  occurs in the first significant figure. However, this was not attempted due to time constraints.

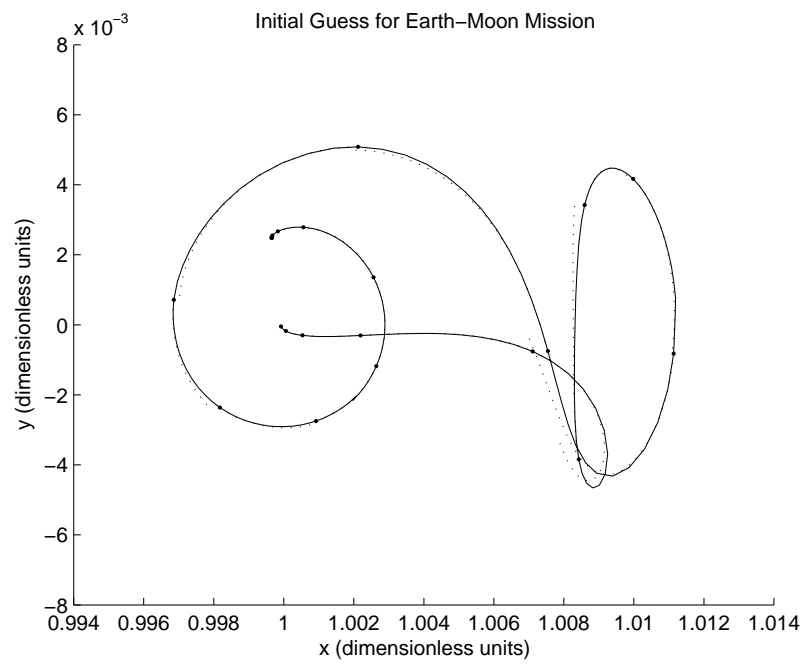


FIGURE 7.6. Coupled PCR3BP initial guess (solid curve) and corresponding bicircular trajectories (dashed curves) with initial conditions sampled from the initial guess. Sun-Earth rotating frame



# CHAPTER 8

## Conclusion

---

This project focused on producing a method for designing impulsive low-energy transfers between the Earth and the Moon using the invariant manifolds of the PCR3BP. This trajectory was then used as an initial guess for a final trajectory in the four-body problem, which was corrected to a possible transfer using the bicircular model. The method presented here for designing such trajectories is more systematic than previous methods in that searches through the parameter space explored via a manifold database were implemented to minimize the  $\Delta v$  required. Using such a database decreased the computational overhead, and the related MATLAB toolbox developed allowed for more informed decisions as to where to look for these transfers.

Presented here are results showing the promise that continuation methods hold in computing larger families of Lyapunov orbits. The method proposed here uses this new approach and is able to compute, using the larger Lyapunov orbits achieved, a high number of manifolds which intersect with the desired circular orbits, providing greater scope for possible transfers.

There are ideas here on parameter space restrictions that need to be considered when designing such trajectories, and outlined is an innovative approach for finding the bounds on manifold propagation. This was useful for this project in determining the restrictions on the manifolds stored in the final database, but it has many possible extensions, including, for example, incorporation of the dependency on the mass ratio of the system.

The presented mission design method, breaks the trajectory up into three separate parts: low Earth orbit to  $EL_2$  manifold, intersection of  $EL_2$  and  $LL_2$  manifolds, and  $LL_2$  manifold to lunar orbit. This approach leads to specifications of Jacobi constants for each system, by requiring the  $\Delta v$  at intersection of manifold and orbit to be minimal, immediately providing suggestions of specific trajectories for use in the final transfer. These guided the choices in the final proposed trajectory.

The method also presents a new way of considering manifold intersections. Previously, manifold intersections were mainly studied using Poincare sections, but that methods dependence on the position of a cut in the manifold led to research into a more intuitive way of studying these intersections. This method provides a visual idea of where a transfer with a low  $\Delta v$  will occur in relation to the intersecting manifolds themselves and suggests the possibility for mapping the entire  $\Delta v$  surface. The area of manifold intersection considerations opens up a huge area for future research. In order for the initial idea presented here to become a fully useful tool, a consideration of manifold

layers would need to be done and a more representational way of showing these low energy transfer areas would need to be found, possibly by using contour plots.

The final section of this report deals with the problems involved in correcting a proposed coupled three-body trajectory in the fully integrated four-body problem. A correction method is proposed that formulates the problem as one of optimization, and although this works well for simple cases such as closing Lyapunov orbits, here would be an ideal area for continued future research.

This project highlights many other possible areas for future research. Only considered here was the Lagrange point  $L_2$  and so one possible extension would be to apply the exact same method outlined here to  $L_1$ . The PCR3BP assumptions could be challenged too, by taking elliptical orbits instead of circular ones and by making an allowance for the relative orbital inclinations of the Sun-Earth and Earth-Moon systems. Also the design of the final trajectory leaves open endless opportunities for investigation. The method here takes in a section around the Lyapunov orbit of  $L_2$  (in the Sun-Earth system) that takes upward of 6 months to traverse. Taking out this section and considering manifold transfer before the convergence onto the orbit would cut significant time off the length of the transfer, but may increase the overall  $\Delta v$ . Moreover the final trajectory could be made more realistic by integrating it with JPL ephemeris data. Taking into account other options such as retrograde orbits and slingshot trajectories, as well as the extension to the three-dimensional model, there are many areas that could be investigated.

In conclusion, this report lays out the basic stages for the logical design of a low-energy trajectory from the Earth to the Moon using the invariant manifolds of the PCR3BP. Results, detailed earlier, show that this method of transfer, although more time consuming, is expected to be significantly more efficient than the conventional Hohmann transfer and imply that the dynamical properties that the final trajectory successfully utilizes merit much further exploration.



# APPENDIX A

## *Restricted Two-Body Problem Dynamics*

---

In this appendix, the equations of motion for the restricted two-body problem are stated and their solutions discussed. In this context, by restricted we mean that the influence of the smaller mass upon the larger is ignored. Similar treatments of this topic can be found in [16], for example.

### A.1 Equations of Motion

The equations of motion for the restricted two-body problem are given by Newton's equation:

$$\ddot{\mathbf{r}} = -\frac{Gm}{r^3}\mathbf{r},$$

where  $m$  is the mass of the larger body, here the Earth or the Moon,  $G$  is the gravitational constant, and  $\mathbf{r}$  is the vector pointing from the larger body to the smaller body (the Earth to the spacecraft, or the Moon to the spacecraft). These equations can be alternatively cast as

$$\ddot{\mathbf{r}} = -\frac{\mu}{r^3}\mathbf{r} \tag{A.1}$$

where  $\mu \equiv Gm$  is the gravitational constant of the larger body.

### A.2 Planar Motion

Taking the cross product of (A.1) with  $\mathbf{r}$ , we can find an equation for the angular momentum  $\mathbf{h}$  per unit mass:

$$\mathbf{r} \times \ddot{\mathbf{r}} = -\mathbf{r} \times \frac{\mu}{r^3}\mathbf{r} = 0.$$

Consider:

$$\frac{d}{dt}(\mathbf{r} \times \dot{\mathbf{r}}) = \dot{\mathbf{r}} \times \dot{\mathbf{r}} + \mathbf{r} \times \ddot{\mathbf{r}}$$

The second term on the right hand side is zero and so therefore

$$\mathbf{r} \times \ddot{\mathbf{r}} = \frac{d}{dt}(\mathbf{r} \times \dot{\mathbf{r}}) = 0$$

$$\implies \mathbf{r} \times \ddot{\mathbf{r}} = \mathbf{r} \times \mathbf{v} = \text{constant} = \mathbf{h} \quad (\text{A.2})$$

$\mathbf{v}$  is the angular momentum and so, as  $\mathbf{h}$  is constant and perpendicular to both  $\mathbf{v}$  and  $\mathbf{r}$ , the motion of the two bodies is confined to the plane. This planar motion gives us three constants of motion.

### A.3 Energy

Taking the dot product of equations (A.1) with the velocity  $\mathbf{v} = \dot{\mathbf{r}}$ , an equation for the energy can be derived:

$$\dot{\mathbf{r}} \cdot \ddot{\mathbf{r}} = -\frac{\mu}{r^3} \dot{\mathbf{r}} \cdot \mathbf{r}$$

$$\mathbf{v} \cdot \dot{\mathbf{v}} = v \cdot \dot{v} = -\frac{\mu}{r^2} \dot{r}$$

$$\frac{d}{dt} \left( \frac{1}{2} v^2 \right) = \frac{d}{dt} \left( \frac{1}{r} \mu \right)$$

$$E = \frac{1}{2} v^2 - \frac{\mu}{r} + C \quad (\text{A.3})$$

This  $E$ , energy value, is constant along the trajectories and is the sum of the kinetic and potential energies with  $C$  a constant. The constant value,  $C$ , is usually zero. This equation can then be rearranged to one for velocity:

$$v = \sqrt{2 \left( E + \frac{\mu}{r} \right)} \quad (\text{A.4})$$

For a circular orbit the energy value is zero, and so, due to elliptical orbit considerations, the velocity required for the smaller mass to remain in a circular orbit around the larger one is:

$$v = \sqrt{\frac{\mu}{r}} \quad (\text{A.5})$$

### A.4 Properties of an Ellipse

Using the  $\mathbf{h}$  value calculated earlier take the cross product of this with equations (A.1) :

$$\ddot{\mathbf{r}} \times \mathbf{h} = -\frac{\mu}{r^3}(\mathbf{r} \times \mathbf{h})$$

Consider the derivative

$$\frac{d}{dt}(\mathbf{v} \times \mathbf{h}) = \dot{\mathbf{v}} \times \mathbf{h} + \mathbf{v} \times \dot{\mathbf{h}} = \dot{\mathbf{v}} \times \mathbf{h} = \ddot{\mathbf{r}} \times \mathbf{h}$$

as  $\dot{\mathbf{h}} = 0$  due to  $\mathbf{h}$  being constant. Also there is

$$\mathbf{r} \times \mathbf{h} = \mathbf{r} \times (\mathbf{r} \times \mathbf{v}) = (\mathbf{r} \cdot \mathbf{v})\mathbf{r} - (\mathbf{r} \cdot \mathbf{r})\mathbf{v} = r\dot{r}\mathbf{r} - r^2\mathbf{v}$$

So, combining the above:

$$\ddot{\mathbf{r}} \times \mathbf{h} = -\frac{\mu}{r^3}(\mathbf{r} \times \mathbf{h}) = -\frac{\mu}{r^2}(\dot{r}\mathbf{r} - r\mathbf{v}) = \frac{d}{dt}\left(\frac{\mu\mathbf{r}}{r}\right)$$

Define  $\hat{\mathbf{r}} = \frac{\mathbf{r}}{r}$ , the unit vector.

$$\frac{d}{dt}(\mathbf{v} \times \mathbf{h}) = \frac{d}{dt}(\mu\hat{\mathbf{r}})$$

$$\implies \mathbf{v} \times \mathbf{h} - \mu\hat{\mathbf{r}} = C$$

By convention we take  $C = \mu\mathbf{e}$  where  $\mathbf{e}$  is the eccentricity vector. Then take the dot product of this with  $\mathbf{r}$  to give:

$$\mathbf{r}(\mathbf{v} \times \mathbf{h} - \mu\hat{\mathbf{r}}) = \mu\mathbf{er}$$

$\mathbf{re} = r\cos(\gamma)$  where  $\gamma$  is the angle from the eccentricity to the edge of the orbit radius  $r$ .

$$h^2 - \mu r = \mu r \cos(\gamma)$$

$$\frac{h^2}{\mu} = r(1 + \cos(\gamma))$$

So we can get the equation of a conic in polar co-ordinates:

$$r = \frac{\frac{h^2}{\mu}}{(1 + e \cos(\gamma))}$$

which simplifies to

$$r = \frac{P}{(1 + e \cos(\gamma))}$$

where  $P = \frac{h^2}{\mu}$

From the properties of an ellipse, with  $r_p$  being the pericentre at distance  $a$  from the origin,  $r_a$  being the apocentre, and  $e$  the location of the eccentricity:

$$r_p = a(1 - e)$$

$$r_a = a(1 + e)$$

$$P = \frac{h^2}{\mu} = a(1 - e^2)$$

The energy ((A.3)) at the pericentre is therefore

$$E = \frac{1}{2}v_p^2 - \frac{\mu}{r_p} = -\frac{\mu}{2a}$$

This can be rearranged to give an equation for the semi-major axis,  $a$ , of the ellipse in which the smaller body moves, in the frame of reference with the other body at the origin:

$$a = -\frac{\mu}{2E} \tag{A.6}$$

Also having this equation for  $E$  allows us to rearrange (A.4) to

$$v = \sqrt{2\mu \left( \frac{1}{r} - \frac{1}{2a} \right)} \tag{A.7}$$

The period,  $T$ , can be calculated also using the formula

$$T = 2\pi \sqrt{\frac{a^3}{\mu}} \tag{A.8}$$

# APPENDIX B

## Table of Parameter Values

---

This appendix provides tables of the parameter values used in this project.

The parameter values used for the Sun-Earth ( $\mu \equiv 3 \times 10^{-6}$ ) and Earth-Moon ( $\mu \equiv 0.012$ ) systems are given in Tables B.1 and B.2, respectively. Note that the angular velocity of the Earth-Moon frame given is relative to the angular velocity of the Sun-Earth frame.

Parameter	SI units	Normalized Units
Mean Earth-Sun distance	$1.496 \times 10^8$ km	1
Mass of Sun	$1.9889 \times 10^{30}$ kg	$1 - \mu = 0.999996$
Mass of Earth	$5.9742 \times 10^{24}$ kg	$\mu = 3 \times 10^{-6}$
Angular velocity of Sun-Earth frame	$1.991 \times 10^{-7}$ s <sup>-1</sup>	1

TABLE B.1. Table of parameter values for the Sun-Earth system.

Parameter	SI units	Normalized Units
Mean Earth-Moon distance	$3.844 \times 10^5$ km	1
Mass of Earth	$5.9742 \times 10^{24}$ kg	$1 - \mu = 0.988$
Mass of Moon	$7.3483 \times 10^{22}$ kg	$\mu = 0.012$
Angular velocity of Earth-Moon frame	$2.680 \times 10^{-6}$ s <sup>-1</sup>	1

TABLE B.2. Table of parameter values for the Earth-Moon system.

# APPENDIX C

## Derivation of the Equations of Motion for the Planar Circular Restricted Three-Body Problem

---

The equations of motion for the PCR3BP are derived here in both inertial (sidereal) and rotating (synodic) coordinate systems, using both dimensional and dimensionless quantities. In addition, the Jacobi integral and the Jacobi constant are derived and explained. The development given here follows [20] with minor modifications.

The PCR3BP is given as follows: Two masses  $m_1$  and  $m_2$  ( $m_1 > m_2$ ) travel in circular orbits with constant angular velocity  $n$  about their barycenter, separated by a constant distance  $l$ . A third mass  $m_3$  moves under the gravitational influence of the first two, but does not affect their motion. Equations of motion are given in an inertial coordinate system originating at the barycenter of masses  $m_1$  and  $m_2$  or in a rotating coordinate system such that  $m_1$  and  $m_2$  appear to be fixed. The equations of motion are given in terms of  $r_1$  and  $r_2$ , the distance from  $m_3$  to masses  $m_1$  and  $m_2$ , respectively. In addition, define  $\mu \equiv m_2/(m_1 + m_2)$  to be the mass ratio of the system.

The equations of motion will be derived using the Euler-Lagrange equations

$$\frac{d}{dt} \frac{\partial L}{\partial \dot{q}_i} - \frac{\partial L}{\partial q_i} = 0,$$

where  $q_i$  are the generalized coordinates and  $L$  is the Lagrangian, equal to kinetic minus potential energy. In order to simplify these equations, The PCR3BP is non-dimensionalized as follows

$$\begin{aligned} \text{distance } d &\rightarrow d/l \\ \text{time } t &\rightarrow nt \\ \text{mass } m &\rightarrow m/(m_1 + m_2). \end{aligned}$$

Also, rather than introduce new variables for each coordinate system and dimensionality, variable names will be used over in the following sections. Accordingly, variable names will only be consistent for the local section.

### C.1 Inertial (Sidereal) Coordinates

Examining Figure C.1, it can be seen that

$$\begin{aligned} r_1^2 &= (x + \mu \cos nt)^2 + (y + \mu \sin nt)^2 \\ r_2^2 &= (x - (1 - \mu) \cos nt)^2 + (y - (1 - \mu) \sin nt)^2. \end{aligned} \tag{C.1}$$

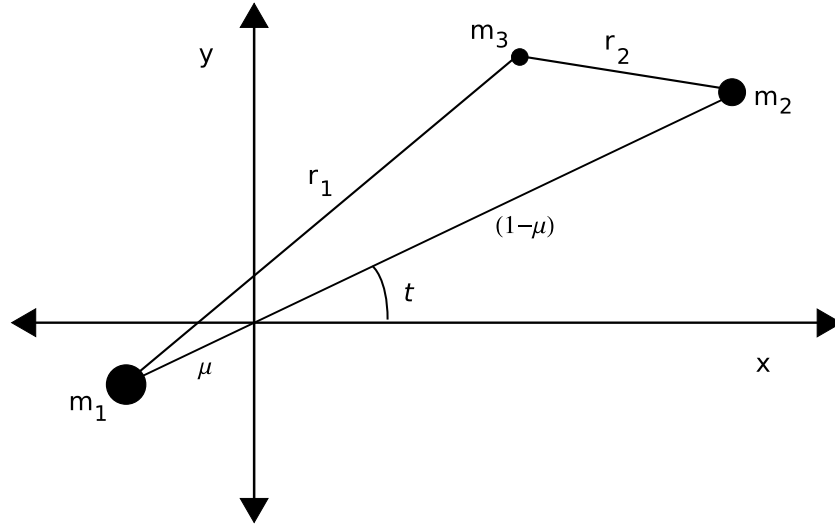


FIGURE C.1. Schematic diagram of the PCR3BP in the inertial frame.

Forming the Lagrangian, one obtains

$$L = \frac{1}{2}(\dot{x}^2 + \dot{y}^2) - U(x, y, t), \quad (\text{C.2})$$

where

$$U(x, y, t) = -\frac{1-\mu}{r_1} - \frac{\mu}{r_2} - \frac{1}{2}\mu(1-\mu)$$

is an explicit function of time. The constant term in  $U$  is there by convention and does not affect the potential.

Differentiating (C.2) according to the Euler-Lagrange equations, one obtains the equations of motion in the inertial frame:

$$\begin{aligned} \ddot{x} &= -U_x \\ \ddot{y} &= -U_y, \end{aligned} \quad (\text{C.3})$$

where subscripts denote partial derivatives. As seen above, these equations of motion are time-dependent, making analysis difficult.

## C.2 Rotating (Synodic) Coordinates

In the rotating coordinate system, distances  $r_1$  and  $r_2$  become (see Figure C.2)

$$\begin{aligned} r_1^2 &= (x + \mu)^2 + y^2 \\ r_2^2 &= (x - (1 - \mu))^2 + y^2. \end{aligned} \quad (\text{C.4})$$

Using the coordinate transformations in Appendix D, the Lagrangian in the rotating frame becomes



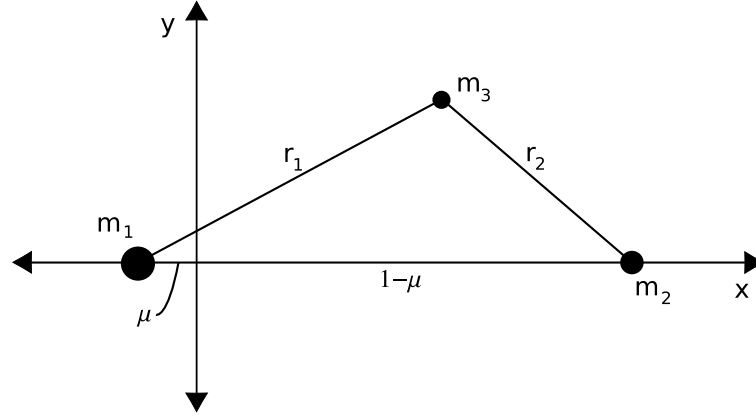


FIGURE C.2. Schematic diagram of the PCR3BP in the rotating frame.

$$L = \frac{1}{2}((\dot{x} - y)^2 + (\dot{y} + x)^2) - U(x, y), \quad (\text{C.5})$$

where

$$U(x, y) = -\frac{1-\mu}{r_1} - \frac{\mu}{r_2} - \frac{1}{2}\mu(1-\mu)$$

is no longer an explicit function of time. Differentiating (C.5) according to the Euler-Lagrange equations, one obtains, after simplification, the equations of motion

$$\begin{aligned} \ddot{x} - 2\dot{y} &= -\bar{U}_x \\ \ddot{y} + 2\dot{x} &= -\bar{U}_y, \end{aligned} \quad (\text{C.6})$$

where

$$\bar{U} = -\frac{1}{2}((1-\mu)r_1^2 + \mu r_2^2) - \frac{1-\mu}{r_1} - \frac{\mu}{r_2}$$

is the effective potential.

### C.3 The Jacobi Constant

The time-independent equations of motion (C.6) admit one integral of motion, or energy integral, called the Jacobi integral. To derive this from the equations of motion, note that

$$\begin{aligned} \frac{d}{dt}(\dot{x}^2 + \dot{y}^2) &= 2(\dot{x}\ddot{x} + \dot{y}\ddot{y}) \\ &= 2[\dot{x}(2\dot{y} - \bar{U}_x) + \dot{y}(-2\dot{x} - \bar{U}_y)] \\ &= -2(\bar{U}_x\dot{x} + \bar{U}_y\dot{y}) = -2\frac{d}{dt}(\bar{U}) \end{aligned}$$

and define

$$J \equiv -(\dot{x}^2 + \dot{y}^2) - 2\bar{U} \quad (\text{C.7})$$

so that

$$\frac{d}{dt}J = 0.$$

Therefore, the quantity  $J$  is conserved for any trajectory in the PCR3BP.

# APPENDIX D

## Invariant Manifold Computation

---

In this appendix, methods used for computing the invariant manifolds in the PCR3BP are outlined. The method may be broken down into the following steps: determining the locations of the Lagrange points, linearizing the equations of motion around these points, finding Lyapunov orbits about these points, computing the monodromy matrix, and perturbing from the Lyapunov orbit and propagating either forwards or backwards in time to generate the manifolds. For more information regarding the location of the Lagrange points and linearization of the equations of motion, see [13]. The details relating to Lyapunov orbits and the monodromy matrix can be found in [9].

### D.1 Lagrange Points

Consider the equations of motion for the PCR3BP (with masses  $m_1$  and  $m_2$ ) in the non-dimensionalized rotating frame:

$$\begin{cases} \ddot{x} - 2\dot{y} = \Omega_x, \\ \ddot{y} + 2\dot{x} = \Omega_y, \end{cases} \quad (\text{D.1})$$

where dot notation denotes differentiation with respect to time and subscripts denote partial differentiation, and

$$\Omega \equiv \frac{1}{2} (x^2 + y^2) + \frac{1-\mu}{r_1} + \frac{\mu}{r_2} + \frac{1}{2} (\mu - 1) \mu,$$

where  $r_1$  and  $r_2$  are the distances from the third body to  $m_1$  and  $m_2$ , respectively. The Lagrange points are equilibrium solutions to this system, which necessarily requires  $\dot{x} = \ddot{x} = \dot{y} = \ddot{y} = 0$ , hence the equilibrium system

$$\begin{cases} \Omega_x = x - \frac{(1-\mu)(x+\mu)}{r_1^3} - \frac{\mu(x+\mu-1)}{r_2^3} = 0, \\ \Omega_y = y \left( 1 - \frac{1-\mu}{r_1^3} - \frac{\mu}{r_2^3} \right) = 0. \end{cases} \quad (\text{D.2})$$

is obtained. This system has five solutions, three of which lie on the  $x$ -axis. Investigating these three collinear Lagrange points ( $L_1$ ,  $L_2$ , and  $L_3$ ) by setting  $y = 0$  in (D.2) for  $\Omega_x$  gives

$$x - \frac{(1-\mu)(x+\mu)}{|x+\mu|^3} - \mu \frac{(x+\mu-1)}{|x+\mu-1|^3} = 0. \quad (\text{D.3})$$

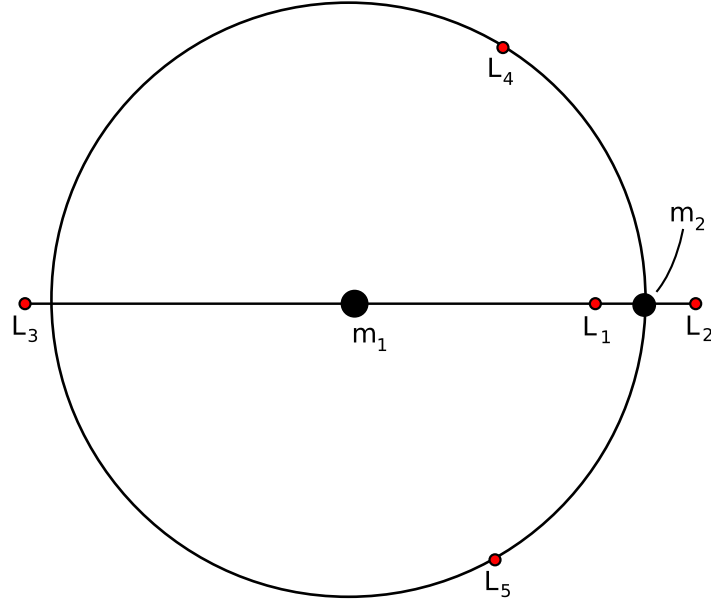


FIGURE D.1. Lagrange points of the PCR3BP.

This gives three equations, depending on the value of  $x$  relative to the position of the masses, which partition the  $x$ -axis into the three intervals

$$x < -\mu, \quad -\mu < x < 1 - \mu, \quad x > 1 - \mu.$$

In the intermediate region  $-\mu < x < 1 - \mu$ , (D.3) gives the equation

$$x - \frac{1 - \mu}{(x + \mu)^2} + \frac{\mu}{(x + \mu - 1)^2} = 0$$

for the Lagrange point  $L_1$ , which lies in between the two masses (see Figure D.1). The Lagrange point  $L_2$  beyond the secondary mass is given by

$$x - \frac{1 - \mu}{(x + \mu)^2} - \frac{\mu}{(x + \mu - 1)^2} = 0.$$

Finally, the Lagrange point  $L_3$  beyond the primary mass is given by

$$x + \frac{1 - \mu}{(x + \mu)^2} + \frac{\mu}{(x + \mu - 1)^2} = 0.$$

A quintic can now be derived from each of these equations and it can be shown that each has only one real solution.

There are also two triangular Lagrange points,  $L_4$  and  $L_5$ , which coincide with the off-axis vertex of the equilateral triangles defined by the positions of the masses (see

Figure D.1) . Since the distance between the masses has normalized non-dimensional distance 1, set  $r_1 = r_2 = 1$  (the distances from the masses to the third body) to obtain

$$(x + \mu)^2 + y^2 = (x + \mu - 1)^2 + y^2 = 1.$$

Note that this choice satisfies (D.2). The solutions are then

$$(x, y) = \left( \frac{1}{2} - \mu, \pm \frac{\sqrt{3}}{2} \right).$$

By convention, let the point with the positive  $y$ -coordinate be  $L_4$ , and that with the negative  $y$ -coordinate be  $L_5$ .

## D.2 Linearization About the Collinear Lagrange Points

Having found the Lagrange points, it now remains to locate the families of periodic Lyapunov orbits encircling them. In order to compute a Lyapunov orbit in the full nonlinear PCR3BP, periodic solutions are first found in the linearized approximation and used as a first guess for the nonlinear system. This is done by linearizing the system about the Lagrange point of interest to find the linear periodic solutions. The initial conditions from the linear periodic orbits then act as the initial guess for the nonlinear case. These initial conditions will not give closed solutions in the nonlinear system so a differential corrector is then used to give the actual periodic Lyapunov orbits.

Taking

$$x^* = \begin{pmatrix} x \\ y \\ \dot{x} \\ \dot{y} \end{pmatrix}$$

the system of equations (D.1) can be rewritten as:

$$\dot{x}^* = \bar{G}(x^*)$$

Centering the equation at a Lagrange point and linearizing yields

$$\dot{\mathbf{x}} = \mathbf{F}\mathbf{x}, \tag{D.4}$$

where  $\mathbf{F}$  is the Jacobian of  $\bar{G}$ . This gives the dynamics of the linear system with mass ratio  $\mu$  about a Lagrange point  $(l, 0)$  on the  $x$ -axis of a rotating barycentric reference frame ( $L_1$ ,  $L_2$  or  $L_3$ ). Here  $\mathbf{x} \equiv (\xi, \eta, \dot{\xi}, \dot{\eta})^\top$  is the local coordinate (e.g.,  $\xi = x - l$ ), and  $\mathbf{F}$  (the Jacobian of the linear system) is

$$\mathbf{F} \equiv \begin{pmatrix} 0 & 0 & 1 & 0 \\ 0 & 0 & 0 & 1 \\ \Omega_{xx} & \Omega_{xy} & 0 & 2 \\ \Omega_{yx} & \Omega_{yy} & -2 & 0 \end{pmatrix} \tag{D.5}$$

evaluated at the Lagrange point, where

$$\Omega_{xx} = 1 + 2c, \quad \Omega_{yy} = 1 - c, \quad \Omega_{xy} = \Omega_{yx} = 0, \quad c \equiv \frac{1 - \mu}{r_1^3} + \frac{\mu}{r_2^3}.$$

The system (D.4) has the general solution

$$\mathbf{x} = \sum_{i=1}^4 a_i \mathbf{u}_i e^{\lambda_i t}, \quad (\text{D.6})$$

where the  $\lambda_i$  and the  $\mathbf{u}_i$  are the eigenvalue-eigenvector pairs of  $F$ .

By calculating the eigenvalues of  $\mathbf{F}$ , it may be shown that they have certain relationships:  $\lambda_{1,2} = \pm \lambda_{xy}$  and  $\lambda_{3,4} = \pm i\omega_{xy}$  for  $\lambda_{xy}, \omega_{xy} \in \mathbb{R}$ , i.e.  $\mathbf{F}$  has two real and two purely imaginary eigenvalues. Furthermore, the fact that the last two elements of  $\mathbf{x}$  are derivatives of the first two gives that  $\mathbf{u}_i = (A_i, \alpha_i A_i, \lambda_i A_i, \lambda_i \alpha_i A_i)^\top$ , where

$$\alpha_i \equiv \frac{\lambda_i^2 - \Omega_{xx}}{2\lambda_i}.$$

In particular,  $\alpha_2 = -\alpha_1$  and  $\alpha_4 = -\alpha_3$ , where, explicitly,

$$\alpha_3 = i \frac{\omega_{xy}^2 + 1 + 2c}{2\omega_{xy}} \equiv ik.$$

Absorbing the constants  $a_i$  into  $A_i$ , the solutions obtained from (D.6) are

$$\begin{cases} \xi = A_1 e^{\lambda_{xy} t} + A_2 e^{-\lambda_{xy} t} + A_3 e^{i\omega_{xy} t} + A_4 e^{-i\omega_{xy} t}, \\ \eta = \alpha_1 (A_1 e^{\lambda_{xy} t} - A_2 e^{-\lambda_{xy} t}) + \alpha_3 (A_3 e^{i\omega_{xy} t} - A_4 e^{-i\omega_{xy} t}), \end{cases}$$

By appropriate coefficient transformations the following can be obtained:

$$\begin{cases} \xi = A_1 e^{\lambda_{xy} t} + A_2 e^{-\lambda_{xy} t} + A_x \cos(\omega_{xy} t + \theta), \\ \eta = \alpha_1 (A_1 e^{\lambda_{xy} t} - A_2 e^{-\lambda_{xy} t}) - k A_x \sin(\omega_{xy} t + \theta), \end{cases} \quad (\text{D.7})$$

Here  $A_x$  is the  $x$ -amplitude of the linear orbit, and  $\theta$  is a phase displacement. The solutions for  $\dot{\xi}$  and  $\dot{\eta}$  may then be found by differentiation.

### D.3 Periodic Orbits in the Linearized System

Recall that  $\mathbf{F}$  has two real eigenvalues of opposite sign, hence necessarily, in the general case, the terms corresponding to  $A_1$  and  $A_2$  will either grow or decay. For periodicity, initial conditions must then be chosen such that  $A_1$  and  $A_2$  vanish. Therefore set  $A_1 =$

$A_2 = 0$  and evaluate the resulting expressions in (D.7) and their derivatives at  $t = 0$ , to obtain the initial condition  $\mathbf{x}_0$ :

$$\begin{cases} \xi_0 = A_x \cos \theta, \\ \eta_0 = -k A_x \sin \theta, \\ \dot{\xi}_0 = -\omega_{xy} A_x \sin \theta, \\ \dot{\eta}_0 = -\omega_{xy} k A_x \cos \theta. \end{cases} \quad (\text{D.8})$$

These relations must hold for any initial condition on a linear Lyapunov orbit of  $x$ -amplitude  $A_x$ . The period of the orbit is  $T \equiv 2\pi/\omega_{xy}$ .

A sample graphical display is shown below in Figure D.2. Shown in the top diagrams are the position and velocity coordinates of a sample periodic orbit in the linearized system about the  $L_1$  Lagrange point in the Earth-Moon system derived using the method described above. As required, this linear orbit is closed in both position and velocity space, with period  $T$ . A direct comparison can be made to the orbits in the nonlinear system as shown in the second row of diagrams. These show the orbits derived by integrating the full nonlinear equations of motion forward from the same initial conditions as used for the linear periodic orbits. This demonstrates the lack of correspondence between a linear and nonlinear periodic orbit, and so the need for a differential corrector to close the orbit in the nonlinear case.

## D.4 Lyapunov Orbits by Differential Correction

Using the above methods it is possible to compute periodic orbits about the collinear Lagrange points ( $L_1$ ,  $L_2$ , and  $L_3$ ) in the corresponding linearized systems. However these linearized approximations do not close in the relevant nonlinear system (see Figure D.2). Discussed here is the differential corrector method for closing these nonlinear orbits. Once closed, the nonlinear orbits obtained from the linear initial conditions form the periodic Lyapunov orbits.

Let  $\mathbf{x}(t) \equiv (x(t), y(t), \dot{x}(t), \dot{y}(t))^T$  be a state vector of interest with initial condition  $\mathbf{x}_0 \equiv \mathbf{x}(t_0)$ . Consider the perturbation

$$\delta \mathbf{x}(t) = \mathbf{x}(\mathbf{x}_0 + \delta \mathbf{x}_0, t + \delta t) - \mathbf{x}(\mathbf{x}_0, t), \quad (\text{D.9})$$

The Taylor expansion gives

$$\delta \mathbf{x}(t) = \frac{\partial \mathbf{x}(\mathbf{x}_0, t)}{\partial \mathbf{x}_0} \delta \mathbf{x}_0 + \dot{\mathbf{x}}(\mathbf{x}_0, t) \delta t + O(\delta^2) \approx \Phi(t, t_0) \delta \mathbf{x}_0 + \dot{\mathbf{x}}(\mathbf{x}_0, t) \delta t, \quad (\text{D.10})$$

where  $\delta^2$  denotes multiplications of second order or higher of the perturbation elements  $\delta \mathbf{x}_0$  or  $\delta t$ , and  $\Phi(t, t_0) \equiv (\Phi_{ij}) = \partial \mathbf{x}(\mathbf{x}_0, t) / \partial \mathbf{x}_0$ .

For the PCR3BP, start with an initial condition for a linear orbit obtained analytically. For convenience, let this initial condition coincide with the  $x$ -axis. Integrate this

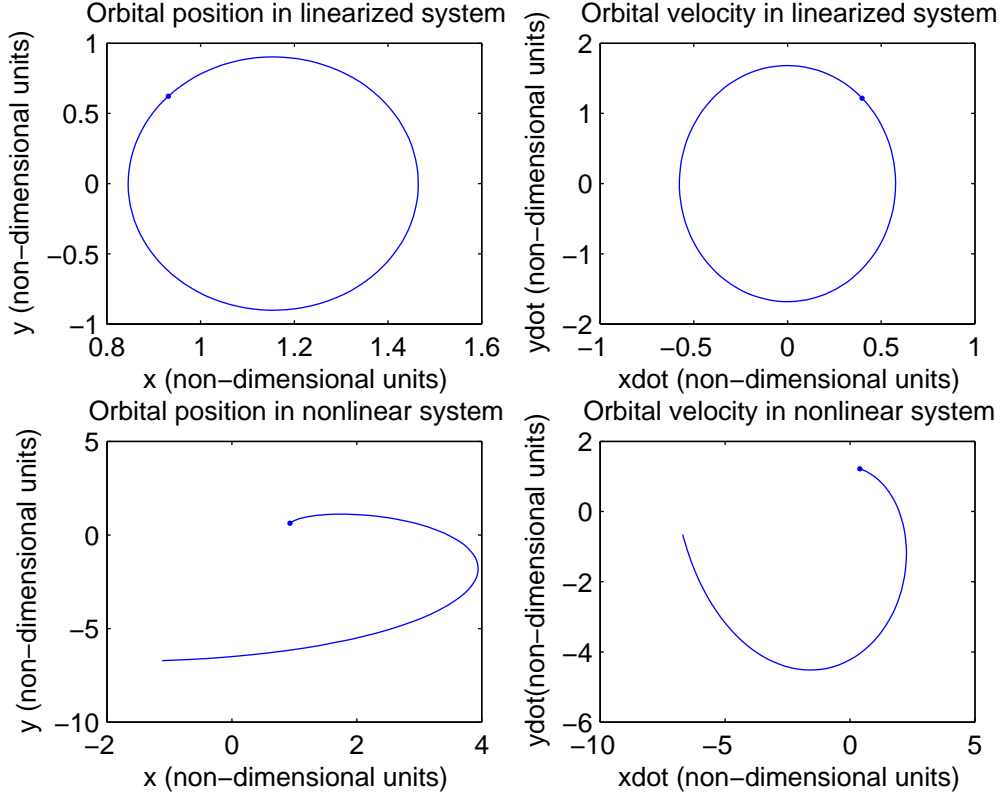


FIGURE D.2. A comparison of periodic orbits in the linear system to orbits derived by integrating forward the same initial conditions in the full nonlinear system. Dots denote initial conditions.

initial condition using the full nonlinear dynamics of the system

$$\dot{\mathbf{x}} = f(\mathbf{x}) \quad (\text{D.11})$$

until the solution again reaches  $y = 0$  at time  $t = t_1$ . Although the linear orbits do show significant divergence from periodicity in the nonlinear system, the existence of  $t$  is generally not a concern. The symmetry of the system (D.11) under the transformation  $y \mapsto -y$ ,  $t \mapsto -t$  necessarily requires that the solution cross the  $x$ -axis perpendicularly, i.e, that

$$y_1 = y_0 = \dot{x}_1 = \dot{x}_0 = 0, \quad (\text{D.12})$$

where  $\mathbf{x}_1 \equiv \mathbf{x}(t_1)$ . Thus, letting  $\delta\mathbf{x}_1$  and  $\delta\mathbf{x}_0$  be the correction vectors for the Lyapunov orbit at  $t = t_1$  and  $t = t_0$ , respectively, the following are obtained:  $\delta y_1 = 0$  and  $\delta \dot{x}_1 = -\dot{x}_1$ . The approach then is to solve for  $\delta\mathbf{x}_0$  via (D.10). There is first, however, a need to obtain  $\Phi(t, t_0)$ .



The matrix  $\Phi(t, t_0)$  appearing in (D.10) is the state transition matrix associated with the initial condition  $\mathbf{x}_0$ . Derive a differential equation for  $\Phi(t, t_0)$  as follows. By the chain rule

$$\dot{\Phi}(t, t_0) = \frac{d}{dt}\Phi(t, t_0) = \frac{d}{dt} \left[ \frac{\partial \mathbf{x}(t)}{\partial \mathbf{x}_0} \right] = \frac{\partial \dot{\mathbf{x}}(t)}{\partial \mathbf{x}_0} = \frac{\partial f(\mathbf{x})}{\partial \mathbf{x}_0} = f'(\mathbf{x}) \frac{\partial \mathbf{x}(t)}{\partial \mathbf{x}_0} = \mathbf{F}\Phi(t, t_0).$$

where it may be shown that

$$\mathbf{F} = \begin{pmatrix} 0 & 0 & 1 & 0 \\ 0 & 0 & 0 & 1 \\ \Omega_{xx} & \Omega_{xy} & 0 & 2 \\ \Omega_{xy} & \Omega_{yy} & -2 & 0 \end{pmatrix} = \begin{pmatrix} 0 & 0 & 1 & 0 \\ 0 & 0 & 0 & 1 \\ 1+2c & d & 0 & 2 \\ d & 1-c & -2 & 0 \end{pmatrix},$$

where

$$c \equiv \frac{1-\mu}{r_1^3} + \frac{\mu}{r_2^3}, \quad d \equiv 3y \left[ \frac{(1-\mu)(x+\mu)}{r_1^5} + \frac{\mu(x+\mu-1)}{r_2^5} \right].$$

Thus, for the differential corrector, there is a need to integrate the system

$$\begin{cases} \dot{\mathbf{x}} = f(\mathbf{x}), \\ \dot{\Phi} = \mathbf{F}\Phi, \end{cases} \quad (\text{D.13})$$

which, for the two-dimensional case, has a solution vector of 20 elements.

The requirements from the symmetries of the equation i.e. that  $y_1 = y_0 = \dot{x}_1 = \dot{x}_0 = 0$ , applied to (D.25) gives

$$\begin{pmatrix} \delta x_1 \\ 0 \\ -\dot{x}_1 \\ \delta \dot{y}_1 \end{pmatrix} = \Phi(t_1, t_0) \begin{pmatrix} \delta x_0 \\ 0 \\ 0 \\ \delta \dot{y}_0 \end{pmatrix} + \begin{pmatrix} \dot{x}_1 \\ \dot{y}_1 \\ \ddot{x}_1 \\ \ddot{y}_1 \end{pmatrix} \delta t,$$

Rearranging the second row for  $\delta t$  gives

$$\delta t = -\frac{1}{\dot{y}_1} \begin{pmatrix} \Phi_{21} & \Phi_{24} \end{pmatrix} \begin{pmatrix} \delta x_0 \\ \delta \dot{y}_0 \end{pmatrix},$$

which can then be substituted back into the equation to give

$$\begin{pmatrix} \delta x_1 \\ 0 \\ -\dot{x}_1 \\ \delta \dot{y}_1 \end{pmatrix} = \left[ \begin{pmatrix} \Phi_{11} & \Phi_{14} \\ \Phi_{21} & \Phi_{24} \\ \Phi_{31} & \Phi_{34} \\ \Phi_{41} & \Phi_{44} \end{pmatrix} - \frac{1}{\dot{y}_1} \begin{pmatrix} \dot{x}_1 \\ \dot{y}_1 \\ \ddot{x}_1 \\ \ddot{y}_1 \end{pmatrix} \begin{pmatrix} \Phi_{21} & \Phi_{24} \end{pmatrix} \right] \begin{pmatrix} \delta x_0 \\ \delta \dot{y}_0 \end{pmatrix}.$$

There are no constraints on  $\delta x_1$  or  $\delta \dot{y}_1$ , but  $\delta \dot{x}_1$  is required to be 0 so consider only that component, and rearrange to obtain

$$-\dot{x}_1 = \left[ \begin{pmatrix} \Phi_{31} & \Phi_{34} \end{pmatrix} - \frac{\ddot{x}_1}{\dot{y}_1} \begin{pmatrix} \Phi_{21} & \Phi_{24} \end{pmatrix} \right] \begin{pmatrix} \delta x_0 \\ \delta \dot{y}_0 \end{pmatrix}.$$

There are now two convenient choices, set either  $\delta x_0 = 0$  or  $\delta \dot{y}_0 = 0$ , which correspond to the corrections

$$\delta \dot{y}_0 = -\frac{\dot{x}_1}{\Phi_{34} - (\ddot{x}_1/\dot{y}_1) \Phi_{24}} \quad \text{and} \quad \delta x_0 = -\frac{\dot{x}_1}{\Phi_{31} - (\ddot{x}_1/\dot{y}_1) \Phi_{21}},$$

respectively. The convergence of these equations is discussed in [19]. For a more in depth discussion of this derivation, see [9]

For a comparison of the two methods (setting either  $\delta x_0 = 0$  or  $\delta \dot{y}_0 = 0$ ) see the following figures (Figures D.3, D.4 respectively). These show the orbits obtained from integrating the initial conditions from the linear system forward in the full nonlinear system and set of corrected orbits. The first orbit is the red line starting on the far right, showing the lack of correlation between a linear periodic orbit and a nonlinear one. The other red lines then correspond to the iterations of the differential corrector in the nonlinear system. The final corrected orbit for the nonlinear system is shown in blue. Both methods work well, converging in 8 iterations, and so in this project's MATLAB code we have routines for holding either  $\delta x_0 = 0$  or  $\delta \dot{y}_0 = 0$ . (The number of iterations is usually similar for the two methods, but here they just happen to be the same.)

Using the above corrections, it is possible to obtain periodic solutions from any given initial conditions derived from the linear system, though the number of iterations of the differential corrector may vary enormously depending on the validity of the initial conditions. For a direct comparison of an example of a closed periodic linear approximation, and its corresponding, corrected full nonlinear orbit see Figure D.5. Shown there are the orbits in the linear approximation and nonlinear system around the Earth-Moon L2 point with x-amplitude (distance from the Lagrange point) of 0.0305187. The misalignment of the blue nonlinear return trajectory with the initial condition is due to integration error.

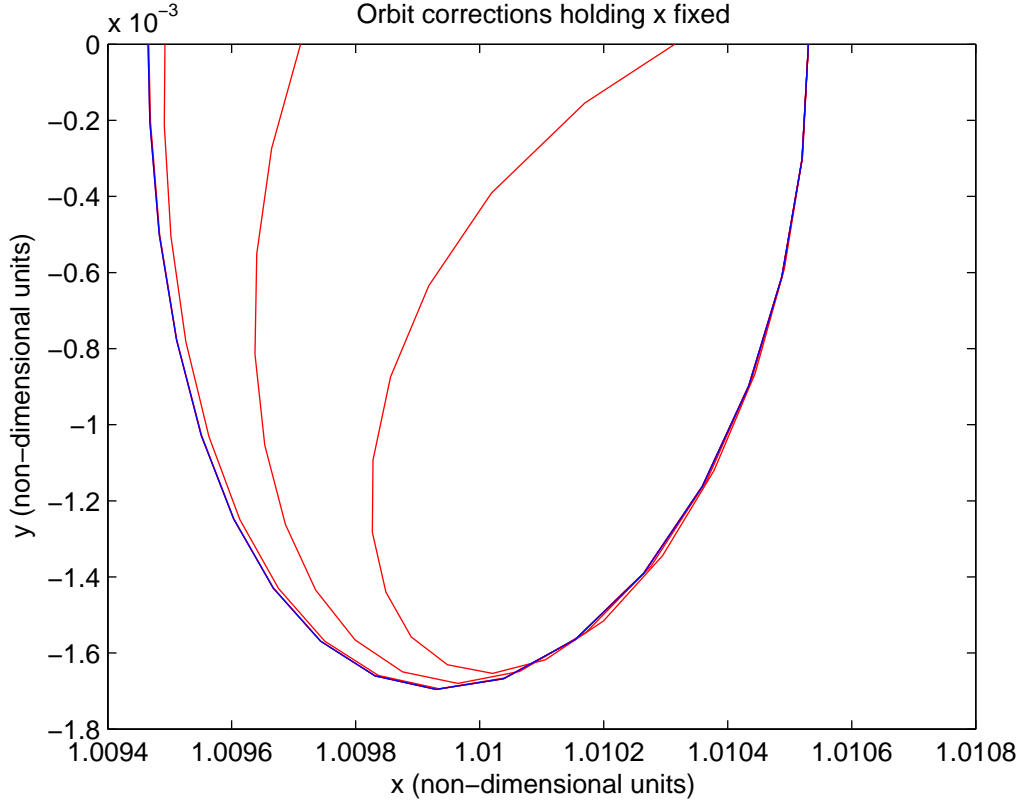


FIGURE D.3. Lyapunov orbit corrections with  $\delta x_0 = 0$ . Red, intermediate orbits; blue, corrected orbit.

## D.5 Stability Directions: The Monodromy Matrix

In the following sections, a method for computing the monodromy matrix from the state transition matrix will be outlined. The monodromy matrix is useful for determining first-order stability properties of the Lyapunov orbits found previously. These stable and unstable directions will then be used to generate the invariant manifolds of each three-body system.

The monodromy matrix is defined as

$$M_0 \equiv \Phi(T, 0),$$

where  $\Phi$  is the state transition matrix and  $\Phi(0, 0) = I$ . The state transition matrix is determined from

$$\begin{aligned} \dot{\Phi} &= F\Phi \\ \dot{\mathbf{x}} &= f(\mathbf{x}), \end{aligned} \tag{D.14}$$

where  $f$  corresponds to equation (D.1) converted to a system of four first-order ODEs and  $F$  is a 4x4 matrix which is found by linearizing  $f$  around  $\mathbf{x}$ . As mentioned in the

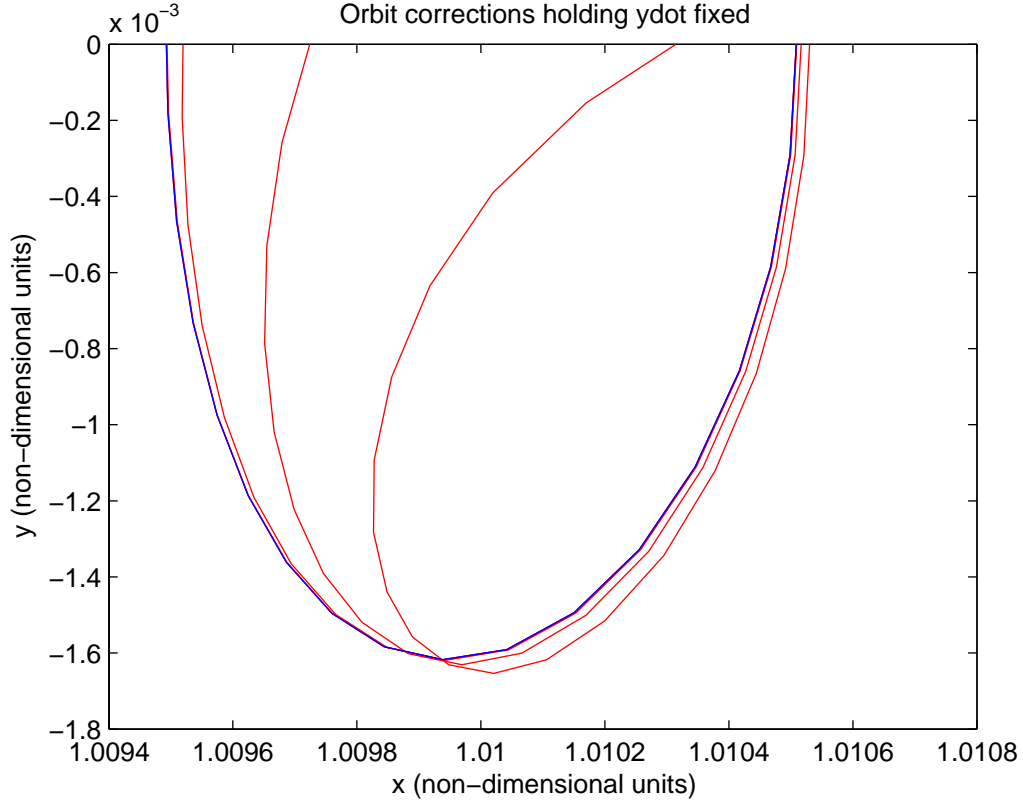


FIGURE D.4. Lyapunov orbit corrections with  $\delta\dot{y}_0 = 0$ . Red, intermediate orbits; blue, corrected orbit.

previous chapter, equation (D.1) is invariant under the transformations

$$\begin{aligned} t &\rightarrow -t \\ y &\rightarrow -y. \end{aligned} \tag{D.15}$$

Remembering that  $\mathbf{x} = (x \ y \ \dot{x} \ \dot{y})^T$ , define a new vector

$$\mathbf{y} = A\mathbf{x}, \tag{D.16}$$

where

$$A = \begin{pmatrix} 1 & 0 & 0 & 0 \\ 0 & -1 & 0 & 0 \\ 0 & 0 & -1 & 0 \\ 0 & 0 & 0 & 1 \end{pmatrix}.$$

By (D.15), every  $\mathbf{x}(t)$  which solves the equations of motion for the three body problem has a corresponding  $\mathbf{y}(t)$  which is also a solution. For the solution  $\mathbf{x}(t)$ ,

$$\mathbf{x}_1 = \Phi(t_1, t_0)\mathbf{x}_0,$$

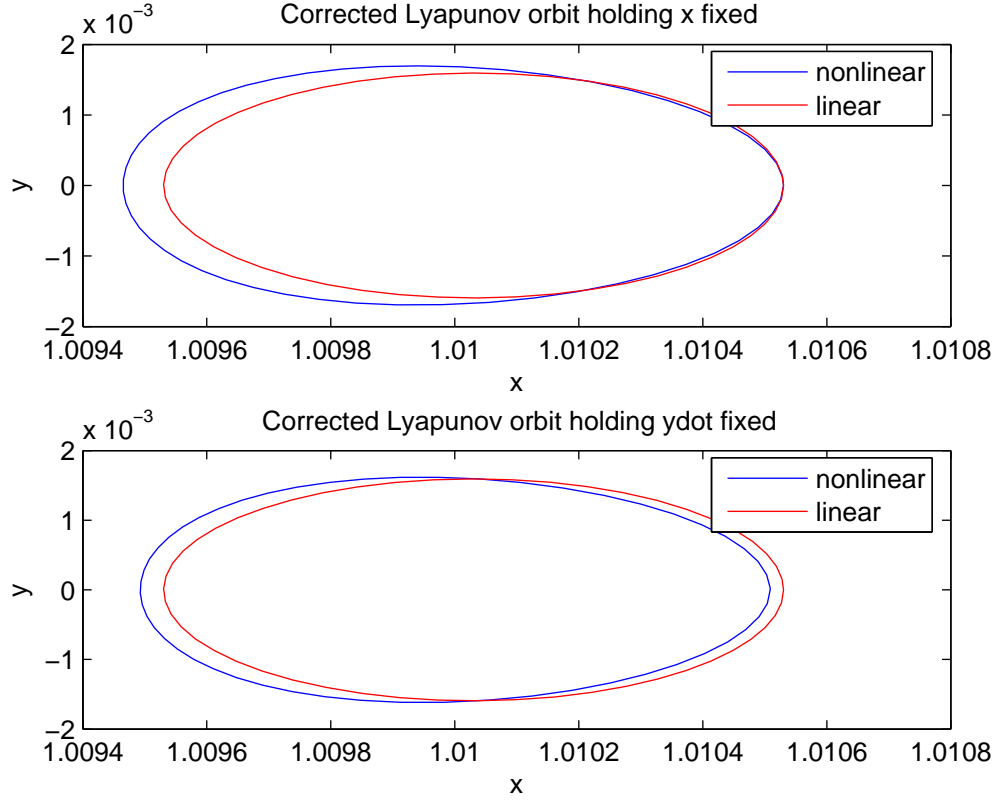


FIGURE D.5. Lyapunov orbits corrected using either  $\delta x_0 = 0$  or  $\delta \dot{y}_0 = 0$  compared with their linear approximations. Blue, nonlinear; red, linear.

where  $\Phi$  is the state transition matrix,  $\mathbf{x}_0 = \mathbf{x}(t_0)$ , and  $\mathbf{x}_1 = \mathbf{x}(t_1)$ . Similarly,

$$\mathbf{y}_1 = \Psi(t_1, t_0)\mathbf{y}_0,$$

where  $\Psi$  is another state transition matrix,  $\mathbf{y}_0 = \mathbf{y}(t_0)$ , and  $\mathbf{y}_1 = \mathbf{y}(t_1)$ . Using (D.16), one finds

$$\Psi(t_1, t_0) \equiv A\Phi(t_1, t_0)A. \quad (\text{D.17})$$

By (D.15),

$$\Psi(T/2, 0) = \Phi(-T/2, 0). \quad (\text{D.18})$$

See Figure D.6 for a visual representation of (D.18).

A property of the state transition matrix is that

$$\Phi(t_2, 0) = \Phi(t_2, t_1)\Phi(t_1, 0). \quad (\text{D.19})$$

Equations (D.16) and (D.18), along with the above property, give

$$\Phi(T, 0) = \Psi^{-1}\left(\frac{T}{2}, 0\right)\Phi\left(\frac{T}{2}, 0\right).$$

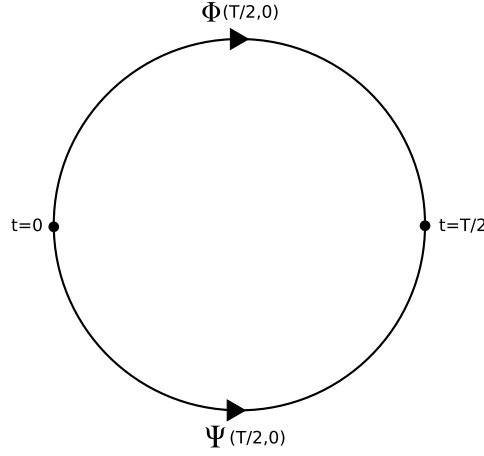


FIGURE D.6. A diagram showing of the relationship between the transition matrices  $\Phi$  and  $\Psi$ .

Using (D.17),

$$M_0 = \Phi(T, 0) = A\Phi^{-1}\left(\frac{T}{2}, 0\right)A\Phi\left(\frac{T}{2}, 0\right). \quad (\text{D.20})$$

In other words, the monodromy matrix  $\Phi(T, 0)$  can be calculated using  $\Phi(T/2, 0)$ . In this way, the symmetry of equations (D.1) is used to reduce numerical integration error, since equations (D.14) need to be integrated for only half the normally required time.

Basic properties of the state transition matrix give the relationships

$$\begin{aligned} \mathbf{x}(T) &= M_0\mathbf{x}(0) \\ \mathbf{x}(T+t) &= M_t\mathbf{x}(t) \\ \mathbf{x}(s+t) &= \Phi(s+t, s)\mathbf{x}(s), \end{aligned} \quad (\text{D.21})$$

where  $T$  is the period of the Lyapunov orbit. Now

$$\begin{aligned} M_t\mathbf{x}(t) &= \mathbf{x}(T+t) \\ &= \Phi(T+t, T)\mathbf{x}(T) \\ &= \Phi(T+t, T)M_0\mathbf{x}(0), \end{aligned} \quad (\text{D.22})$$

but  $\mathbf{x}(t) = \Phi(t, 0)\mathbf{x}(0)$ , so

$$M_t = \Phi(T+t, T) M_0 \Phi^{-1}(t, 0). \quad (\text{D.23})$$

Consider the monodromy matrix  $M_0$ . Let  $\mathbf{v}$  the eigenvector of  $M_0$  associated with the eigenvalue  $\lambda$ , so that

$$M_0\mathbf{v} = \lambda\mathbf{v}.$$

From (D.23),

$$M_t\Phi(t, 0)\mathbf{v} \approx \lambda\Phi(t, 0)\mathbf{v}, \quad (\text{D.24})$$

since  $\Phi(t, 0) \approx \Phi(T+t, T)$ . Equation (D.24) gives a relationship between the eigenvectors of  $M_0$  and the eigenvectors of  $M_t$  without having to propagate the state transition matrix forward in time one period. The eigenvectors of the monodromy matrix, paired with their corresponding eigenvalues, give the stable and unstable directions projecting from each point on the Lyapunov orbit. Perturbing along these eigenvectors and integrating forwards and backwards in time, one can compute the stable and unstable manifolds of the PCR3BP, as will be outlined in a following section.

## D.6 Integration of Perturbations Along the Stability Directions

$M_0$  can now be used along with results concerning the eigenvalues and eigenvectors of the more general class of monodromy matrices  $M_t \equiv \Phi(T+t, t)$  to compute the first-order approximations of the stable and unstable manifolds projecting from a given Lyapunov orbit. The concept of interest here is the Lyapunov exponent,

$$|\delta \mathbf{x}(t)| = e^{\lambda t} |\delta \mathbf{x}_0|. \quad (\text{D.25})$$

Eigenvalues  $\lambda$  of modulus greater than unity correspond to (unstable) diverging trajectories; those of modulus less than unity correspond to (stable) converging ones.

Consider a Lyapunov orbit about some Lagrange point of interest and compute the stable and unstable directions on a given mesh of points along the orbit. The eigenvectors determine the direction of the first-order approximations to the actual invariant manifolds. At each of these mesh points, a perturbation will evolve and either grow or decay depending on the stability of the associated eigenvalue.

Sample output is given in Figure D.7, where we have plotted the stable and unstable manifolds of a Lyapunov Orbit around the lunar  $L_2$  with a given Jacobi constant. Of particular interest is the symmetry of the stable and unstable manifolds: due to the symmetry of the system under the transformation  $t \mapsto -t$ ,  $y \mapsto -y$ , integration of the unstable manifold forward in time is equivalent to integration of the stable manifold backward in time across the  $x$ -axis.

## D.7 Manifold Propagation: Parameter Considerations and Adaptive Methods

Recall that manifolds in the PCR3BP are generated by perturbing initial conditions sampled from a Lyapunov orbit and then integrating either forwards or backwards in time. The perturbation directions are given by the eigenvectors of the monodromy matrix. The perturbations must be small, as the eigenvectors are only linear approximations of the true stability directions. In early computations, the perturbation magnitude was arbitrarily chosen to be  $\|\delta \mathbf{x}\| = 10^{-4}$ . This value was selected using medium  $LL_2$  Lyapunov orbits ( $0.01 < A_x < 0.02$ ) in the non-dimensionalized rotating Earth-Moon frame, integrated out for 1.25 times the orbital period, based on visualization reasons.

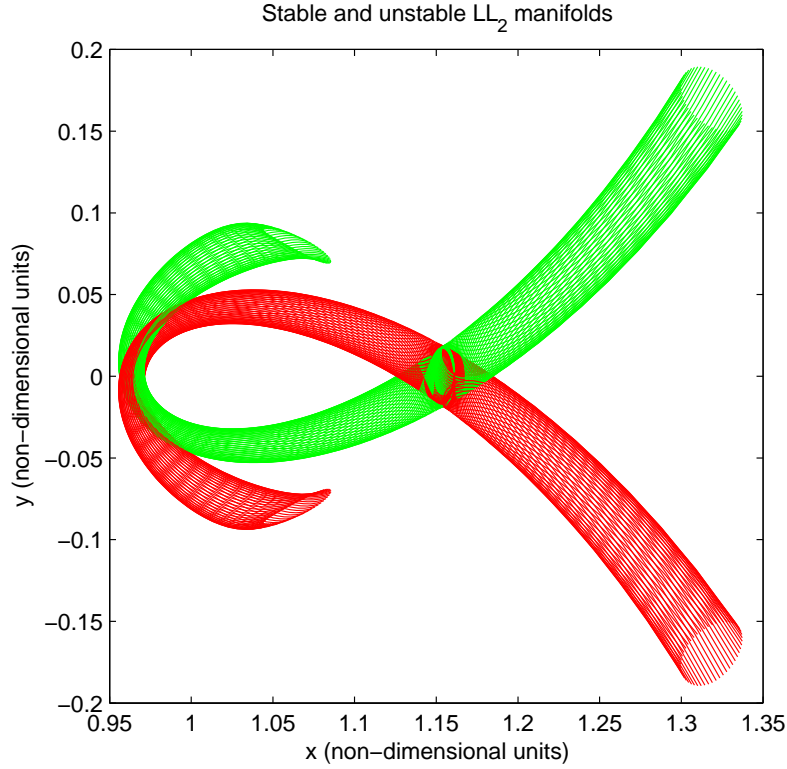


FIGURE D.7. The stable and unstable manifolds projecting from a Lyapunov orbit about the Earth-Moon  $L_2$  point corresponding to Jacobi constant  $J \approx 3.158436$ . The stable trajectories are green and the unstable ones are red. The Lyapunov orbit is centered at  $x \approx 1.1551$ . The moon is located at  $(1-0.012, 0)$  and the Earth is located at  $(0.012, 0)$ .

Due to the *ad hoc* nature of this choice, it was not surprising when difficulties arose, particularly when considering significantly smaller or larger orbits, or when considering  $EL_2$  Lyapunov orbits (this second case, after scaling, is equivalent to the first). Simply put, the fixed perturbation magnitude approach did not have the flexibility necessary to compensate for the impressive range of variation exhibited by these orbits. Indeed, when considering small orbits, the perturbation  $\|\delta\mathbf{x}\| = 10^{-4}$  was too large compared to the orbital size. In addition, the perturbation directions lacked accuracy (though admittedly, this was probably not a significant effect). On the other hand, when considering large orbits, the same  $\|\delta\mathbf{x}\|$  resulted in trajectories that stayed close to the Lyapunov orbit for too long before escaping. Plots of such trajectories with a fixed integration time showed only their slow winding around the orbit and little, of the manifold structure of interest. In fact, this orbital winding can cause complications in subsequent analyses.

From these observations, it seems logical to pursue an algorithm where the pertur-



bation magnitude depends upon the size of the Lyapunov orbit in question. Of course, the term “size” is imprecise, hence we consider instead the Jacobi constant of the orbit. What is desired, then, is a scaling function which takes as inputs a Jacobi constant  $J$  and a mass ratio  $\mu$ , and returns an appropriate perturbation magnitude  $\|\delta\mathbf{x}\|$ . The magnitude should be chosen so that it preserves both the accuracy of the propagation direction and a time of orbital escape which is not too long. This chapter details the determination, implementation, and evaluation of this function.

In addition to the magnitude of the perturbation away from the Lyapunov orbit  $\|\delta\mathbf{x}\|$ , another parameter plays an important part in the propagation of the manifolds. Supposing that the propagation of the manifolds begins at time  $t = 0$ , the parameter to be considered is the end time of integration  $T$ . This parameter obviously controls the qualitative character of the manifolds by restricting the region of interest temporally. For example, the manifolds tend to wrap around and cross themselves spatially given enough time. By an appropriate choice of  $T$ , complicated behaviors, which have the potential to make analysis of the manifolds more difficult, may be avoided.

Although it is possible, in principle, to develop a fully adaptive manifold propagation scheme implementing both variable  $T$  and variable  $\|\delta\mathbf{x}\|$ , it is simpler, and arguably, more natural, to consider a partial adaptive method by letting  $T$  be the period of the Lyapunov orbit in question. The problem then reduces (in a rough sense) to choosing a suitable  $\|\delta\mathbf{x}\|$ . Clearly, the choice of  $\|\delta\mathbf{x}\|$  as the “free parameter” gives sufficient freedom to avoid the difficulties encountered above.

## D.7.1 Criteria for Perturbation Magnitude Selection

The natural question now is how one might appropriately choose  $\|\delta\mathbf{x}\|$  for a given Lyapunov orbit. Two useful criteria are outlined below.

### D.7.1.1 Speed of Orbital Escape

As discussed previously, one criterion that may be imposed is a reasonable time of orbital escape for the manifold trajectories. More precisely, the quasi-stable behavior of trajectories very close to the Lyapunov orbit is not of interest to determining the shape of the manifolds, hence  $\|\delta\mathbf{x}\|$  must be sufficiently large such that the trajectories actually map out the entire manifold structure by time  $t = T$ . This, then, in some sense, gives a lower bound on  $\|\delta\mathbf{x}\|$ .

### D.7.1.2 The First-Pass Restriction

Although not a necessary restriction, only the “first pass” of manifolds will be considered for this research. In this way, the self-crossing discussed earlier is not observed. Therefore, the adaptive perturbation magnitude model must satisfy this first-pass restriction. Numerical explorations have shown that suitable manifold transfers exist under this restriction, hence there is some validation for its imposition. Moreover, second (and higher)

passes tend to lose accuracy of approximation in the full four-body dynamics due to the accumulation of higher-order effects as the time of integration is increased; hence this restriction also preserves the validity of the approximation for the manifolds propagated. Therefore, an upper bound on  $\|\delta\mathbf{x}\|$  is obtained.

## D.7.2 An Adaptive Perturbation Magnitude Scheme for Manifold Propagation

### D.7.2.1 Modeling the Jacobi Scaling Function

A suitable form for the Jacobi scaling function described may be obtained by imposing a particular functional form on the scaling function. We may then use this functional form as a model of the scaling function, using best-fit parameters to produce perturbation magnitudes. Only the  $L_2$  manifolds have been considered.

### D.7.2.2 Power Law Fitting

Numerical explorations have demonstrated that for fixed  $\mu$ , a reasonable model for the Jacobi scaling function is a power law. Therefore, we consider the perturbation model

$$\|\delta\mathbf{x}\| \equiv \alpha_1 + \alpha_2 (J - \alpha_3)^{\alpha_4} \quad (\text{D.26})$$

in the four parameters  $\alpha_1, \dots, \alpha_4$ .

### D.7.2.3 Model Parameters

The model parameters  $\alpha_1, \dots, \alpha_4$  give the power law (D.26) sufficient degrees of freedom to appropriately adapt to the manifold propagation data. These parameters have the following interpretations:  $\alpha_1$  is the basal perturbation magnitude,  $\alpha_2$  the scaling ratio,  $\alpha_3$  the Jacobi constant corresponding to  $\|\delta\mathbf{x}\| = \alpha_1$ , and  $\alpha_4$  is the exponent. Optimal values for these parameters will be determined by least-squares fitting on generated data satisfying the perturbation magnitude criteria discussed.

### D.7.2.4 Least-Squares Model Parameter Fitting

To prepare for least-squares parameter fitting, we generate sample data consisting of pairs  $(J, \|\delta\mathbf{x}\|)$  satisfying the evaluation criteria.

As a visualization, some sample manifolds manually deemed to be in satisfaction of the evaluation criteria are shown in Figures D.8–D.10. All manifolds were integrated out to one period of their associated Lyapunov orbit. Observe that in each of the three figures,  $\|\delta\mathbf{x}\|$  was large enough that the manifold structures of interest (the “tubes”) were sufficiently propagated; on the other hand,  $\|\delta\mathbf{x}\|$  was also small enough that none of the figures exhibited significant self-crossing of the manifolds. This is in contrast to

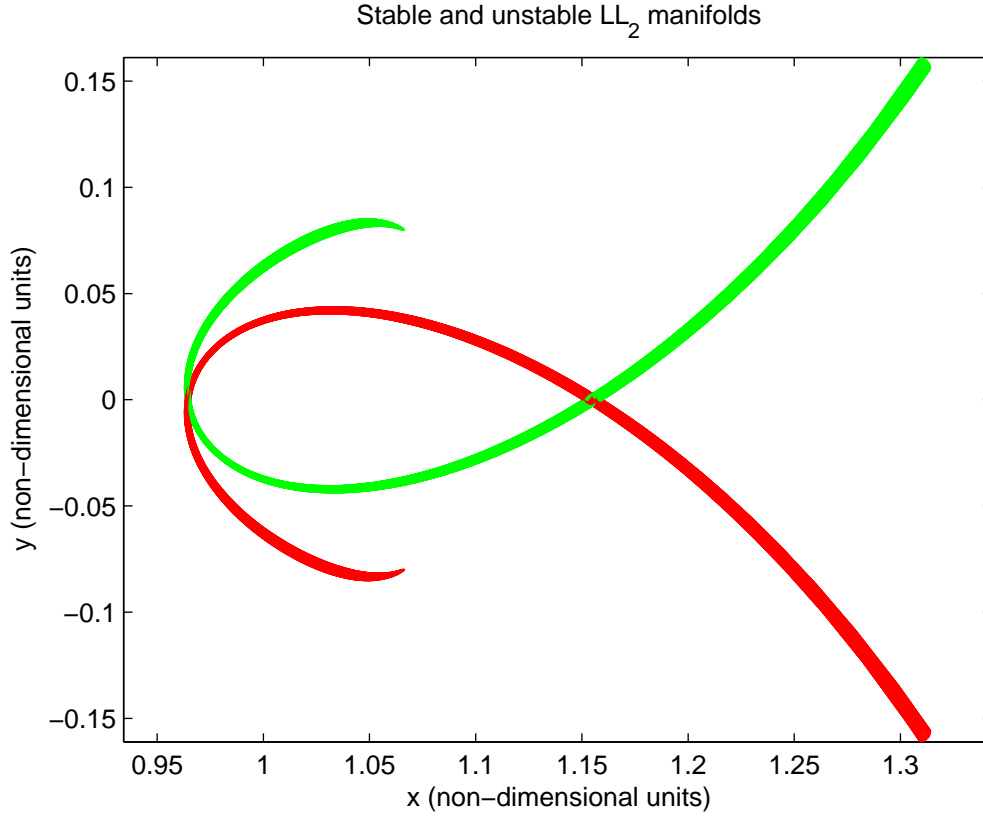


FIGURE D.8. Stable and unstable manifolds satisfying the evaluation criteria. The manifolds are propagated from the  $LL_2$  Lyapunov orbit with Jacobi constant  $J \approx 3.159090$ , and zero-angle initial condition  $x_0 \approx 9.923427 \times 10^{-4}$ . Green, stable manifold; red, unstable manifold.

the situation shown in Figure D.11, for which the value of  $\|\delta\mathbf{x}\|$  was greater than the upper bound imposed by the first-pass restriction. A general rule of thumb that we have used in specifying proper values of  $\|\delta\mathbf{x}\|$  is to generate manifolds whose left branches are propagated only very slightly past their inflection points.

#### D.7.2.5 Bounds on the Jacobi Constants

Within the database the Jacobi constant limits were chosen, using methods described earlier in the chapter, to be neither too 'large' nor too 'small'.

After the parametric study of the database to search for intersections with circular orbits of either the Moon or Earth there are further restrictions on the Jacobi Constants:

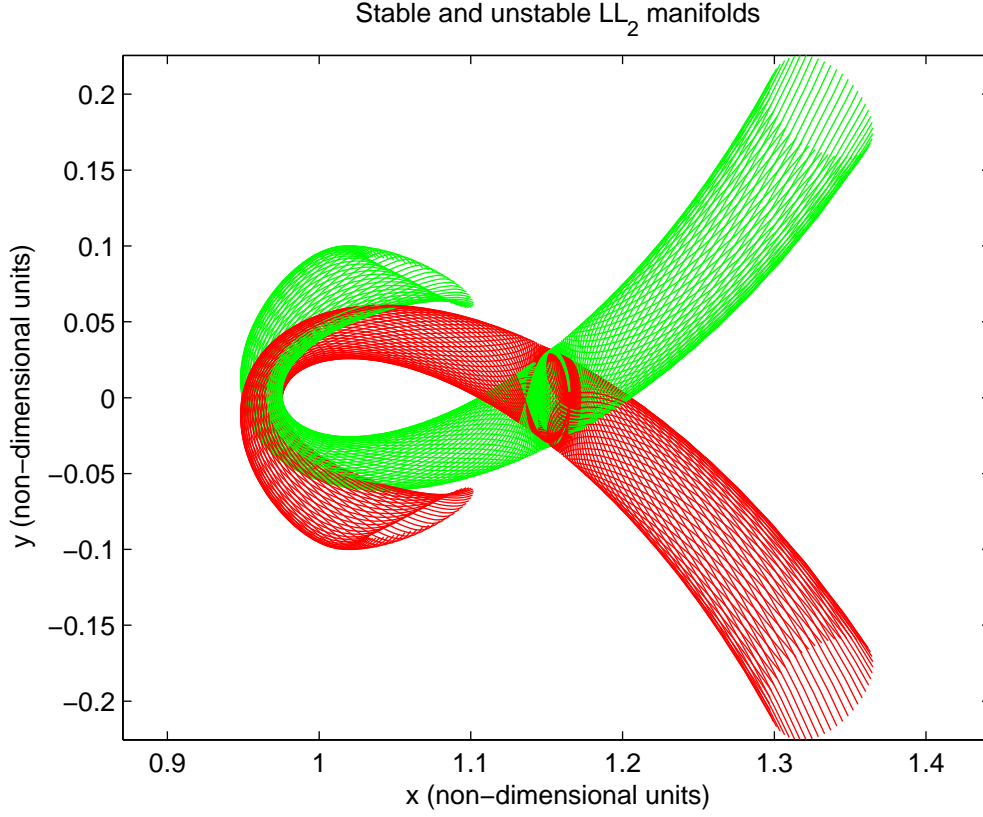


FIGURE D.9. Stable and unstable manifolds satisfying the evaluation criteria. The manifolds are propagated from the  $LL_2$  Lyapunov orbit with Jacobi constant  $J \approx 3.156616$ , and zero-angle initial condition  $x_0 \approx 0.010001$ . Green, stable manifold; red, unstable manifold.

System	Minimum Jacobi Constant	Maximum Jacobi Constant
Sun-Earth-SC	3.00064111	3.00088267
Earth-Moon-SC	3.13941	3.15909

TABLE D.1. Jacobi constant bounds in the manifold database.

Intersection with	Minimum Jacobi Constant	Maximum Jacobi Constant
Earth	3.00070100	3.00081614
Moon	3.13941	3.15226

TABLE D.2. Jacobi constant bounds for intersection with LEO and LO.

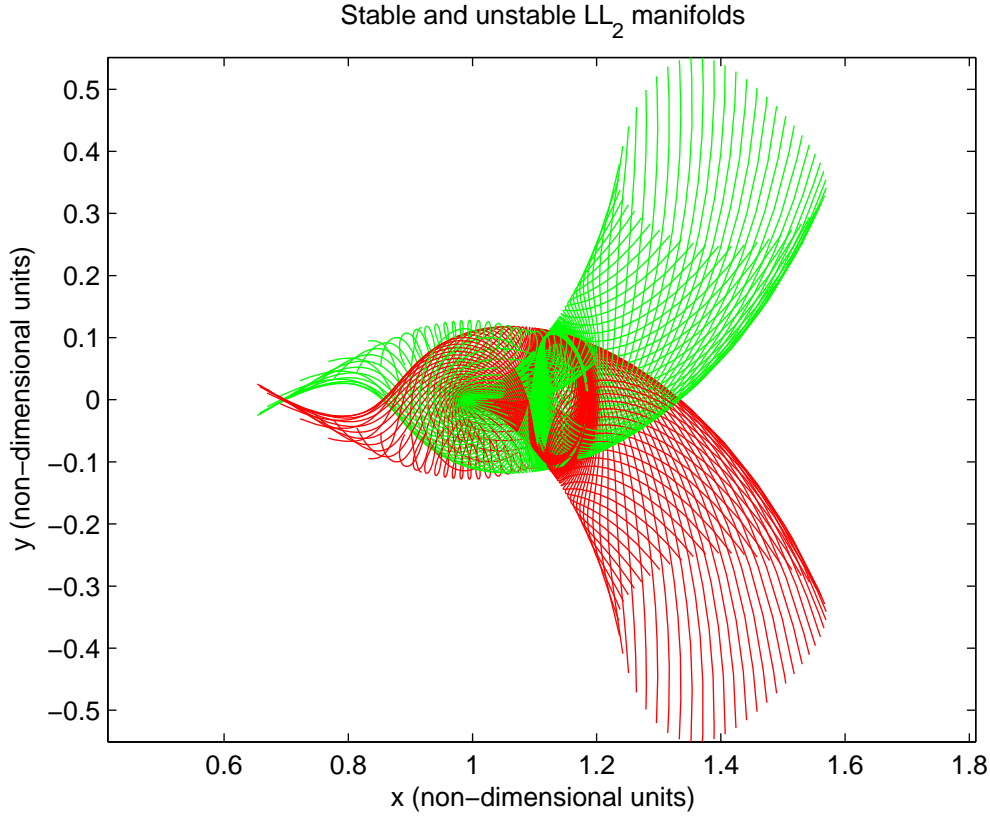


FIGURE D.10. Stable and unstable manifolds satisfying the evaluation criteria. The manifolds are propagated from the  $LL_2$  Lyapunov orbit with Jacobi constant  $J \approx 3.127846$ , and zero-angle initial condition  $x_0 \approx 0.029997$ . Green, stable manifold; red, unstable manifold.

### D.7.3 Results

The vast majority of manifolds propagated with the implemented adaptive perturbation magnitude scheme satisfy the evaluation criteria. Indeed, Figures D.8–D.10 were generated by the adaptive approach. These figures, then, are characteristic of the results obtained, and show the general suitability of this adaptive method. In the process of implementing these Jacobi scaling functions, several possible extensions of the derivation were noted. These are discussed briefly below.

#### D.7.3.1 Fully Adaptive Integration End Time

It may be worthwhile to pursue a fully adaptive model with no constraints on either of the parameters  $T$  or  $\|\delta\mathbf{x}\|$ . We may consider, for example, a Jacobi scaling function of

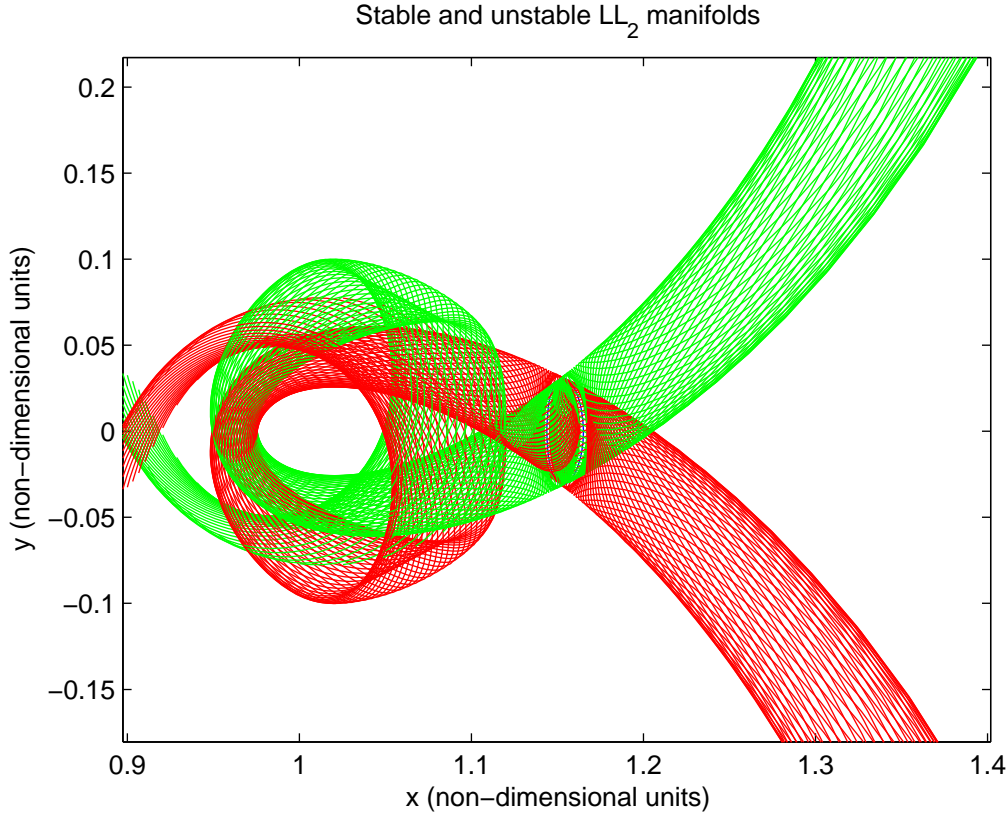


FIGURE D.11. Stable and unstable manifolds violating the first-pass restriction. The manifolds are propagated from the  $LL_2$  Lyapunov orbit with Jacobi constant  $J \approx 3.156616$ , and zero-angle initial condition  $x_0 \approx 0.010001$  (the same case as in Figure D.9). Green, stable manifold; red, unstable manifold. Notice the significant self-crossing of the manifold branches on the left.

the form

$$(T, \|\delta \mathbf{x}\|) = f(J, \mu).$$

Possible concerns with this functional form include difficulties with data generation, the need for more sophisticated fitting algorithms, and the reduction of physical insight obtained from the fitted values of the model parameters.

### D.7.3.2 Orbits About Other Lagrange Points

A more likely pursuit involves the implementation of Jacobi scaling functions for Lyapunov orbits about other Lagrange points, in particular, about  $L_1$ . For  $L_1$  specifically, it is reasonable to expect that the power law relation still holds due to the qualitatively similar local dynamics.

### D.7.3.3 Systems with Arbitrary Mass Ratio

Thus far, we have only considered  $\mu = 0.012$  and  $\mu = 3 \times 10^{-6}$  as these are the mass ratios of the Earth-Moon and Sun-Earth systems, respectively, and we are only interested in these two systems for our particular application. However, it should be possible, in principle, to extend the form of (D.26) for arbitrary  $\mu$ . The value of  $\|\delta \mathbf{x}\|$  should vary continuously with  $\mu$ , and we expect that this pursuit will, indeed, give good results.





# APPENDIX E

## Coordinate Transformations

---

Given a solution to the PCR3BP in either the inertial frame, the Sun-Earth rotating frame, or the Earth-Moon rotating frame, it should be possible to re-express this solution in either of the other frames. These coordinate transformations are derived in the following appendix. The position and orientation of the Earth-Moon frame relative to the Sun-Earth frame is given by the bicircular model, as used in [19], and explained in detail in Chapter 7.

### E.1 Geometry of the Coupled Systems

Consider two planar circular restricted three body problems in the following configuration. Let  $m_1$ ,  $m_2$ , and  $m_3$  be the masses of the Sun, Earth, and Moon, respectively. Let  $R_1$  and  $R_2$  be the Sun-Earth and Earth-Moon separations, respectively. Let  $n_1$  and  $n_2$  be the angular velocities of the Sun-Earth and Earth-Moon rotating systems, respectively. From two body dynamics,

$$n_1 = \sqrt{\frac{G(m_1 + m_2)}{R_1^3}}$$
$$n_2 = \sqrt{\frac{G(m_2 + m_3)}{R_2^3}},$$

Also define  $\mu \equiv m_2/(m_1 + m_2)$  and  $\nu \equiv m_3/(m_2 + m_3)$ , the mass ratios of each system.

The inertial frame originates at the Sun-Earth barycenter. The Sun-Earth frame originates at the Sun-Earth barycenter and rotates with angular frequency  $n_1$ , so that the Sun is fixed at the point  $(-\mu R_1, 0)$  and the Earth-Moon barycenter is fixed at the point  $((1 - \mu)R_1, 0)$ . The Earth-Moon frame is centered at the Earth-Moon barycenter and rotates with angular velocity  $n_2$ , so that the Earth is fixed at the point  $(-\nu R_2, 0)$  and the Moon is fixed at  $((1 - \nu)R_2, 0)$  in this frame. See Figure C.2 for a schematic diagram.

### E.2 Coordinate Transformations

#### E.2.1 Vector Form

Let  $\{x, y\}$  be the coordinates in the inertial frame,  $\{x', y'\}$  the coordinates in the Sun-Earth rotating frame, and  $\{x'', y''\}$  the coordinates in the Earth-Moon rotating frame.

In the inertial frame,

$$\mathbf{r} = x\hat{\mathbf{x}} + y\hat{\mathbf{y}}. \quad (\text{E.1})$$

To change coordinates from the unprimed system to the primed system, use

$$\mathbf{r}' = (\mathbf{r} \cdot \hat{\mathbf{x}}')\hat{\mathbf{x}}' + (\mathbf{r} \cdot \hat{\mathbf{y}}')\hat{\mathbf{y}}', \quad (\text{E.2})$$

where

$$\begin{aligned} \hat{\mathbf{x}}' &= \cos n_1 t \hat{\mathbf{x}} + \sin n_1 t \hat{\mathbf{y}} \\ \hat{\mathbf{y}}' &= -\sin n_1 t \hat{\mathbf{x}} + \cos n_1 t \hat{\mathbf{y}}. \end{aligned} \quad (\text{E.3})$$

are the unit vectors of the Sun-Earth rotating system. Now in the primed system,

$$\mathbf{r}' = x'\hat{\mathbf{x}}' + y'\hat{\mathbf{y}}'. \quad (\text{E.4})$$

To change from the primed system to the double primed system, the origin of the old coordinate system must be translated to the barycenter of the Earth-Moon system and then the axes rotated again. This process is expressed by

$$\mathbf{r}'' = [(\mathbf{r}' - (1 - \mu)R_1\hat{\mathbf{x}}') \cdot \hat{\mathbf{x}}'']\hat{\mathbf{x}}'' + [(\mathbf{r}' - (1 - \mu)R_1\hat{\mathbf{x}}') \cdot \hat{\mathbf{y}}'']\hat{\mathbf{y}}'', \quad (\text{E.5})$$

where

$$\begin{aligned} \hat{\mathbf{x}}'' &= \cos n_2 t \hat{\mathbf{x}}' + \sin n_2 t \hat{\mathbf{y}}' \\ \hat{\mathbf{y}}'' &= -\sin n_2 t \hat{\mathbf{x}}' + \cos n_2 t \hat{\mathbf{y}}'. \end{aligned} \quad (\text{E.6})$$

Now in the double primed system,

$$\mathbf{r}'' = x''\hat{\mathbf{x}}'' + y''\hat{\mathbf{y}}''. \quad (\text{E.7})$$

Equations (E.2) and (E.3) provide all the information necessary to transform from the unprimed system to the primed system and vice versa. Equations (E.5) and (E.6) facilitate transforming from the primed system to the double primed system and back again.

### E.2.2 Matrix Form

It is useful to restate the coordinate transformations in matrix form. First define

$$A_1 \equiv \begin{pmatrix} \cos n_1 t & \sin n_1 t \\ -\sin n_1 t & \cos n_1 t \end{pmatrix} \quad (\text{E.8})$$

$$A_2 \equiv \begin{pmatrix} \cos n_2 t & \sin n_2 t \\ -\sin n_2 t & \cos n_2 t \end{pmatrix}. \quad (\text{E.9})$$

Equations (E.2) and (E.3) can be combined to read

$$\begin{pmatrix} x' \\ y' \end{pmatrix} = A_1 \begin{pmatrix} x \\ y \end{pmatrix}, \quad (\text{E.10})$$

which, inverted, reads

$$\begin{pmatrix} x \\ y \end{pmatrix} = A_1^{-1} \begin{pmatrix} x' \\ y' \end{pmatrix}, \quad (\text{E.11})$$

Equations (E.5) and (E.6) can also be combined to read

$$\begin{pmatrix} x'' \\ y'' \end{pmatrix} = A_2 \begin{pmatrix} x' \\ y' \end{pmatrix} - (1 - \mu)R_1 \begin{pmatrix} \cos n_2 t \\ -\sin n_2 t \end{pmatrix} \quad (\text{E.12})$$

which, inverted, reads

$$\begin{pmatrix} x' \\ y' \end{pmatrix} = A_2^{-1} \left[ \begin{pmatrix} x'' \\ y'' \end{pmatrix} + (1 - \mu)R_1 \begin{pmatrix} \cos n_2 t \\ -\sin n_2 t \end{pmatrix} \right]. \quad (\text{E.13})$$

In addition, the velocities can be transformed by differentiating the above expressions. These transformations are given by the following.

$$\begin{pmatrix} \dot{x}' \\ \dot{y}' \end{pmatrix} = A_1 \begin{pmatrix} \dot{x} + n_1 y \\ \dot{y} - n_1 x \end{pmatrix} \quad (\text{E.14})$$

$$\begin{pmatrix} \dot{x} \\ \dot{y} \end{pmatrix} = A_1^{-1} \begin{pmatrix} \dot{x}' - n_1 y' \\ \dot{y}' + n_1 x' \end{pmatrix} \quad (\text{E.15})$$

$$\begin{pmatrix} \dot{x}'' \\ \dot{y}'' \end{pmatrix} = A_2 \begin{pmatrix} \dot{x}' + n_2 y' \\ \dot{y}' - n_2 x' \end{pmatrix} + n_2(1 - \mu)R_1 \begin{pmatrix} \sin n_2 t \\ \cos n_2 t \end{pmatrix} \quad (\text{E.16})$$

$$\begin{pmatrix} \dot{x}' \\ \dot{y}' \end{pmatrix} = A_2^{-1} \begin{pmatrix} \dot{x}'' - n_2 y'' \\ \dot{y}'' + n_2 x'' \end{pmatrix} \quad (\text{E.17})$$

It may be desired to change the initial orientation of the Earth-Moon frame to the Sun-Earth frame by some phase angle  $\theta$ . To do this, replace  $t \rightarrow t + \theta/n$  in (E.10) through (E.17).

### E.3 Non-Dimensional Coordinates

In the Sun-Earth frame, units are non-dimensionalized as follows

$$\begin{aligned} \text{mass} \quad m' &= m/(m_1 + m_2) \\ \text{time} \quad t' &= n_1 t \\ \text{distance} \quad d' &= d/R_1 \\ \text{velocity} \quad v' &= v/(n_1 R_1). \end{aligned} \quad (\text{E.18})$$

In the Earth-Moon frame, units are non-dimensionalized as

$$\begin{aligned} \text{mass} \quad m'' &= m/(m_2 + m_3) \\ \text{time} \quad t'' &= n_2 t \\ \text{distance} \quad d'' &= d/R_2 \\ \text{velocity} \quad v'' &= v/(n_2 R_2). \end{aligned} \quad (\text{E.19})$$

(See Appendix F for the code written in MATLAB to perform these transforms)

# APPENDIX F

## The MATLAB Toolbox

---

This appendix lists, with brief discussions, the code written for this project in MATLAB. It is split into the various stages required to implement the method outlined this report.

### F.1 Manifold Computation

First the problem of computing invariant manifolds is considered:

1. Calculate the location of the Lagrange Points  $L_1$  to  $L_5$ :

- `lagrange`
  - Calculates matrix containing non-dimensionalized positions of Lagrange points 1 to 5 in the PCR3BP with mass ratio  $\mu$ .
- `lagrange1`
  - Calculates non-dimensionalized x co-ordinate of  $L_1$  in the PCR3BP with mass ratio  $\mu$ .
- `lagrange2`
  - Calculates non-dimensionalized x co-ordinate of  $L_2$  in the PCR3BP with mass ratio  $\mu$ .
- `lagrange3`
  - Calculates non-dimensionalized x co-ordinate of  $L_3$  in the PCR3BP with mass ratio  $\mu$ .

2. Calculate linear periodic orbits:

- `amp2lyap_lin`
  - Translates from an x-amplitude to the corresponding initial condition and period for a Lyapunov orbit about a Lagrange point in the linearized PCR3BP with mass ratio  $\mu$  and at a specified phase of the moon.
- `jacobi2lyap_lin`
  - Translates from a Jacobi Constant to the corresponding initial condition and period for a Lyapunov orbit about a Lagrange point in the linearized PCR3BP with mass ratio  $\mu$  and at a specified phase of the moon.

- **twobody**
    - Evaluates the two-body equations of motion.
3. Calculate Lyapunov Orbits using a Differential Corrector and Continuation methods:
- **dcl yap**
    - Corrects the initial conditions and period from the linear approximation of a Lyapunov orbit about the collinear Lagrange points in the PCR3BP with mass ratio  $\mu$ .
  - **dcnxj**
    - Takes an x value or Jacobi constant and gives corrected initial values for a Lyapunov orbit in the PCR3BP with mass ratio  $\mu$ .
  - **pcr3bp**
    - Evaluate the nonlinear planar circular restricted three-body equations of motion for a mass ratio (secondary-to-primary)  $\mu$ .
  - **diffcorr**
    - Evaluates the differential correction ODE system for the PCR3BP with mass ratio  $\mu$ , consisting of the nonlinear equations of motion for the system states, and the differential equation for the state transition matrix.
4. Calculate Stable and Unstable directions
- **monodromy**
    - Computes the initial monodromy matrix for a Lyapunov orbit in the PCR3BP with mass ratio  $\mu$ , at a point on the x-axis.
  - **su\_vectors**
    - Calculate the stable and unstable eigenvectors on a periodic orbit of a nonlinear PCR3BP with mass ratio  $\mu$ .
5. Manifold Propagation
- **j2dv**
    - Uses best-fit parameters (in the least-squares sense) to estimate the appropriate perturbation magnitude for an  $L_2$  Lyapunov orbit with a given Jacobi constant in the PCR3BP with mass ratio  $\mu$ .

Also to consider in the generation of manifolds is the Jacobi Constant:

Jacobi Constant

- `[J, Jmean, Jstd]=jacobi(v, mu)`
  - Computes the Jacobi constant from the state vector in the PCR3BP with mass ratio  $\mu$ . Also computes the mean Jacobi constant and the standard deviation (for J a vector).

Below are two of the functions used to visualize the manifolds:

#### Manifold Plot

- `Manifold_Plot(A, mu)`
  - Plots manifold from Lyapunov orbit with x-amplitude in the PCR3BP with mass ratio  $\mu$ .
- `manifoldplot(m, c)`
  - Plots a manifold the color 'c'.

## F.2 Manifold Transfer

Once manifolds are computed, transfers between manifolds in the two different systems need to be studied, and transfers between circular orbits and manifolds found in order to find a final trajectory.

### 1. Co-ordinate Transforms and Non-Dimensionalization

- `em_nd2em_dim`
  - Dimensionalizes a state vector in the Earth-Moon rotating frame.
- `em_dim2em_nd`
  - Non-dimensionalizes a state vector in the Earth-Moon rotating frame.
- `em_dim2se_dim`
  - Converts a dimensional state vector in the Earth-Moon rotating frame to a dimensional state vector in the Sun-Earth rotating frame.
- `se_dim2em_dim`
  - Converts a dimensional state vector in the Sun-Earth rotating frame to a dimensional state vector in the Earth-Moon rotating frame.
- `se_dim2se_nd`
  - Non-dimensionalizes a state vector in the Sun-Earth rotating frame.
- `se_nd2se_dim`
  - Dimensionalizes a state vector in the Sun-Earth rotating frame.

- **se\_traj2em\_traj**
  - Converts a non-dimensional trajectory in the Sun-Earth rotating frame to a non-dimensional trajectory in the Earth-Moon rotating frame. Combines above functions for dimensionalization and transforms.
- **em\_traj2se\_traj**
  - Converts a non-dimensional trajectory in the Earth-Moon rotating frame ( $x_{em}$ ) to a non-dimensional trajectory in the Sun-Earth rotating frame ( $x_{se}$ ) with Jacobi constant  $J_{se}$  in the Sun Earth frame. Combines above functions for dimensionalization and transforms.
- **man\_em2se**
  - Transforms a manifold from non-dimensional Earth-Moon rotating frame to non-dimensional Sun-Earth rotating frame.

## 2. Intersection of Manifolds

- **cut**
  - Cuts a multi-valued discretized function into single-valued branches.
- **intersect1**
  - Computes the (x,y) intersections between curves via linear interpolation.
- **intersectn**
  - Computes the (x,y) intersections between curves via linear interpolation.
- **grid2poly**
  - Constructs polygons from points by grid overlay.
- **area\_poly**
  - Computes the total area of a polygon.
- **area\_int**
  - Computes the area of intersection of two polygons constructed from points by grid overlay.
- **man\_xyintersect1**
  - Finds the spatial intersections of a pair of single-valued discretized functions and returns the corresponding coordinates in velocity space.
- **man\_xyintersectn**
  - Computes spatial intersections of two manifolds via linear interpolation and the velocities of the manifolds at this points of intersection.
- **manifold\_area\_int**
  - Computes measures of the area (in velocity space) of low-energy transfer between two manifolds assuming impulsive thrusts.



- **psectd**
  - Computes the (discretized) Poincare section of two manifolds at a given spatial coordinate restriction.
- **psect**
  - Computes the (continuous) Poincare section of two manifolds at a given spatial coordinate restriction.

### 3. Transfer between Circular Orbits and Manifolds

- **bp2**
  - Evaluates the two-body equations of motion .
- **deltav**
  - Calculates a vector of  $\Delta v$  values at each point from a matrix of intersections.
- **find\_LEO**
  - Searches through database to find lowest  $\Delta v$ 's of intersection of manifolds with circular orbits in Sun-Earth system.
- **find\_LL0**
  - Searches through database to find lowest  $\Delta v$ 's of intersection of manifolds with circular orbits in Earth-Moon system.
- **traj**
  - Computes minimum  $\Delta v$  value of 'manifold' intersection with a low Earth or low Lunar orbit.
- **traje**
  - Computes intersection of manifold 'me' with low Earth orbit.
- **trajm**
  - Computes intersection of manifold 'mm' with low Lunar orbit.
- **vele**
  - Calculates the velocity required to remain in a circular orbit above the Earth using the two body equations of motion.
- **velm**
  - Calculates the velocity required to remain in a circular orbit above the Moon using the two body equations of motion.

Also used in the manifold intersection code is the function 'PolygonClipper', a routine written by Sebastian Hölz obtained online from the MATLAB Central File Exchange.

### F.3 Trajectory Correction

In order to find a final transfer from the Earth to the moon the following functions are needed:

#### 1. Trajectory Correction

- **fbpcorr\_se**
  - Accepts an initial guess for a trajectory in the 4-body system and returns a continuous trajectory, constrained to have fixed position coordinates at the endpoints.
- **sem\_bicirc\_se**
  - Evaluates bicircular model of the equations of motion for the restricted four-body Sun-Earth-Moon-spacecraft problem (the spacecraft is the negligible mass) in the non-dimensionalized Sun-Earth rotating frame. The Moon is assumed to have initial phase theta.

To run a comparison of the final trajectory with the Hohmann transfer the following function could be used:

#### Hohmann Transfer

- **hohmann\_e2m**
  - Computes the  $\Delta - v$  cost and the propellant mass fraction for a Hohmann transfer from an Earth orbit to a lunar orbit using an engine providing a specific impulse.

### F.4 Database

Listed below are the functions written to compile the database of manifolds (stored as structs).

#### Compiling the Database

- **Database(AInit, AFinal, AStep, mu)**
  - Creates the manifold files and places them in the database folder.
- **[x SE\_mani] = Load\_EO(direction, Jacobi)**
  - Loads up the intersections, x, of a Sun-Earth Manifold and a low earth orbit (LEO).
- **[x SE\_mani] = Load\_EO(direction, Jacobi)**
  - Loads up the intersections, x, of a Sun-Earth Manifold and a low earth orbit (LEO).

- `my_struct = Load_Manifold(stability, Lag_Point_Number, mu, J)`  
 - Loads a manifold from the database with at specified mass ratio,  $\mu$ , and Jacobi,  $J$ .
- `Save_Manifold(A, mu)`  
 - Computes and stores a manifold into a text file, where  $A$  is the x-amplitude,  $\mu$  the specified mass ratio.
- `m=store_traj(l,mu,n,x0,T,t,v)`  
 - Stores trajectory data in struct form - Computes and stores the Jacobi constant, and the input data in struct form. Here  $l$  is the Lagrange point number,  $\mu$  the PCR3BP system mass ratio,  $n$  the number of total trajectories,  $x_0$  the initial condition (at angle zero) of originating Lyapunov orbit,  $T$  the period of originating Lyapunov orbit,  $t$  the trajectory time vector and  $V$  the trajectory state vector.

## F.5 Integration

### F.5.1 Runge-Kutta Order Schemes

Due to the fact that small inaccuracies can produce large errors in dynamical systems, rather than using the conventional Runge-Kutta order 4/5 scheme ( MATLAB function `ode45`) a more accurate (though computationally expensive) Runge-Kutta order 7/8 scheme was used (`ode78`). In particular, when the monodromy matrix was computed from the differentially corrected Lyapunov orbit using `ode45`, a slight gap in the manifolds occurred, as shown in Figure 1. This was initially thought to be a natural consequence of the dynamical system, and indeed it was caused by slightly inaccurate results. The source of this inaccuracy, however, was due to error in the integrator<sup>1</sup>.

### F.5.2 Integration Options

The MATLAB function `ode45` has a list of integration options available, one of these being a test condition to stop integrating. In particular, when differentially correcting the Lyapunov Orbit, the integration was stopped once half of the orbit was computed, which corresponded to the y-value of the integration scheme becoming positive. While MATLAB has a built in option for this type of scheme, the `ode78` scheme developed as part of this project was lacking such a detection option.

This functionality was programmed by adding a stop condition to `ode78`, which is contained in `my_ode78_stop2`. Once the integration scheme integrates to a y-value greater than zero, integration stops and the penultimate values are used as initial values in the

---

<sup>1</sup>Indeed, a closer look at the figures from the RIPS 2005 JPL project reveals manifolds with similar gaps. Their routines all use MATLAB's `ode45`.

iteration routine `my_ode78_stop2a`. The iteration routine then returns only the time and final set of values when the y-value is within a certain tolerance of zero.

The last modification to `ode78` was actually a simplification, which was used in the computation of the monodromy matrix. Rather than using `ode45` with an equal step size (which really means using Runge-Kutta 4th order scheme), we took the same step size and used a Runge-Kutta 7th order scheme `my_ode78_equal`. As mentioned in the previous section, this modification gave the necessary accuracy to get rid of the gaps in the manifolds.

## Bibliography

---

- [1] E. A. Belbruno. *Capture dynamics and chaotic motions in celestial mechanics*. Princeton University Press, Princeton, NJ, 2004. With applications to the construction of low energy transfers, With a foreword by Jerry Marsden.
- [2] E. A. Belbruno and J. K. Miller. Sun-perturbed earth-to-moon transfers with ballistic capture. *Journal of Guidance Control Dynamics*, 16:770–775, 1993.
- [3] E. Canalias, G. Gómez, M. Marcote, and J. J. Masdemont. Assessment of mission design including utilization of libration points and weak stability boundaries. European Space Agency, 2004.
- [4] C. C. Conley. Low energy transit orbits in the restricted three-body problem. *SIAM Journal on Applied Mathematics*.
- [5] M. Dellnitz, O. Junge, W. S. Koon, F. Lekien, M. W. Lo, J. E. Marsden, K. Padberg, R. Preis, S. D. Ross, and B. Thiere. Transport in dynamical astronomy and multibody problems. *International Journal of Bifurcation and Chaos in Applied Sciences and Engineering*, 15(3), 2005.
- [6] D. Folta and M. Beckman. Libration orbit mission design: Applications of numerical and dynamical methods. In Gerard Gómez, Martin W. Lo, and Josep J. Masdemont, editors, *Proceedings of the Conference Libration Point Orbits and Applications*, pages 95–97, New Jersey, 2003. World Scientific Publishing Co. Pte. Ltd.
- [7] G. Gómez, W. S. Koon, M. W. Lo, J. E. Marsden, J. Masdemont, and S. D. Ross. Invariant manifolds, the spatial three-body problem and space mission design. *American Astronautical Society*, pages 1–20, 2001.
- [8] G. Gómez, W. S. Koon, M. W. Lo, J. E. Marsden, J. Masdemont, and S. D. Ross. Connecting orbits and invariant manifolds in the spatial restricted three-body problem. *Nonlinearity*, 17(5):1571–1606, 2004.
- [9] K. C. Howell. Three-dimensional, periodic, “halo” orbits. *Celestial Mechanics*, 32(1):53–71, 1984.

- [10] K. C. Howell, B. T. Barden, and M. W. Lo. Application of dynamical systems theory to trajectory design for a libration point mission. *American Astronautical Society. Journal of the Astronautical Sciences*, 45(2):161–178, 1997.
- [11] R. Jehn, S. Campagnola, D. Garcia, and S. Kemble. Low-thrust approach and gravitational capture at mercury. In *ESA SP-548: 18th International Symposium on Space Flight Dynamics*, 2004.
- [12] W. S. Koon, M. W. Lo, J. E. Marsden, and S. D. Ross. Dynamical systems, the three-body problem and space mission design. In *International Conference on Differential Equations, Vol. 1, 2 (Berlin, 1999)*, pages 1167–1181. World Sci. Publishing, River Edge, NJ, 2000.
- [13] W. S. Koon, M. W. Lo, J. E. Marsden, and S. D. Ross. Heteroclinic connections between periodic orbits and resonance transitions in celestial mechanics. *Chaos*, 10:427–469, 2000.
- [14] M. W. Lo. Libration point trajectory design. *Numerical Algorithms*, 14(1-3):153–164, 1997. Dynamical numerical analysis (Atlanta, GA, 1995).
- [15] M. W. Lo, W. S. Koon, J. E. Marsden, and S. D. Ross. Low energy transfer to the moon. *Celestial Mechanics and Dynamical Astronomy*.
- [16] J. B. Marion and S. T. Thornton. *Classical Dynamics of Particles and Systems*. Saunders College Publishing, Fort Worth, 1995.
- [17] J. E. Marsden and S. D. Ross. New methods in celestial mechanics and mission design. *American Mathematical Society. Bulletin. New Series*, 43(1):43–73, 2006.
- [18] J. E. Prussing and B. A. Conway. *Orbital Mechanics*. Oxford University Press, 1993.
- [19] S. D. Ross. *Cylindrical Manifolds and Tube Dynamics in the Restricted Three-Body Problem*. PhD dissertation, California Institute of Technology, Pasadena, California, 2004.
- [20] V. Szebehely. *Theory of Orbits: The Restricted Problem of Three Bodies*. Academic Press, New York, New York, 1967.